Computational Modeling of the Cervical Spinal Cord: Integration into a Human Body Model to Investigate Response to Impact

by

Aleksander Lukasz Rycman

A thesis

presented to the University of Waterloo

in fulfillment of the

thesis requirement for the degree of

Doctor in Philosophy

in

Mechanical and Mechatronics Engineering

Waterloo, Ontario, Canada, 2022

Examining Committee Membership

The following served on the Examining Committee for this thesis. The decision of the Examining Committee is by majority vote.

External Examiner   KARIN BROLIN

Professor, Department of Applied Mechanics
Chalmers University of Technology

Supervisor(s)   DUANE S. CRONIN

Professor, Mechanical and Mechatronic Engineering,
University of Waterloo

STEWART D. MCLACHLIN

Assistant Professor, Mechanical and Mechatronic Engineering
University of Waterloo

Internal Member   CLIFFORD BUTCHER

Assistant Professor, Mechanical and Mechatronic Engineering
University of Waterloo

Internal Member   ADIL AL-MAYAH

Associate Professor, Civil and Environmental Engineering
University of Waterloo

Internal-external Member   JACK P. CALLAGHAN

Professor, Kinesiology and Health Sciences
University of Waterloo

Author's Declaration

This thesis consists of material all of which I authored or co-authored: see Statement of Contributions included in the thesis. This is a true copy of the thesis, including any required final revisions, as accepted by my examiners.

I understand that my thesis may be made electronically available to the public.

Statement of Contributions

Aleksander Rycman developed all presented methods in this thesis including: (1) calibration methodology of the material models, (2) indentation and impact validation models, (3) development of the geometry and mesh of the cervical nervous tissues, (4) implementation of the spinal cord tissue in the GHBMC M50 model, and (5) evaluation of the strains in the brain and spinal cord tissue in the dynamic impact scenarios. Duane Cronin and Stewart McLachlin formulated a general plan to implement the spinal cord in a contemporary human body model, provided technical supervision and guidance, and editorial feedback on the thesis.

Some of the thesis content has been previously published in the following journal articles or conference proceedings:

Rycman A., McLachlin S., Cronin, D.S., (2019). "Hyper-Viscoelastic Constitutive Material Model of the Cervical Spinal Cord to Predict Impact Response", The Injury Biomechanics Symposium, Ohio May 2019

AR performed all model simulation, data post-processing and drafted the article (70%). DC (15%) and SM (15%) provided technical guidance and changes to the manuscript.

Rycman A. L., McLachlin S. D, Cronin D. S, (2020). "Comparison of Spinal Cord Impact Response with a Cerebrospinal Fluid Layer Using Three Numerical Formulations", In International Research Council on Biomechanics of Injury, IRCOBI, Munich

AR performed all model simulation, data post-processing and drafted the article (70%). DC (15%) and SM (15%) provided supervision and coordination to the study and served as editors to the manuscript.

Rycman, A., McLachlin, S., & Cronin, D. S. (2021). A Hyper-Viscoelastic Continuum-Level Finite Element Model of the Spinal Cord Assessed for Transverse Indentation and Impact

Loading. Frontiers in Bioengineering and Biotechnology, 9. https://doi.org/10.3389/fbioe.2021.693120

AR performed all model simulations including data post-processing and drafted the article (70%). DC provided supervision contribution to this study and technical support with the FE model (15%). SM (15%) contributed by providing substantial technical advice and reviewer to the manuscript.

Rycman, A., McLachlin, S., & Cronin, D. S. (2022). Comparison of numerical methods for cerebrospinal fluid representation and fluid–structure interaction during transverse impact of a finite element spinal cord model. International Journal for Numerical Methods in Biomedical Engineering. https://doi.org/10.1002/cnm.3570

DC (10 %) and SM (10 %) served as reviewers of the pre-print of the manuscript and provide technical support. AR prepared and processed the models and drafted first version of the manuscript (80%).

Co-authors agree with the evaluation of the roles and contributions:

X
Stewart McLachlin

X
Duane Cronin

Abstract

Acute spinal cord injuries (SCI) have a global annual occurrence rate of 14 to 40 per million population with considerable societal cost. The primary mechanism of injury involves physical damage to the nervous tissues, such as spinal cord compression resulting from fracture or dislocation of the vertebra. However, experimental findings have indicated that neurological sequela can occur without radiographic abnormalities of the neural tissues. In addition, studies have suggested that the cerebrospinal fluid (CSF) layer may play a protective role for the spinal cord during impact. Yet, there are significant limitations to examining SCI experimentally, resulting in large gaps in understanding. Computational Human Body Models (HBM) are an alternative and potentially important tool to investigate the risk of SCI. A key challenge in applying contemporary HBM to study SCI is the need for a biofidelic model of the spinal cord, which accurately predicts the loading and response of the cervical neural tissues in relevant impact scenarios.

This thesis developed and validated a finite element model of the cervical spinal cord and associated tissues and integrated this model within a contemporary HBM to achieve two aims: (1) to provide a tool for the assessment of spinal cord response in impact scenarios; and (2) to create an improved physical boundary condition for the brain and brain stem, which is a limitation of current HBM. The geometry of the cervical neural tissues was defined using subject-specific magnetic resonance imaging and literature data. The salient mechanical properties of cervical neural tissues were identified, and experimental data were used to fit appropriate constitutive material models for each tissue. Experimental pellet impact tests and indentation tests on the spinal cord were simulated to validate the tissue mechanical properties, verify finite element mesh refinement and assess numerical representation of the CSF. The developed material models and meshes of the cervical neural tissues were integrated into a contemporary HBM. Lastly, the contemporary HBM with implemented cervical neural tissues was simulated in frontal, lateral, rear, and oblique impact scenarios. A comprehensive assessment of the spinal cord influence on brain tissue deformation was undertaken. In general, the presence of the spinal cord in the HBM model increased the strains observed in the brain tissue. The brain stem tissue observed the largest average increase of 17% in strain.

Results from this work provided the first validated finite element model of the cervical neural tissues and cerebrospinal fluid layer integrated into a state-of-the-art full-body HBM for transient impact simulations. This model enabled the prediction of spinal cord response for impact scenarios, improved anatomic boundary conditions for connection to the brain tissue, and ultimately will assist in assessing safety systems to mitigate catastrophic human injuries.

Acknowledgements

Table of Contents

List of Figures

List of Tables

List of Equations

List of Nomenclature

Abbreviations

ALE	Arbitrary Lagrangian-Eulerian
ASME	American Society of Mechanical Engineers
CG	Center of Gravity
CNS	Central Nervous System
CORA	Correlation and Analysis
CSDM	Cumulative Strain Damage Measure
CSF	Cerebrospinal Fluid
CT	Computed Tomography
ELF	Extraforaminal Ligament
EOS	Equation of State
FE	Finite Element
FSI	Fluid Structure Interaction
HBM	Human Body Model
NBDL	Naval Biodynamics Laboratory
NSCISC	The National Spinal Cord Injury Statistics Center
MPS	Maximum Principal Strain
MPS_{95}	Maximum 95th Percentile of the Maximum Principal Strain
MRI	Magnetic Resonance Imaging
PAC	Pia-Arachnoid-Complex
PV	Pressurized Volume
SCI	Spinal Cord Injury
SCP	Spinal Cord-Pia Mater Complex
SPH	Smoothed Particle Hydrodynamics
RSME	Root-Square-Mean Error
TBI	Traumatic Brain Injury
QLV	Quasi-Linear Viscoelasticity
VAI_{MPS}	Volume Weighted Average Increase Maximum Principal Strain

Symbols

C	Fluid bulk speed of sound
C_0	Fluid bulk speed of sound
G(t)	Viscoelastic relaxation function
G_i	Shear relaxation modulus
J	Relative volume
K	Bulk modulus
p	Pressure
P_{cut}	Pressure cut-off value
S_{ij}	Deviatoric part of stress
S_1	Constant of the Mie- Grüneisen equation of state
VC	Viscous parameter
W	Strain energy function
α_i	Ogden model material constant
β_i	Decay constant
γ	Constant of the equation of state, Grüneisen's gamma
ΔL	Characteristic length
ε	Strain
$\dot{\varepsilon}$	Strain rate
$\dot{\varepsilon}_{ij}$	Deviatoric part of strain rate
λ_i^*	Deviatoric principal stretch
μ_i	Ogden model material constant
ν	Poisson's ratio
ρ	Fluid current density
ρ_0	Fluid initial density
$\sigma(t)$	Total stress in viscoelastic model

Chapter 1
Introduction

Spinal cord injuries (SCIs) are serious and often life-threatening injuries with high social and economical costs. Despite the global effort in SCI prevention research, SCIs are still common in developed and developing countries. The National Spinal Cord Injury Statistics Center (NSCISC) reported 17,900 new SCIs across the United States in 2020; whereas, in Canada, the 2010 incidence of SCIs was estimated to be 3,174 (Noonan et al., 2012). In Ontario 2,465 new SCIs were reported in the time span of 3 years from 2003 to 2006 (Guilcher et al., 2010). The global incidence of SCIs was estimated to be 930 000 new cases per year and it was reported that the prevalence of SCIs did not change significantly between 1990 to 2016 (James et al., 2019). Individuals who suffer SCI require expensive and frequently lifelong rehabilitation and treatment. SCIs are associated with psychological, neurological, physical, and social disorders. Although the occurrence rate of the SCIs is not as frequent as diseases such as cancer or stroke, the costs to society are significant (Sadowsky et al., 2002), and SCIs primarily affect the working age population (~20-49 years old) (Pickett et al., 2006). The direct lifetime cost of the SCI for a patient who was injured at the age of 25 ranges from 2.1 to 5.4 million dollars and depends greatly on the educational level, neurological impairment, age at the injury and pre-injury employment history (Cao et al., 2011). Indirect costs, such as losses in wages, fringe benefits, and productivity, associated with SCI were estimated on average at 77 000 dollars per injury (NSCISC).

The most common cause of spinal cord trauma is motor vehicle accidents, accounting for more than one-third of all SCIs (Pickett et al., 2006; DeVivo, 1997; Lee et al., 2014). The cervical region of the spinal cord is the most frequently injured; 55% of all SCI are localized in this region. Fracture dislocations and burst fractures are the leading mechanisms of the SCIs (Sekhon and Fehlings, 2001).
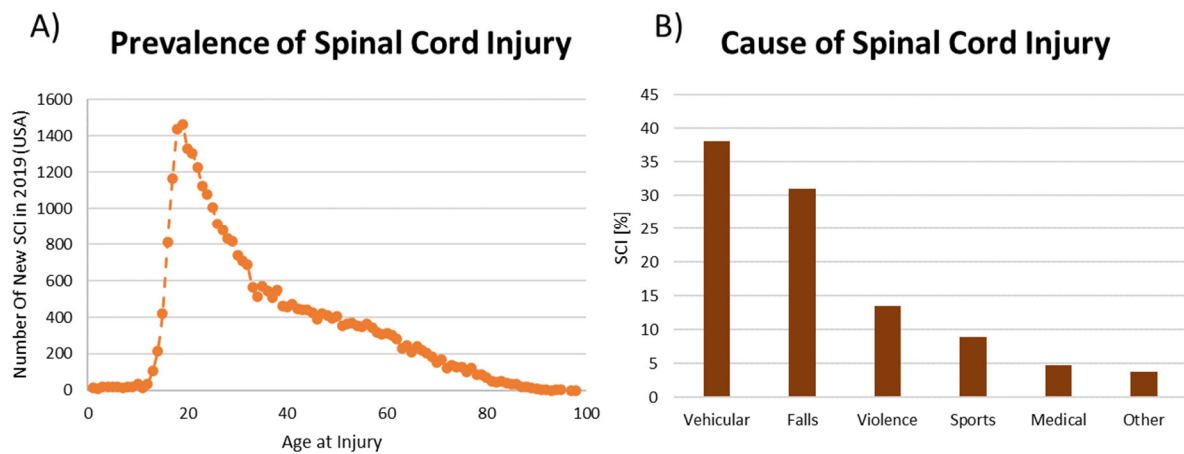
Figure 1.1: A) Prevalence of the spinal cord injuries in the USA by age of the injured person (based on the NSCISC 2016 annual statistical report); (B) cause of the spinal cord injury (Pickett et al., 2006).

SCIs can be grouped based on the mechanism of injury, neurological implications, or severity grade of injury. The mechanisms of SCI can be divided into two phases: primary (acute) and secondary (Dumont et al., 2001). Primary injury is associated with a dynamic event and physical damage to the spinal cord cells, surrounding tissues, and blood vessels; whereas, secondary (chronic) injury develops over time. Dumont et al. (2001) distinguished four essential mechanisms of primary injury: (1) impact with compression, (2) impact with ephemeral compression, (3) laceration, and (4) distraction. The first mechanism is the most common and can be observed in burst fractures, fractures of the vertebral bodies with dislocations, and severe intervertebral disc ruptures. Impacts with temporary compression are observed in subjects with degenerative spine diseases. Lacerations are mostly caused by foreign body (e.g., gun bullet) or intrusion of sharp retropulsed bone fragments into the spinal canal as well as bilateral facet dislocations (Ivancic et al., 2007). The last mechanism, distraction of the spinal cord, occurs when the forces from the motion of the spine (flexion, extension, lateral bending, and rotation) produce abnormal stresses and strains in the transverse plane on the spinal cord (Panjabi and White, 1988).

Following mechanical damage to the neural and vascular tissues, secondary injury mechanisms may be induced. The secondary mechanisms are associated with neurogenic shock,

hemorrhage and hematoma, apoptosis, ischemia, excitotoxicity, hypercalcemia, electrolyte imbalance and other biochemical processes (Liu et al., 1997). Nerve cells are further damaged either by insufficient blood supply, the toxicity of surrounding fluid, or compression of the neural tissues resulting from hemorrhage.

To date, experimental data, animal injury models, and field data have provided crucial knowledge to understand SCI (Jones and Clarke, 2018). However, the ability to obtain detailed insights into SCI mechanisms through experimental or epidemiological means remains limited. As an alternative, investigations using finite element (FE) human body models (HBMs) can be used to augment and enhance understanding of SCI by quantifying the cervical neural tissue deformations during simulated impact conditions.

FE full-body HBMs are virtual biomechanical representations of the human body and its anatomical systems and components (Yang, 2018). The main goal of HBMs in impact biomechanics is to simulate the response of the human body under prescribed loading scenarios (Schmitt et al., 2019). Moreover, HBMs can provide detailed insight into the mechanism of injury; thus, they are an important tool in injury prediction research. The main development of HBMs is being conducted in the automotive industry to improve and enhance vehicle safety systems (Bostrom et al., 2003; Hartlieb et al., 2015, Iraeus et al., 2020). Currently, three adult full-body computational HBMs have been adopted globally: the Global Human Body Models Consortium (GHBMC) (Barker and Cronin, 2021), the Total Human Model for Safety (THUMS) (Iwamoto et al., 2015), and the Virtual Vehicle Safety Assessment (ViVA) (Östh et al., 2016, Kleinbach et al., 2018) and recently developed PIPER child model (Beillas et al., 2018). The main advantage of a numerical FE model is the ability to investigate the human body response at injurious levels of loading. Furthermore, the potential for injury can be investigated at multiple levels: global, organ, or localized tissue level. The complexity of the model is much higher to predict injury at the local tissue level compared to the organ or global levels (Corrales and Cronin, 2021). These models require anatomically correct geometries, detailed material models, representative boundary conditions, validation against independent

experimental data, and injury threshold levels that can relate simulation results to the probability of injury (Cronin, 2011; Schmitt et al., 2019; Yoganandan et al., 1996).

The quality of an FE HBM model lies within its validation, which ensures and quantifies the ability of the model to mimic the biomechanical response of the human body under specified loading conditions (i.e., biofidelity during impact) (Cronin, 2011). In the validation process, the developed model, based on the experimental data, is compared to an independent set of experimental data. Moreover, validation cases should cover the same regime of velocities (strain rates) as the investigation case. Finally, validation cases help developers to discover limitations of the models and build trust in the obtained simulation results (ASME V&V 40, 2018). Validation should not be confused with calibration. Calibration is the process of altering FE model parameters to match a specific set of experimental data. Calibrated models perform well with respect to the experimental data for which they were adjusted to, and as such may falsely predict response for other loading conditions (Panjabi, 1998; Yang et al., 2018).

1.1 Research Motivation

Previous research has highlighted a need to increase the understanding of SCI and development of tools that can be utilized to investigate those injuries in a safe environment. FE modeling offers significant potential to provide important new understanding into SCI mechanisms under different loading conditions. FE models of the spinal cord have been previously developed for various species, different mechanisms of injury, and varying levels of complexity (Jones and Clarke, 2018). Some studies have integrated the spinal cord and dura mater with motion segments (Greaves, 2008; Russell et al., 2012; Wilcox et al., 2003) or cervical spine (Kim et al., 2018; Stoner et al., 2020). Czyz et al. (2012) focused on developing a subject-specific spinal cord model and quantified injury by comparing the simulations results to the epidemiological data. FE animals models containing the spinal cord integrated into the spinal column were developed to provide a direct comparison with in-vivo experimental data for the same injury mechanism (Maikos et al., 2008; Russell et al., 2012). However, most of the models developed to date have contained only the spinal cord tissue and did not include the pia mater or the cerebrospinal fluid (CSF) layer, which is considered important in

biomechanical response (Jones et al., 2008; Ramo et al., 2018, Persson et al., 2011). In consideration of head-neck and full-body HBM, only simplified approaches have been applied for spinal cord modeling. For example, the current THUMS model (v6.1) has implemented cervical neural tissues, including the spinal cord, pia mater, arachnoid mater, and CSF; yet there are recognized limitations in terms of biofidelity.

While FE model developers are challenged with several aspects in developing accurate SCI models, one primary challenge has been the identification and implementation of the neural tissue material properties. Soft tissues are challenging to characterize from a mechanical point of view, mainly due to their complex response that involves anisotropy, nonlinearity, viscoelasticity and asymmetry (Yoganandan et al., 1996, Fung, 1993). The mechanical response of the spinal cord tissue is particularly difficult to accurately model, due to the non-linear anisotropic behaviour and strain-rate stiffening effects (Jannesar et al., 2018; Shetye et al., 2014). Most FE studies of SCI have used a simplified approach (e.g., linear elastic constitutive models) and investigated injury using only the spinal cord tissue without the complex geometry and interactions of the spine and surrounding soft tissues. Complex material models, incorporating viscoelastic effects, are required to characterize the spinal cord tissues under dynamic impact scenarios. The limited availability of the existing experimental data does not always fall into the desired strain rate regime, plus there is a wide range of variability observed in the published experimental data (Jones and Clarke, 2018).

1.2 Research Objectives and Scope

The proposed research entailed the identification and integration of the cervical neural tissues into the GHBMC 50th percentile male Head-Neck model (GHBMC M50 Head-Neck) for the prediction of SCI in response to impact. Moreover, this study aimed to address current limitations of existing FE spinal cord models in the literature. Therefore, material models including hyperelastic, viscoelastic, and orthotropic properties were used. The protective role and importance of the CSF layer are highlighted in the literature (Jones et al., 2008); therefore, different approaches to model fluid-structure interaction were undertaken to identify the most appropriate one. The final aim of this thesis was to implement the spinal cord into the GHBMC

M50 Head-Neck. Implementing the spinal cord into this model serves two goals: (1) expands capabilities of the GHBMC M50 Head-Neck model to predict SCI risk, and (2) provides anatomical boundary conditions for the brain stem that could influence the brain tissue deformation during impact. To achieve these goals, the following methodology was developed and implemented in this thesis:

1. **Identify the salient mechanical properties of the cervical neural tissues which drive dynamic deformation in response to impact loading.** Tissues considered include the spinal cord, dura mater, pia mater, and the CSF. Selection of the appropriate constitutive material models for each tissue was based on fitting of the material parameters to the best available experimental data for each tissue. Validation of the fitted material models was compared to an independent dynamic tissue level validation case.

2. **Develop a high-quality, subject-specific geometry (i.e., finite element mesh) of the spinal cord based on measurements from a magnetic resonance imaging (MRI) dataset, augmented with literature data.** To address the limitation of using simplified geometry to represent the spinal cord within the existing FE spinal cord models, the developed subject-specific geometry of the cervical neural tissues was based on the original MRI and CT data set that was used to develop GHBMC M50 model. Cervical spinal canal depth and width dimensions, as well as obtained dimensions of the spinal cord, were compared against data published in the literature (Fountas et al., 1998; Kameyama et al., 1996; Ko et al., 2004) to ensure that the spinal canal and developed spinal cord were representative for the population.

3. **Implement the fitted material models and developed geometries of the neural tissue into the GHBMC M50 Head-Neck model.** Stability and verification assessment of the implemented tissues in the GHBMC M50 Head-Neck model were evaluated in frontal, lateral, rear, and oblique impact cases. The influence of the spinal cord on the general head kinematics was analyzed. Finally, a sensitivity study regarding attachment of the spinal cord in the spinal canal was undertaken.

4. **Quantify the effect of the spinal cord model on brain tissue deformation and motion in impact scenarios.** Tissue-level strains within the brain tissue and brain stem tissue were calculated and compared between the models with and without the implemented spinal cord model. Metrics including maximum principal strain, proposed cumulative strain distribution curve, or volume weighted average ratio of the maximum principal strain were utilized to quantify the strains within the neural tissues.

1.3 Thesis Organization

This thesis is organized into seven chapters, including the Introduction (Chapter 1). Chapter 2 summarizes the relevant background literature (Figure 1.2) that includes an overview of the spinal cord tissue anatomy and physiology, a summary of the mechanical properties of cervical neural tissues from the existing literature, followed by a brief review of contemporary HBM and existing FE spinal cord and head models. Lastly, a summary of metrics used to predict neural tissue injuries is outlined. Chapter 3 introduces an optimization methodology that was used to fit non-linear hyper-viscoelastic and hyperelastic material models to the tissue level compression data of the spinal cord tissue and tensile data of the pia mater. Two independent validation cases were then recreated in the FE environment to assess model performance. Chapter 4 presents an analysis of different numerical methods used to model fluid structure interaction that occurs between the dura mater, cerebrospinal fluid, and spinal cord during spinal cord compression. This comparative investigation was conducted towards an intended goal of implementation of the CSF into the GHBMC M50 Head-Neck model. Chapter 5 presents the development and evaluation of the 3D geometries and mesh of the cervical spinal cord and adjacent neural tissues for implementation into the GHBMC M50 Head-Neck model. Chapter 6 examines the influence of the cervical spinal cord tissues on the corresponding brain tissue deformation during simulated impact cases. Two separate models of the GHBMC M50 Head-Neck model, one with the spinal cord included and one without, were simulated in different impact scenarios. Several tissue level strain metrics were used to evaluate the difference in the brain tissue deformation between the models. Moreover, brief analysis of the strains occurring in the spinal cord tissue was undertaken. Chapter 7 discusses the overall

conclusions of the work completed in this thesis, along with a summary of the limitations and goals for future work.
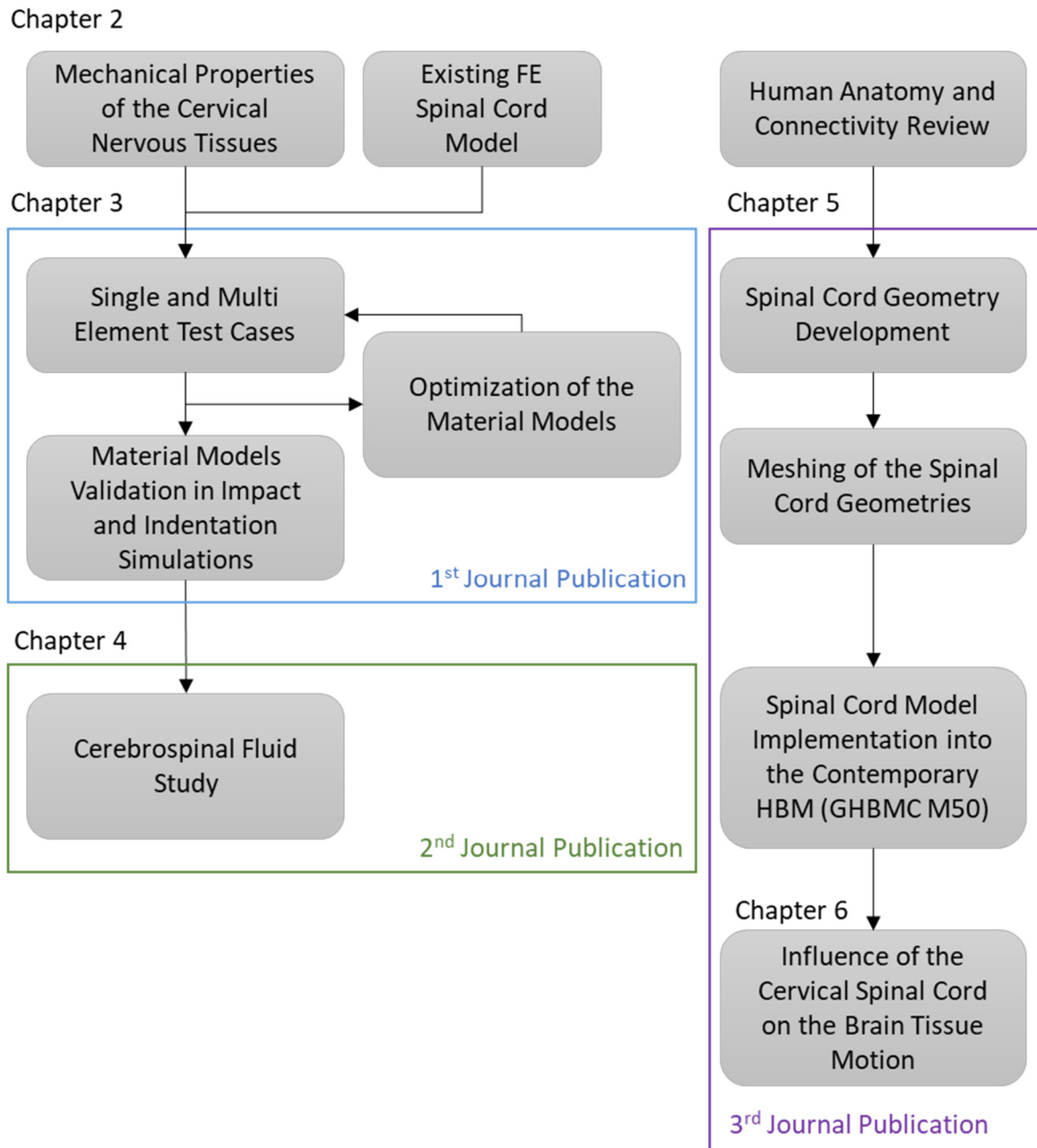
Figure 1.2: High-level chart illustrating the overall workflow of the thesis work completed.

Chapter 2

Background

Biomechanics is the part of engineering science that investigates and tries to understand mechanical loading on and within the living subject (Schmitt et al., 2019). Trauma biomechanics is a specialized discipline that investigates the mechanical loading that causes injuries, encapsulating many types of investigations for different injury scenarios. This interdisciplinary science uses a variety of methodologies to investigate injuries, including statistics, field studies, in-vivo and ex-vivo experimental models, accident reconstructions, standardized impact test procedures, and numerical methods like human body modelling (Jones and Clarke, 2018; Schmitt et al., 2019). Computational human body modelling is becoming more common and widely applicable in scientific and industrial applications. The main advantage of using the computational HBM is the ability to provide comprehensive insight into the mechanical response of the human body (Cronin, 2011). However, HBM require (1) an anatomical representation of the tissues of interest, (2) biofidelic representation of the mechanical properties, i.e., material models that represent and capture relevant material properties for the simulated impact condition, and (3) physical boundary conditions. In spinal cord modelling, the requirements translate to capturing the anatomical structures surrounding and grounding the spinal cord in the spinal canal and understanding the complex mechanical response of the spinal cord under loading. In this Background chapter, a summary of the anatomy of the spinal cord and adjacent tissues is described. Further, current achievements in FE modelling of the spinal cord are summarized, as well as descriptions of the contemporary HBM and FE head models. Lastly, the current metrics to predict damage to the neural tissues are outlined.

2.1 Anatomy, Physiology and Material Properties of the Cervical Neural Tissues

The cervical region of the spinal cord spreads from the brainstem at the foramen magnum to the seventh cervical vertebra (C7) (Standring and Gray, 2009). This section presents the anatomy of the central nervous system (CNS) tissues in the cervical region, including the spinal

9

cord, meninges, cerebrospinal fluid (CSF), and cervical neural ligaments. Frequently used anatomical planes and directions (Figure 2.1) are defined below for clear and consistent communication.
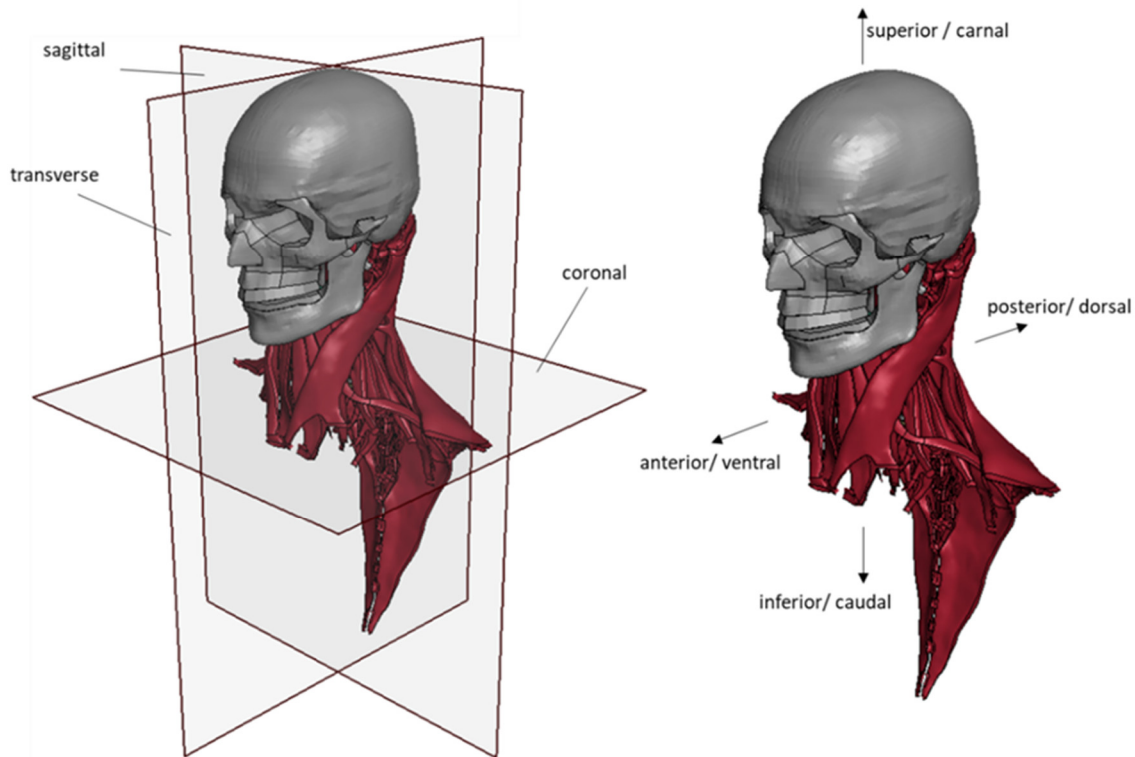
Figure 2.1: Anatomical planes and direction used in the thesis, presented using the human head and neck model.

2.1.1 Spinal Cord

The spinal cord is a long, flexible, nervous structure that occupies the spinal canal. The spinal cord is often classified into four regions along the length of the spine: cervical, thoracic, lumbar, and sacral (Standring and Gray, 2009). The spinal cord contains two types of neural tissues: the white matter and the gray matter. The white matter, which surrounds the gray matter, consists of sensory and motor axons and glial cells. The gray matter comprises neuronal cell bodies, dendrites, axons, and glial cells. The neuronal cell bodies in the gray matter are arranged in a very characteristic butterfly shape (Figure 2.2A). The primary function of the spinal cord is to transfer motor and sensory impulses between each receptor and the brain.

Disruption of nerve impulses between the brain and receptors exhibits itself as physical impairment. On average, the whole spinal cord is 45 cm long in males and 43 cm long in females. In the cervical region, it has a shape of a flattened cylinder in the anteroposterior direction, whereas in the thoracic and lower levels, it becomes more cylindrical (Watson et al., 2009). Average values for cervical cord geometry have been previously reported: a transverse cross-sectional area of 55 mm^2, anterior-posterior diameter of 6.0 mm, and median-lateral diameter of 11.7 mm (Fountas et al., 1998; Kameyama et al., 1996; Ko et al., 2004); however, variations in the values are observed between subjects and vertebral levels.
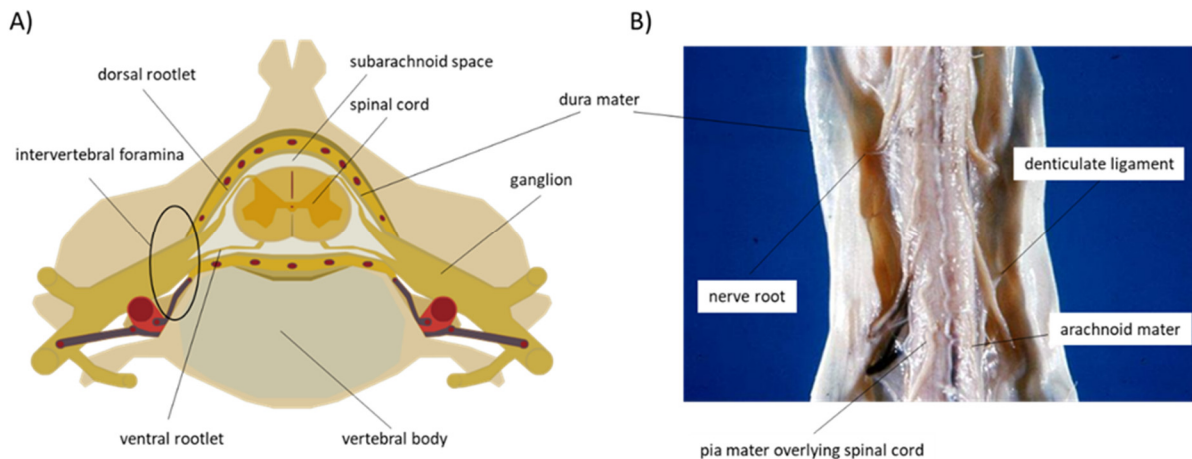
Figure 2.2: A) Transverse cross-section through a cervical spinal canal with highlighted nervous tissues (adapted from Wikimedia Commons). B) Anterior view of the isolated spinal cord tissue, wrapped in dura mater (adapted from Wikimedia Commons).

2.1.2 Spinal Nerves

In humans, there are 31 pairs of spinal nerves: 8 cervical, 12 thoracic, 5 lumbar, 5 sacral, and 1 coccygeal. Cervical nerves control the head, neck, and part of the upper limbs (Standring and Gray, 2009). Nearly all the cervical nerve roots exit the spine above the corresponding vertebral body (e.g., the second nerve root pair exits above the C2 vertebra), except the C8 nerve that exits the spinal column below the C7 vertebrae. Cervical nerves from C3 to C8 exit the spinal column through the intervertebral foramina (Figure 2.2A). Each spinal nerve emerges from the spinal cord in the form of two rootlets, ventral and dorsal (Figure 2.2A). The two bundles

11

merge shortly within the subarachnoid space and exit the spinal column as one bundle (ganglion). The function of the nerve roots is to connect parts of the body to the spinal cord. The cervical nerves increase in diameter along with the vertebral level. The 1st cervical nerve root measures 1.5 mm in diameter, whereas the 6th measures 4.6 mm, on average. After the 6th vertebral level, the diameter of the nerve roots stays constant until reaching the sacral region (Liu et al., 2015).

2.1.3 Meninges of the Spinal Cord and Cerebrospinal Fluid

The spinal cord and nerve roots are enclosed with three membrane-like tissues called meninges (lat. membrane). Their primary functions are to protect the spinal cord and the nerve roots and anchor the spinal cord in the spinal canal. Figure 2.2 represents the transverse cross-section over the human cervical vertebral canal and identifies spinal meninges: the dura mater (the outermost), the arachnoid mater (the intermediate), and the pia mater (the innermost). The meninges are separated by the subarachnoid and subdural spaces (Nicholas and Weller, 1988).

Cervical Pia Mater

The pia mater is a thin fibrous tissue that wraps the spinal cord tightly and penetrates the anterior median fissure (Table 2.1). Its primary function is to protect the spinal cord and provide connections between the spinal cord and the dura mater via the denticulate ligaments. The pia mater is impermeable; therefore, the cerebrospinal fluid, enclosed between the dura mater and the pia mater, creates the fluid cushion for the spinal cord (Standring and Gray 2009). The pia mater protects the dorsal and ventral nerve roots until they pierce the dura mater (Watson et al., 2009). The pia mater comprises two distinct types of tissues: subpial and cellular. Subpial tissue is mainly composed of collagen fibres aligned in the longitudinal direction (Reina et al., 2004) and separates the cellular layer from neurological cells.

Table 2.1: Summary of the pia mater thickness reported in the literature.

Reference	Species	Body region	Reported thickness [μm]
Ozawa et al., 2004	leporid	cervical	12
Ramo et al., 2018	ewe	cervical	200
Kimpara et al., 2006	porcine	cervical	130 to 270
Jin, 2009	bovine	cranial	23.6
Reina et al., 2004	human	spinal	Cellular Pia 8 to 15 Subpial 130 to 200

Cervical Arachnoid Mater

The arachnoid mater is fine, thin, fibrous-like tissue, that is aligned with the dura mater. It is named after its spider web-like appearance (Watson et al., 2009). It is connected to the pia mater by fine trabeculae tissue (Nicholas and Weller, 1988). The spinal arachnoid mater connects with the cervical dura mater and creates unity for the spinal cord and the nerve roots.

Spinal Dura Mater

The dura mater, which is a dense fibrous tissue, encloses the spinal cord, pia mater, arachnoid, and CSF. It is connected to the cranial dura mater at the level of the foramen magnum. The dura mater covers nerve roots up to the dural cuff space, where it blends with connective tissue (Watson et al., 2009). In contrast to the cranial dura mater that consists of two layers, the spinal dura mater consists of one layer (Newell, 1999). Each layer comprises approximately 80 dural laminas, each 5 μm thick (Reina et al., 2015). Other histological studies have identified that the thickness of the dura mater from different species varies, with reported values ranging between 0.08 to 0.40 mm (Table 2.2). The systematic variability in thickness is observed between the anterior and posterior sides. The posterior side of the dura mater is nearly twice as thick as the anterior side (Kwon et al., 2018). The dura mater is impermeable tissue, which creates an outer boundary membrane that encloses the CSF.

Table 2.2: Summary of the dura mater thickness reported in the literature.

Reference	Species	Body region	Thickness [mm]
Shetye et al., 2014a	ovine	cervical	0.35
Mazgajczyk et al., 2012	porcine	cervical	0.08
Reina et al., 2015	human	spinal	0.25 to 0.4
Kwon et al., 2018	human	cervical	0.38
Hong et al., 2011	human	thoracic	0.32

The dura mater is mostly made up of collagen fibres; however, elastin fibres are also present in a lesser portion (Reina et al., 2015). Elastin fibres provide flexibility during movement, whereas the collagen bundles increase the strength of the meninx. Many studies performed histological observations on the spinal dura mater by investigating the collagen and elastin fibres orientation (Ruzna et al., 1992; Maikos et al., 2008; Persson et al., 2010). Yet, there is no consensus regarding the general fibre orientation. Ruzna et al. (1992) reported that fibres are aligned longitudinally, the same observation was reported by Maikos et al. (2008). However, Reina et al. (2015) reported various orientations of elastin and collagen fibres in the laminas of the human cervical dura mater. Maikos et al. (2008) hypothesized that the preferred orientation of the collagen fibres in the dura mater is species sensitive and may depend on the natural position of the subject upright or supine. Persson et al. (2010) observed that the collagen fibres are more crimped in the longitudinal direction than in the circumferential direction.

Cerebrospinal Fluid

CSF is a transparent liquid that surrounds the human brain and the spinal cord. It is enclosed between the pia and dura mater and fills the subarachnoid space. CSF occupies a volume of approximately 150 millilitres in total. Around 25 ml is located in ventricles, whereas 125ml is distributed within cranial and spinal subarachnoid space (Telano and Baker, 2022). The human body produces around 500 millilitres of CSF daily; thus, it is replaced nearly 2.5 times every 24 hours (Palastanga et al., 1998). The CSF is in constant circulation and nourishes the spinal cord and brain tissue (Standring and Gray, 2009). The flow of CSF can be characterized by

Reynold's number raging from 150 to 400 at peak velocities of 0.25 m/s, and pulsate flow to and from the brain cavity, with an average velocity ranging from 0.01 to 0.08 m/s (Alperin et al., 1996; Yardimci, 2000). The CSF layer was shown to play an important and protective role to the spinal cord. It was proven that the CSF layer reduced the degree of neural tissue compression during transverse insult into the spinal canal (Jones et al., 2008, 2012; Persson et al., 2009).

2.1.4 Cervical Nervous System Ligaments

CNS ligaments help anchor the spinal cord in the spinal canal and provide the necessary attachment of the spinal nerves in the extraforaminal magnum. The important ligaments are denticulate, dorsal meningovertebral, anterior dural, and extraforaminal.

Denticulate Ligaments

The denticulate ligaments are a pair of narrow strips made of fibrous tissue. Their primary role is to connect the spinal cord with the dura mater (Figure 2.2B). They occur bilaterally at the sides of the spinal cord and run between the spinal dorsal and ventral nerve roots. From each strip, 18 to 20 triangular extension pairs emerge, which connect the spinal cord with dura mater (Ceylan et al., 2012; Tubbs et al., 2001). The first pair of denticulate ligaments insert with the dura mater to the lateral rim of the foramen magnum. The last pair of ligaments occurs at the level of L2 (Tubbs et al., 2001). At the cervical level, triangular extensions were reported to be shorter (3-5mm) but thicker than in the thoracic or lumbar region (Ceylan et al., 2012; Tubbs et al., 2001). Ceylan et al. (2012) reported that the strip portion of the denticulate ligament consists of longitudinal collagen fibres, whereas the triangular extensions are primarily made of transverse and oblique fibres. The denticulate ligaments stabilize the spinal cord in the cervical region. Nam et al. (2014) showed that collagen fibres in the denticulate ligaments are oriented in a lateral-median direction.

Dorsal Meningovertebral Ligaments

The dorsal meningovertebral ligaments anchor the posterior side of the dural sack to the ligamentum flavum or to the lamina of the adjacent vertebra. The variation in the occurrence

between levels and subjects was observed (Shi et al., 2014, 2015; Chen et al., 2015). Most of those ligaments were found in the sagittal plane and oriented in a craniocaudal direction. The variation between subjects was acknowledged; however, a certain presence in all subjects was observed at C1-C2 and C4-C5 levels. Shi et al. (2014) reported that the dorsal meningovertebral ligaments were fused to the ligamentum flavum and were challenging to separate.

Anterior Dural Ligaments

The anterior dural (Hofmann's) ligaments connect the dural sack to the anterior wall of the vertebral canal or to the posterior longitudinal ligament (Tardieu et al., 2016). The primary function of those ligaments is to provide a supportive and anchoring role to the dura mater. The anterior dural ligaments were observed between the C7 and L5 levels (Wadhwani et al., 2004). The spatial orientation of the anterior dural ligaments progressively changes with the spinal segment. In the cervical region, those ligaments are oriented in a craniocaudal direction. Then, in the thoracic region, the orientation changes to a more vertical one. And finally, in the lumbar region, they are oriented craniocaudally again. The lack of the anterior dural ligaments in the upper cervical level might suggest higher mobility of the spinal cord in the neck.

Extraforaminal Ligaments

The extraforaminal ligaments (ELF) are entities that anchor the spinal nerves in the extraforaminal magnums. They are present at all levels in the cervical spinal cord and occur on the dorsal and ventral sides. At each level, ELF have different spatial orientations, structures, and connections to the adjacent vertebrae. Histological investigation revealed that ELF are mainly composed of parallel collagen fibres (Kraan et al., 2011). Kraan et al. (2011) identified that the main mechanical functions of the extraforaminal ligaments are to decrease longitudinal tension and provide support to the nerve roots. Moreover, they protect the nerve from being pushed against the superior and inferior transverse processes of the adjacent vertebrae. Shi et al. (2015) reported that ELF secure the nerve roots in the center of the

16

extraforaminal magnum; therefore, the possible protective function against compression was identified.

2.2 Mechanical Properties of the Cervical Neural Tissues

Biological tissues demonstrate a highly non-linear material response with significant viscous (deformation rate) effects. Due to their complex internal structure, biological tissues often exhibit an asymmetric and anisotropic response under mechanical loading. Encapsulating the mechanical properties of the biological tissues in the constitutive models is challenging.

Biological tissues in the human body are classified as hard and soft tissues. The mechanical response of the soft tissues (e.g., muscles, ligaments, fat, brain, spinal cord, meninges, etc.) is associated with their microstructure and composition (Fung, 1993). Soft tissues are mainly composed of different types of collagen fibres. Individual collagen fibres exhibit a linear force-displacement response. However, non-linear force-displacement is observed in the soft tissue macrostructure mainly due to their hierarchical organization (Fung, 1993) (Figure 2.3A). Typically, the mechanical response of soft tissues is viscoelastic (Figure 2.3B), which means the total response of the material is composed of time-dependent (viscous) and time-independent response (Lakes, 2009). As a result of viscoelastic behaviour, soft tissues display stress relaxation phenomena, creep, hysteresis in cycling loading (energy loss) and increase in stiffness with an increase of strain rate (Fung, 1981).
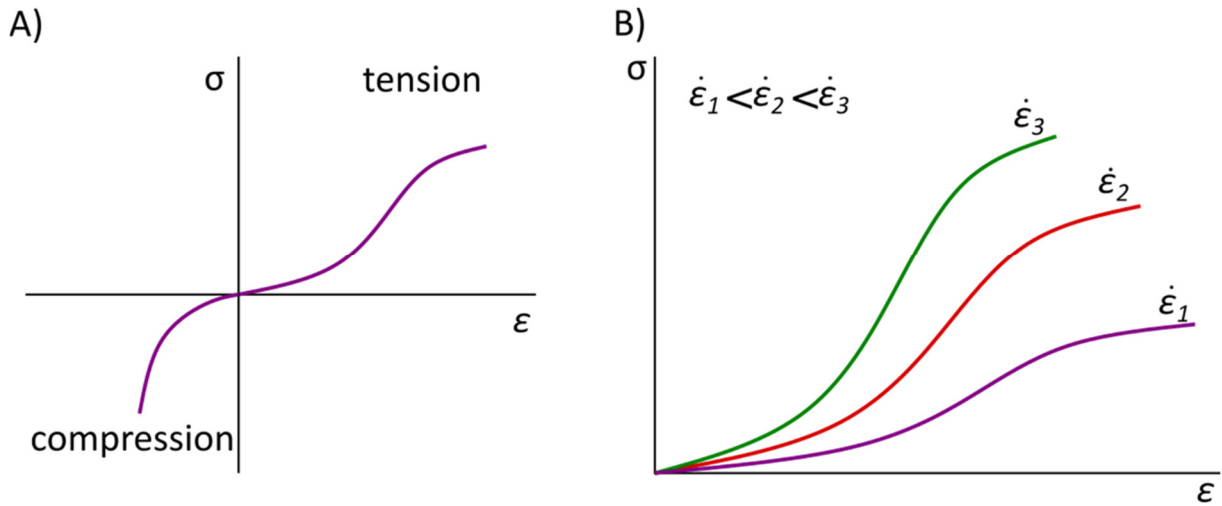
Figure 2.3: Important characteristic mechanical responses of the soft tissues A) nonlinearity and asymmetry in tension and compression B) viscoelastic stiffening.

Biological tissues are challenging to characterize from the mechanical point of view. The experiments are either performed in-vivo (Chang et al., 1988; Hung et al., 1981) or ex-vivo (Bilston and Thibault, 1995; Clarke et al., 2009; Fradet et al., 2016); in both methods limitations are embedded. Results from ex-vivo testing are influenced by the lack of perfusion pressure (Bilston and Thibault, 1995; Fiford and Bilston, 2005; Ramo et al., 2018), fluid loss during the test, tissue dehydration, degradation of the tissue (Galford and McElhaney, 1970), and complex specimen preparation (Sparrey and Keaveny, 2009). Whereas the in-vivo method often requires unique testing apparatus (Chang et al., 1988; Ramo et al., 2018) and complex specimen preparation, which is highlighted as an artifact that can influence the results of the experiment (Hung and Chang, 1981).

Post-mortem time plays an essential role in testing neural tissues (Galford and McElhaney, 1970). Specimens of the spinal cord that were tested 72 hours after animal sacrifice exhibited a stiffer response comparted to tests 12 hours after death (Oakland et al., 2006). A similar observation was reported by Chang et al. (1988), who highlighted that after 4.5 hours of feline sacrifice the pseudo elastic modulus of the spinal increased by 150%. In contrast, Singh et al. (2019) observed progressive reduction in stiffness of the porcine brain tissue specimens that

were stored in the room temperature for 24 and 48 hours. The same trend was observed by Bilston and Thibault (1995). Tissue dehydration was reported as one of the important factors that alters the results of the mechanical testing of living tissues. Hung and Chang (1981) observed an increase in stiffness by up to 1500% of the spinal cord by letting it dry for one hour.

2.2.1 Spinal Cord

Spinal cord tissues exhibit a strong non-linear stress-strain response under dynamic loading with clear direction-dependent phenomena (Sparrey and Keaveny, 2011). Moreover, viscoelastic stiffening (i.e., increase in stiffness with increase of rate of deformation) was also observed (Hung et al., 1982; Jannesar et al., 2016; Ramo et al., 2018). Most of the studies highlighted a non-linear response of the spinal cord specimen under deformation. A typical "J" shape force-displacement (stress-strain) curve was reported (Bilston and Thibault, 1995; Fiford and Bilston, 2005). The anisotropic and asymmetric character of the spinal cord was also observed (Sparrey and Keaveny, 2011). Naturally, CNS tissues exhibit typical effects for living tissues, particularly change in mechanical properties with temperature, wide scatter of experimental results in the same experiment, and variability in mechanical properties between the specimen anthropometrics (Bilston and Thibault, 1995; van Noort et al., 1981; Singh et al., 2019; Clarke et al., 2009) and region of harvesting (Bilston and Thibault, 1995).

Mechanical properties of the spinal cord have been widely examined ex-vivo (Bilston and Thibault, 1995) and in-vivo (Hung and Chang, 1981; Hung et al., 1982)). Most specimens are excised from animals: rodent (Clarke et al., 2009; Fiford and Bilston, 2005; Ozawa et al., 2004), bovine (Hall et al., 2006; Ichihara et al., 2001), porcine (Shetye et al., 2014; Sparrey and Keaveny, 2009), as well as a few studies which have used primate specimens (Bilston and Thibault, 1995; Jannesar et al., 2018) for the mechanical tissue characterization. The spinal cord white matter was more frequently examined (Jannesar et al., 2018; Jannesar et al., 2016; Sparrey and Keaveny, 2011) than the gray matter (Ichihara et al., 2001; Ozawa et al., 2001).

Researchers have often included the pia mater with the spinal cord and refer to that as the "spinal cord"; therefore, the reported spinal cord properties may be confounded with multiple tissue effects (Ramo et al., 2018). This could explain the wide range in the reported stiffness values, ranging from 3.4 kPa (Ozawa et al., 2001) to 1.37 MPa (Bilston and Thibault, 1995). Mazuchowski and Thibauld (2003) reported a significant difference in a pseudo-elastic modulus in the specimens with pia intact and removed, with similar observations reported by Ozawa et al. (2001)

Some investigated the mechanical properties of the spinal white matter and gray matter separately studies (Ozawa et al., 2001; Ichihara et al., 2001). Ozawa et al. (2001) tested specimens with the pipette aspiration method while Ichihara et al. (2001) performed a tensile test on bovine specimens. Ozawa et al. (2001) reported that there was no significant mechanical difference between the spinal white and gray matter. On the other hand, Ichihara et al. (2001) showed explicitly that the gray matter was stiffer and more fragile (rupture occurred at a lower stretch) than the white matter. This conclusion discrepancy can be explained with the fact that the authors used different test methods, which resulted in different strains. At very low strains the stiffness of white and gray matter was observed to be the same. Ichihara et al. (2001) solely reported values of Poisson's ratio 0.42 for the white matter and 0.40 for the gray matter. Literature that characterized mechanical properties of the spinal cord is summarized in Table 2.3.

Table 2.3: Summary of the studies that mechanically characterized spinal cord.

Reference	Research objective and method	Number of specimens	Strain rates Maximum strain	Significant findings
Hung and Chang, 1981	In-vivo tensile test of the canine spinal cord with pia mater intact in the craniocaudal direction	10	0.002 s^{-1} up to 50%	The initial stiffness of the spinal cord was found to be 2 to 3 kPa. The mean pseudo-Young's modulus was 0.265 MPa. Full recovery of motoric function was observed for elongation up to 50%.
Hung et al., 1982	In-vivo compression test of the cat spinal cord with pia	31	Quasi-static	Non-linear force-displacement behaviour was observed,

	mater in the transverse direction			hysteresis was observed in the loading-unloading cycle.
Chang et al., 1988	In-vivo tensile-relaxation test of the cat spinal cord with pia mater in the craniocaudal direction	23	$0.003\ s^{-1}$ up to 11%	Viscoelastic relaxation of the spinal cord tissue was observed. Average pseudo-Young modulus 0.230 MPa.
Bilston and Thibault, 1996	Ex-vivo uniaxial tensile test of the human cervical spinal cord in the craniocaudal direction	13	0.068, 0.14, and $0.21\ s^{-1}$ up to 9%	Viscoelastic behaviour of the spinal cord with pia mater. Long time < (1 min) relaxation response was highlighted. Average pseudo Young's modulus of 1.02 ($0.068\ s^{-1}$), 1.17 MPa ($0.14\ s^{-1}$) and 1.37 MPa ($0.21\ s^{-1}$).
Ichihara et al., 2001	Ex-vivo tensile test of bovine cervical white and gray matter in the craniocaudal direction	6	$0.05\ s^{-1}$ up to 150%	Gray matter was found to be more rigid and rupture earlier than white matter.
Ozawa et al., 2001	In-situ pipette aspiration measurement of the stiffness of the rodent (rabbit) cervical white and gray matter	N/A	N/A	No statistical significance was observed in stiffness between white and gray matter for low strains.
Mazuchowski and Thibault, 2003	Ex-vivo tensile test of the human spinal cord with pia and without	18	0.1, 1, $10\ s^{-1}$ up to 20%	Presence of the pia mater significantly changed modulus of the specimen.
Ozawa et al., 2004	Ex-vivo tensile and compression test of the rodent (rabbit) spinal cord with and without the pia mater in the anterior-posterior direction	N/A	N/A	The spinal pia mater enhances the recovery of the specimen back to the original shape, with pseudo Young's modulus of the pia mater E = 2300 kPa compared to spinal cord 5 kPa.
Fiford and Bilston, 2005	Ex-vivo uniaxial elongation with the relaxation of the rodent spinal cord in the craniocaudal direction	52	0.002, 0.02, $0.2\ s^{-1}$ up to 5%	The typical "J" shape stress-strain response curve was observed. The failure strain of the rodent spinal cord was found to be approximately 12 %.
Oakland et al., 2006	Ex-vivo uniaxial tensile test on the bovine spinal cord	36	$0.24\ s^{-1}$	Stiffness of the spinal cord depends on the time testing after harvesting.

	with pia mater in the craniocaudal direction.			
Clarke et al., 2009	Ex-vivo uniaxial tensile test on the neo-natal spinal cord with pia mater in the craniocaudal direction.	34	0.2, 0.02, 0.002 s^{-1}	The neonatal spinal cord was found to be softer than the adult one. The neonatal specimens did not show strong sensitivity to the changes in the strain rate.
Sparrey and Keaveny, 2009	Ex-vivo unconfined compression of porcine spinal cord tissue.	45	5 and 0.05 s^{-1} up to 40%	The flash freeze of the specimen reduced the variability of the group and did not change the average response.
Sparrey and Keaveny, 2011	Ex-vivo unconfined compression of porcine spinal cord tissue.	104	0.005, 0.05, 0.5, and 5 s^{-1} up to 40 %	Spinal cord white mater exhibits asymmetry in response between compression and tension.
Shetey et al., 2014	Ex-vivo relaxation and dynamic cycling test of porcine spinal cord	N/A	0.1 and 1 s^{-1} up to 5 %	Non-linear viscoelastic mechanical properties of the porcine spinal cord were highlighted.
Ramo et al., 2018a	Ex-vivo and in-vivo relaxation and dynamic cycling test of the porcine spinal-cord	6	0.1 and 1 s^{-1} 5 %	Ex-vivo specimens displayed grater stiffness and viscoelastic relaxation compared to in-vivo samples.
Jannesar et al., 2018	Ex-vivo unconfined compression of the nonhuman primate spinal cord white matter in the transverse direction	65	0.32, 2.83, 25.74, 77.22 s^{-1} up to 45%	Viscoelastic characterization of spinal cord white matter and high strain rates and high strains.
Ramo et al., 2018b	Ex-vivo tensile test of the ewe spinal cord - pia - arachnoid – construct.	8	0.016, 0.0016, 0.00016 s^{-1} 5%	The contrast of stiffness between meninges and spinal cord was observed. The spinal cord rigidity and ability to recover from deformation come from the stiffness of the pia-arachnoid-complex.

2.2.2 Pia Mater

Previous studies have characterized the mechanical properties of pia mater from various species (bovine, canine, porcine). In most studies, the pia mater was tested with the spinal cord as a complex (Clarke et al., 2009; Fiford and Bilston, 2005; Ozawa et al., 2004) or with the arachnoid mater as the pia-arachnoid-complex (PAC) (Jin, 2009; Jin et al., 2011; Mazuchowski and Thibauld, 2003; Ramo et al., 2018). Only a few studies were performed for mechanical characterization of the test pia mater alone (Kimpara et al., 2006; Mazuchowski, 2001) (Table 2.4). Jin, 2009 performed a tensile test on the bovine cranial pia-arachnoid complex specimens at the four-strain rates (0.05 s^{-1}, 0.5 s^{-1}, 5 s^{-1}, and 100 s^{-1}). Obtained stress-strain curves were characteristic for a rich collagen fibre tissue, with four regions observed: toe, linear, traumatic and post-failure (Fung, 1981).

Table 2.4: Summary of the studies that mechanically characterized pia mater.

Reference	Research objective and method	Number of specimens	Strain rates Maximum strain	Significant contribution
Ozawa et al., 2004	Ex-vivo transverse compressions of the rodent cervical spinal cord with and without pia mater	N/A	N/A	Calculation of the elastic modulus of the pia mater in the transverse direction.
Kimpara et al., 2006	Ex-vivo tensile elongation of the porcine cervical spinal pia mater harvested from three different regions	52	0.5, 0.05, 0.005 up to 20%	First viscoelastic characterization of the pia mater, the regional variability in stiffness was observed.
Mazuchowski and Thibault, 2003	Ex-vivo tensile test of the human cervical spinal cord with and without the pia mater	18	$0.1, 1, 10 \text{ s}^{-1}$ up to 50%	Stiffness of the spinal cord with pia mater was calculated to be a magnitude greater than the spinal cord alone.
Jin, 2009	Ex-vivo tensile elongation of the cranial bovine pia-arachnoid complex	40	0.05, 0.5, 5, and 100 s^{-1} up to 50%	Highly non-linear character and non-linear viscoelastic mechanical behaviour of PAC was observed.

Ramo et al., 2018	Ex-vivo tensile test of cervical ewe pia-arachnoid-complex in the axial direction	8	0.016, 0.0016, 0.00016 s^{-1} 5%	Pia-arachnoid complex contributes to the tensile and viscous properties of the whole spinal cord structure.

2.2.3 Arachnoid Mater

Ommaya (1968) suggested that the arachnoid mater as a fine tissue does not contribute significantly to the biomechanical response of CNS tissues. There are no studies that present the mechanical properties of the arachnoid mater itself.

2.2.4 Dura Mater

The dura mater is the outermost meninx, and it is the thickest one. Histological assessment suggested that fibres are oriented in the craniocaudal direction in the cervical dura mater. Importantly, alignment to one direction suggests that the strain-stress relationship is non-linear and mechanical properties of the tissue are direction-dependent (anisotropic) (Fung, 1993). The spinal dura mater demonstrates non-linear mechanical response typical for collagen-rich tissue (Maikos et al., 2008; Mazgajczyk et al., 2012; Persson et al., 2010; Runza et al., 1999; Shetye et al., 2014b). Shetye et al. (2014b), Mazgajczyk et al. (2012), Persson et al. (2010), and Runza et al. (1999) tested spinal dura mater in the longitudinal and circumferential directions (Table 2.5). Results from all studies indicated that the spinal dura mater exhibits orthotropic mechanical properties. Ruzna et al. (1999) and Persson et al. (2010) highlighted that the toe region of the spinal dura mater in the longitudinal direction was significantly greater than in the circumferential one. Whereas the tangent modulus of the linear region was stiffer in the longitudinal direction than in the circumferential one. Previous research has correlated a greater toe region with increased crippling of the collagen fibers (Ruzna et al., 1999, Persson et al., 2010). Persson et al. (2010) tested cervical dura mater at three strain rates, 0.01 s^{-1}, 0.1 s^{-1}, and 1 s^{-1}. While no significant effect, there was a trend towards increased stiffness in higher strain rates.

Table 2.5: Summary of the studies that mechanically characterized dura mater.

Reference	Research objective and method	Number of specimens	Strain rates Maximum strain	Significant findings
van Noort et al., 1981	Ex-vivo uniaxial tensile test of the human dura mater in the axial direction	24	1.25 s^{-1} 25%	Glycerol is an adequate medium to preserve dura mater without changing mechanical properties. Wide range of tensile strength in tested specimens of the dura mater was observed.
Runza et al., 1992	Ex-vivo uniaxial tensile test of the human dura mater in the longitudinal and circumferential direction	N/A	N/A up to 90%	Electron microscopy investigation revealed that the collagen fibres are longitudinally oriented in the dura mater.
Maikos et al., 2008	Ex-vivo uniaxial tensile test of the rodent spinal dura mater longitudinal direction	N/A	0.0014 and 19.42 s^{-1} up to 50%	Typical "J" shaped stress-strain response of the dura mater was observed using histological investigation of rodent dura mater.
Persson et al., 2010	Ex-vivo uniaxial tensile test on the bovine cervical dura mater in the longitudinal and circumferential direction	38	0.01, 0.1 and 1 s^{-1} N/A	No significant effect of the strain rate on the stiffness of the dura mater was observed. Collagen fibres were less crimped in the circumferential direction.
Mazgajczyk et al., 2012	Ex-vivo uniaxial tensile test of the porcine dura mater in the longitudinal and circumferential direction	250	N/A	Detailed mechanical characterization of the porcine dura mater in the longitudinal and circumferential direction. A sensitivity study based on place of harvesting was conducted (dorsal or ventral side).
Shetye et al., 2014b	Ex-vivo uniaxial and biaxial test of the ovine dura mater in the longitudinal and circumferential direction	N/A	N/A	The orthotropic character of the dura mater was confirmed.

2.2.5 Cerebrospinal Fluid

The mechanical properties of CSF are very similar to a saline solution containing 0.9% NaCl (Ellis et al., 1992). CSF is a Newtonian fluid; therefore, its viscosity depends on the temperature, pressure, and chemical composition. Density and viscosity of the CSF at 37º Celsius degrees are 1.0003-1.0007 g/ml (Richardson and Wissler, 1996) and 0.71 to 0.76 mPa*s (Brydon et al., 1995), respectively.

2.2.6 Neural Ligaments

Existing literature data characterizing the mechanical properties of the eight cervical pairs of denticulate ligaments is limited. Tunturi (1978) performed one of the first tests on canine denticulate ligaments. The test was done by applying incremental masses on anesthetized animals. Moreover, it was estimated that the failure elongation and mass of the denticulate ligaments was approximately 9% and 100g (or 0.98N), respectively (Tunturi, 1978). Tubbs et al. (2001) examined human denticulate ligaments and determined the force to create tautness at a different level of the spine in various directions. The range of the forces to cause an avulsion was reported between 0.3 to 0.83N. Some studies (Polak-Kraśna et al., 2019; Polak et al., 2014; Polak et al. 2016) characterized porcine denticulate ligaments in series of tensile tests. Polak-Kraśna et al., (2019) found that the denticulate ligaments, despite their low braking force (appx. 1N), play an important role in stabilizing and positioning of the spinal cord in the spinal canal due to regular occurrence at each spinal level. The reported ligament mechanical behaviour was consistent with typical stress-strain curves with three regions: toe, linear, and post-failure (Mattucci and Cronin, 2015) (Figure 2.4). Mechanical properties of extraforaminal ligaments, dural anterior ligaments, and dorsal meningovertebral ligaments have not been reported in the literature.
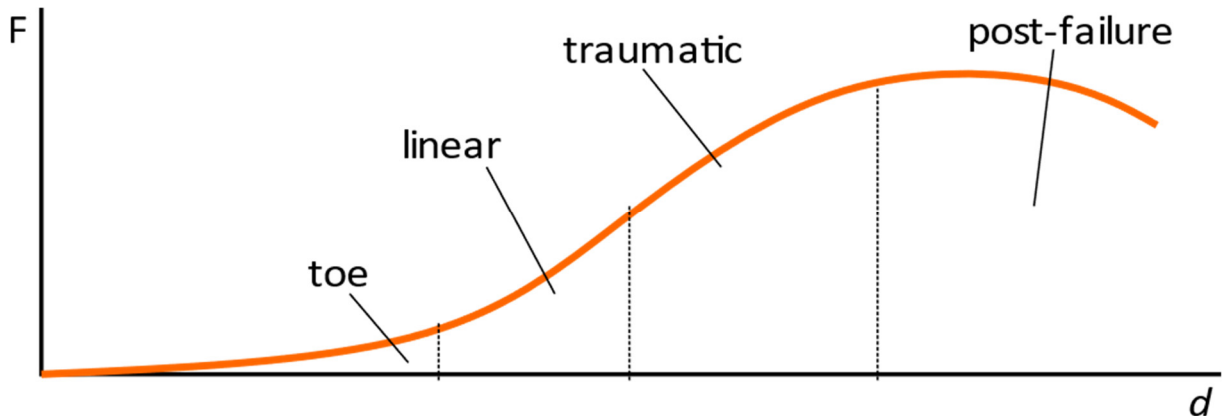
Figure 2.4: Typical mechanical force-displacement response of the ligament with distinct four regions: toe, linear, traumatic, and post-failure.

2.3 Computational Modeling of the Cervical Neural Tissues

To date, there have been several attempts to develop FE models of the spinal cord (Table 2.6). The primary challenge in modeling the cervical neural tissues has been identifying appropriate material models (Jones and Clarke, 2018; Yang et al., 2018). Most of the models developed have used linear elastic models to represent the non-linear mechanical response of the spinal cord and meningeal tissues (Czyz et al., 2011; Greaves et al., 2008; Jannesar et al., 2016; Li and Dai, 2009; Wilcox et al., 2004). Moreover, the geometry of the spinal cord was often simplified to a cylinder or elliptical tube. Incorporation of the CSF layer is also challenging; most of the current studies either have not included fluid structures in their model or instead have included a simplified representation using deformable solid elements. Some of these works (Czyz et al., 2011; Greaves et al., 2008) have validated their FE models against static tension and compression experimental data (Czyz et al., 2011; Hung and Chang, 1981; Hung et al., 1982; Tencer et al., 1985) as well as physical surrogate model data (Bilston, 1998); yet, this validation does not adequately capture the dynamic (viscoelastic) response of the spinal cord to impact. Persson, et al. (2011b) validated their spinal cord model against dynamic experimental data (Persson et al., 2009; Persson et al., 2011a, 2011b); however, the mechanical properties used for the spinal cord were simplified to hyperelastic behaviour and pia mater to linear elastic behaviour.

27

Previous computational studies investigating spinal cord compression demonstrated that FSI modeling of the CSF using the Arbitrary Lagrangian-Eulerian (ALE) numerical approach showed good correlation with reported experimental data (Persson, et al., 2011a, 2011b; Khuyagbaatar et al., 2014; Fradet et al., 2016; Diotalevi et al., 2020). However, the ALE method was reported to be four times more computationally expensive compared to the traditional Lagrange approach when used in simplified models (Tabiei and Chowdhury 2004). Thus, such a method may be computationally prohibitive in full HBM (Mao et al. 2013). Another recent study (Jannesar et al. 2020) presented a detailed model of a subject specific cervical spinal column with the spinal cord surrounded by CSF and dura mater, using a Smoothed Particle Hydrodynamics (SPH) representation of the CSF. The model was comprised of a large number of SPH elements (small element size relative to contemporary HBM and it was acknowledged that the computation time was large (~100 hours per model), which would be prohibitive for use in many industrial and clinical modeling applications. The authors of this study identified a need for further validation of the SPH methodology, including using SPH implementation for simulation of impact scenarios. Another study modeled CSF as simple PV without fluid exchange (Stoner et al. 2020), while other studies have modeled the CSF using a Lagrange mesh along with a hyperelastic constitutive model (Jannesar et al., 2016). However, large compression and corresponding outflow of the CSF experienced during spinal cord impact may not be well captured by PV and Lagrange implementations. Other studies have chosen to exclude the CSF from spinal cord FE models and acknowledged it as a limitation of the spinal cord response predicted by their model (Bailly et al. 2020). In terms of the dura mater, most of the previous FE models simplified the mechanical properties to the dura mater to linear elastic behavior (Persson et al., 2011b; Fradet et al. 2016; Khuyagbaatar et al. 2016; Henao et al. 2018; Bailly et al. 2020; Diotalevi et al. 2020; Stoner et al. 2020), while some others have used a viscoelastic representation of this tissue (Jannesar et al., 2016; Jannesar et al. 2020). Although many individual previous studies have investigated various methods for representing the CSF and dura mater, no previous study has made a consistent quantitative comparison of the methods under the same simulation conditions, making the

specific findings of the CSF and dura mater implementation from each study challenging to compare.

Table 2.6: Summary of previously developed FE models that included spinal cord.

Reference	Model Description	Tissue	Material Law	Properties	Significance
Bilston, 1998	Investigation of various material parameters on the deformation pattern of the cervical spinal cord in hyperflexion, hyperextension, and axial compression using two-dimensional model.	Spinal Cord Brain tissues	Orthotropic, Elastic, Hyperelastic Viscoelastic Elastic	N/A $E = 0.3$ MPa	Material models play an important role in predicting stresses in strain in the spinal cord model.
Wilcox et al., 2003; Wilcox et al., 2004	Investigation of the burst fracture, in combination with experimental data using a 3-D model of vertebrae and two intervertebral discs.	Spinal Cord Dura Mater	Linear Elastic Anisotropic Elastic	$E = 1.3$ MPa $E_{xx} = 142$ MPa, $E_{yy} = 142$ MPa, $E_{zz} = 0.7$ MPa.	Maximum compression of the spinal cord occurs at the moment of impact, and it is not represented by the final position of the bony fragment in computed tomography images.
Kimpara et al., 2006	Validation of the Total Human Model for Safety (THUMS)	White and gray matter CSF Pia mater Dura mater	Hyperelastic (lookup table) Linear elastic Linear elastic Orthotropic Elastic	Direct curves from Ichihara et al., 2001 0.16 kPa $E=39.3$ MPa $E_{xx} = 44.1$ MPa $E_{yy}=43.35$ MPa	THUMS model validation
Greaves et al., 2008	Investigation of three injury patterns from the spinal column - spinal cord interaction	Spinal Cord Dura Mater	Linear elastic Linear elastic	0.26 MPa $E = 5$ MPa	Three patterns of the spinal cord injury: transverse contusion, vertebra dislocation, and distraction were investigated in simple 3D model.
Maikos et al., 2008	Investigation of the injury pattern during weight drop test on the rat spinal cord	Spinal cord Dura mater	Hyper-Viscoelastic (Ogden) Hyper-Viscoelastic (Ogden)	N/A N/A	The model predicted stresses and strains in the rat spinal cord after weight drop test; however, material coefficients of the

		CSF	Hyperelastic (Mooney-Rivlin)	G = 134 Pa; C01 = C10= 33.5 Pa	spinal cord were calibrated to match the validation case.
Czyz et al., 2008	Comparison of the strain in the FE model with MRIs from patients with SCIs.	White matter	Linear elastic	E=0.27 MPa	Personalized spinal cord model that provided insight to stains and stress in the spinal cord.
		Gray matter	Linear elastic	E=0.66 MPa	
		Pia mater	Linear elastic	E=2.3 MPa	
		Dura mater	Linear elastic	E=142 MPa	
		Denticulate ligament	Linear elastic	E=2.3 MPa E=100 MPa,	
Li and Dai, 2009	Investigation of the hyperextension injury utilizing an enlarged three-dimensional FE model of the spinal cord	White matter	Linear elastic	E=0.65 MPa ν = 0.4	Simulation of hyperextension injury revealed higher stresses in the anterior and posterior horns of gray matter. Patients with hyperextension injury may suffer hand weakness.
		Gray matter	Linear elastic	E= 0.277 MPa ν = 0.4	
Persson et al., 2011	Investigation of the protective role of the cerebrospinal fluid on the spinal cord transverse compression	Spinal Cord	Hyperelastic (Ogden)	μ= 2kPa, α= 9 ν = 0.4	CSF layer plays a salient protective role on the spinal cord during dynamic impacts.
		Dura Mater	Linear elastic	E = 80 MPa	
		CSF	Newtonian Fluid (ALE)	η = 0.001 Pa, ρ = 1000 kgm^{-3}	
Czyz et al., 2011	Development and validation of the accurate and universal human cervical spinal cord model	Gray matter	Linear elastic	E = 0.656 MPa	Stresses and strains were compared to clinical cases.
		White matter	Linear elastic	E = 0.277 MPa	
		Pia mater	Hyperelastic	N/A (look up curve model)	
Czyz et al., 2012		Dura Mater	Hyperelastic	N/A (look up curve model)	
		Denticulate ligament	Linear elastic	E = 2.3 MPa (shells) E = 100 MPa (solid)	
Jannesar et al., 2016	The three-dimensional model of the cervical spinal cord to validate transversely isotropic constitutive material	Spinal cord	User Material, hyper-viscoelastic with reinforced fibres in the craniocaudal direction		Transverse isotropy of the white matter resulted in different maximum principal strain compared to the
		CSF	Hyper-Viscoelastic (Ogden)		

| models for the spinal white matter. | Dura Mater | Hyper-viscoelastic (Mooney-Rivlin) | | isotropic model. Moreover, the mechanical properties of pia mater have a salient effect on the mechanical response of the model. |
| | Pia mater | Linear elastic | E = 39.3 MPa | |

2.4 Finite Element Full-Body Human Body Models

Mathematical representations of the human body for human safety have been in development since 1963 (Yang et al., 2006). The first-generation models of seated occupant (Bartz, 1972), side impact occupant (Padgaonkar and Prasad, 1979), child (Kaleps and Marcus, 1982), pedestrian (Verma and Repa, 1983), and occupant for submarining investigation (Deng, 1992) contained rigid parts lumped together with kinematic joints. Simultaneously, the Highway Safety Research Institute (now University Michigan Transport Research Center) developed a similar group of rigid models with kinematic joints (Robbins et al., 1971). However, their usage was limited due to restricted degrees of freedom (Yang et al., 2006).

The first elastic parts in the FE HBM were introduced in modified version of MADYMO model (Happee et al., 1998). In this model, the thorax was represented by several elastic bodies, whereas the rest of the anatomical components were implemented as rigid bodies. The model was assessed in frontal and rear cases, demonstrating that HBM have the potential to predict occupant response in multiple directions (i.e., omnidirectional) where physical dummy models are designed to predict kinematic behaviour in a preferred direction. The main intent for the simple rigid or partially rigid models was to investigate and predict kinematics of the human body in response to impact, with injury risk assessed at the body region level using kinematic or kinetic metrics (i.e., acceleration).

Second generation models began development with the increase in available computational power (Yang et al., 2006). At this generation, detailed development of thorax, cervical spine and head region is observed (Baudrit et al., 1999; Lizee et al., 1998). The development of the spine models was initiated in the 1990s. Dauvilliers et al. (1994) and Kleinberger (1993)

developed the first, simplified (idealized geometry) 3D model of the cervical spine. More anatomically correct models with detailed structures like ligaments and intervertebral discs were developed in late 1990's (Deng et al., 1999; Yang et al., 1998). Moreover, the main intent of second-generation models was to predict an injury at the regional (body organ) level.

The development of the third-generation models was initiated with the HUman MOdel for Safety (HUMOS) (Robin, 2001). It was the first model where the geometry and mesh were entirely based on a frozen cadaveric specimen measurement. More detailed anatomical models with soft abdomen tissues, like trachea, aorta, heart ventricles, were developed by Ruan et al. (2003) with targeted capabilities to predict injuries at the tissue level.

Currently, three adult computational HBMs have been adopted globally: the Global Human Body Models Consortium (GHBMC) (Gayzik et al., 2011; Barker and Cronin, 2021), the Total Human Model for Safety (THUMS) (Kimpara et al., 2006; Iwamoto et al., 2015; Kato et al., 2018), and the Virtual Vehicle Safety Assessment (ViVA) (Östh et al., 2016, 2017). Recently, a full-body HBM of a child was developed (Beillas et al., 2018). The complexity of these HBMs continues to evolve with interest in further enhancing biofidelity and accurate prediction of neural tissue deformation during impact (Table 2.7).

Table 2.7: Summary of the contemporary full-body HBMs.

Model	Size	Complexity and Validation	Neural Tissues	Spinal Cord Representation and Brain Stem Boundary Condition	Reference
Total Human Model for Safety (THUMS)	50th percentile Male	Detailed full body model with active musculature (nr of el. 1.9M)	Detailed cranial and spinal neural tissues implemented	Solid spinal cord elements are connected with a node-to-node connection to the brain tissue.	Kimpara et al., 2006; Iwamoto et al., 2015; Kato et al., 2018
Virtual Vehicle Safety Assessment Open-Source Human Body Models	50th percentile Female	A simplified full-body model with a detailed cervical spine and active muscle (nr of el. 318k)	In the current model, the neural tissues are not implemented	The cranial and spinal cavities are not filled with the neural tissues	Östh et al., 2016, 2017
Global Human Body Consortium (GHBMC) M50-O	50th percentile Male	Detailed full body with active musculature (nr of el. 1.9M)	Detailed cranial neural tissues, spine cavity empty	Magnum foramen is sealed with an elastic cap	Gayzik et al., 2011; Barker and Cronin, 2021
PIPER Child HBM	1.5 YO - 6 YO	Detailed scalable child HBM, with approximately 531k elements	Single part of cranial nervous tissues surrounded by cerebrospinal fluid and meninges	The brain tissue terminates at the foramen magnum.	Beillas et al., 2018

An important aspect of implementing cervical neural tissues in HBM is incorporating validated material models and anatomically correct geometries. Of the recognized full-body HBMs, only the current THUMS model (v6.1) has implemented cervical neural tissues, including the spinal cord, pia mater, arachnoid mater, and CSF; yet there are recognized limitations in terms of biofidelity. For example, the spinal cord in THUMS model utilizes the shear parameters that are 1000 times stiffer than the shear parameters used for the brain tissue. Representation of the nerve roots, which play an important boundary condition for the spinal cord, has also not yet been incorporated in the THUMS model, or any other known HBM. Further, the official THUMS manual (Toyota Motor Corporation and Toyota Central R&D Labs, 2021) has not reported any validation cases regarding motion and deformations of the cervical spinal cord and brain stem; therefore, it is unknown how well THUMS can assess SCI during dynamic

impact conditions. The GHBMC is the cooperative between seven automakers (Fiat Chrysler Automotive U.S. LLC, General Motors Co., Honda R&D Co., Hyundai Motor Co., Nissan Motor Corp. Ltd., PSA Peugeot-Citroën, and Renault S.A.) and one automotive part supplier (Joyson Safety Systems) that joins effort and individual knowledge in the development of the human body models for advance crash safety technology. The GHBMC M50-O is a key model that represents the 50th percentile male (Figure 2.5).
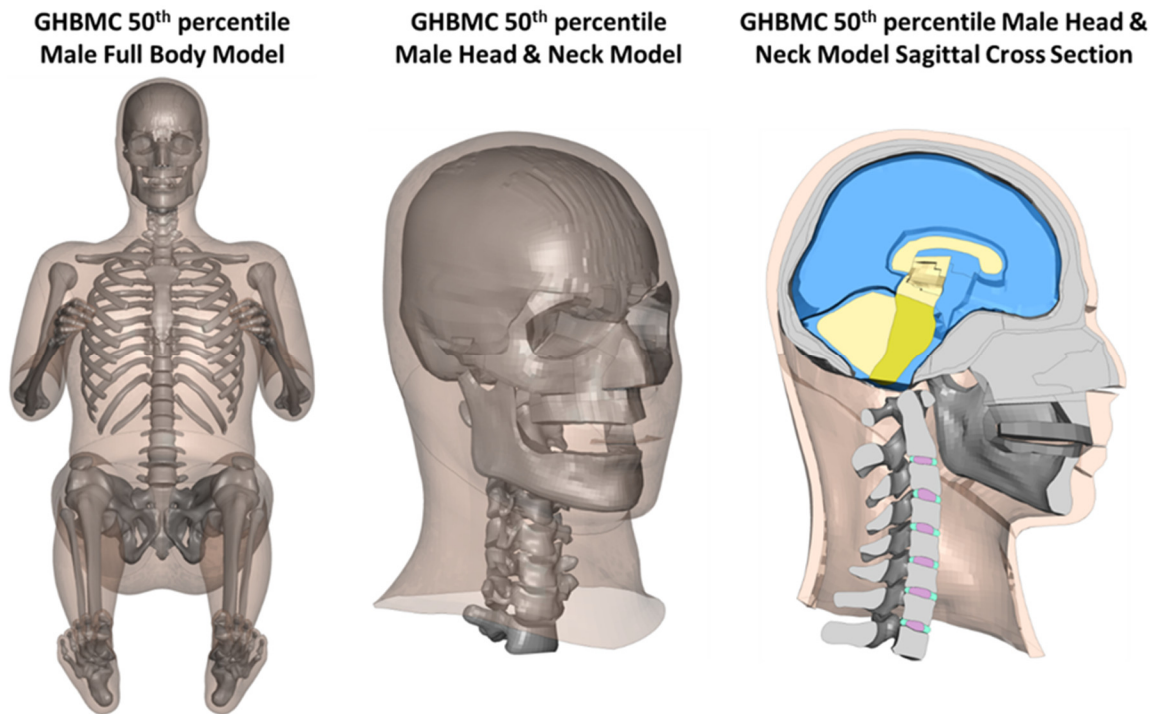
Figure 2.5: GHBMC 50th percentile male full body model, Head & Neck model, and sagittal cross section of Head and Neck model with highlighted end of cranial neural tissues.

The current version of the GHBMC 50th percentile male (GHBMC M50) model does not include spinal neural tissues, and the magnum foramen of the brain stem ends with an elastic cap, which seals the intracranial cavity. The GHBMC M50 model has been previously validated against numerous cases at multiple complexity levels, from single tissue evaluation through the component to the full body level. Within the neck region, 84 validation cases ensure a high level of biofidelity, including the motion segments (Barker et al., 2017),

ligamentous cervical spine, and full neck (Barker and Cronin, 2021). Yet, to date, there has been no implementation of the cervical spinal cord and surrounding neural tissues. Incorporating an anatomically correct spinal cord model into a full HBM like GHBMC M50 requires altering the brain tissue boundary conditions, which has the potential of affecting the resulting brain tissue deformations during simulated impact conditions.

2.4.1 Head Finite Element Models

Similar to the use of full-body HBMs, many head-only FE models have been developed to investigate brain tissue deformation during impact and risk of traumatic brain injuries (TBI). Current state-of-the-art head-only FE models have been developed by Wayne State University (Zhang et al., 2001), GHBMC head model (Mao et al., 2013), YEAHM (Fernandes et al., 2018), UCD Brain Trauma Model (Horgan and Gilchrist, 2003), Wake Forest (Miller et al., 2016), Simulated Injury Monitor (SIMon) head model (Takhounts et al., 2003; 2008), Kungliga Tekniska Högskolan (KTH) head model (Kleiven and Hardy, 2002; Kleiven, 2007; Zhou et al., 2020), the Human Head Model (Antona-Makoshi, 2016) and the Strasbourg University Finite Element Head Model (SUFEHM) (Deck and Willinger, 2008). In the first version of the KTH head model (Kleiven and Hardy, 2002; Kleiven, 2007) the extension of the spinal cord, without the nerve roots, was included. However, the most recent version of the KTH Head Model did not report specifics of the spinal cord implementation (Zhou et al., 2020). In another study, the Human Head Model (Antona-Makoshi, 2016) included a simplified cervical spinal cord in the spinal canal that utilized linear models for the meninges and linear viscoelastic model for the brain tissue. Most of the current FE head models utilize linear viscoelastic material behaviour to represent the mechanical properties of the brain tissue (Table 2.8). However, there is little cadaveric experimental data that FE head models can be validated against. Measuring the full displacement field of the cadaveric human brain is challenging (Hardy et al., 2007), with most studies instead reporting displacement of discrete points (Hardy et al., 2007; Mao et al., 2013). Several FE head models have been developed to represent various animal species for comparison to experiments (Anderson, 2004; Mao et al., 2006; Antona-Makoshi et al., 2014, 2015, 2016). Although some models included a spinal cord

35

(Antona-Makoshi et al., 2014, 2015, 2016), current limitations include non-human geometry and simplified material properties.

Table 2.8: Summary of the contemporary FE head models.

Model	Validation	Number of Elements	Number Brain Regions	Brain Constitutive Model	Reference
Wayne State University brain injury model (WSUBIM)	brain motion; intercranial pressure	314,500	4	Linear viscoelastic	Zhang et al., 2001
UCB Brain Trauma Model	intercranial pressure	28,000	1	Linear viscoelastic	Horgan and Gilchrist, 2003
Wake Forest	brain motion	2M nodes and elements	1	Linear viscoelastic	Miller et al., 2016
YEAHM	intercranial pressure	N/A	1	2nd order Ogden with viscoelasticity	Fernandes et al., 2018
aHEAD	brain motion	~1M	4	2nd order Ogden with viscoelasticity	Wilhelm et al., 2020
SIMon	relative brain motion intracranial pressure	45875	3	Linear viscoelastic	Takhounts et al., 2003; 2008
KTH Head Model	relative brain motion intercranial pressure	4.2M solid and 0.5M shell elements	8	Hyperviscoelastic	Kleiven and Hardy, 2002; Kleiven, 2007; Zhou et al., 2020.
Human Head-Neck Model	impact situations	291.948 solid elements and 53.609 shell elements	4	Linear viscoelastic	Antona-Makoshi, 2016
The Strasbourg University Finite Element Head Model (SUFEHM)	impact simulations	13.208	1	Linear viscoelastic	Deck and Willinger, 2008

FE head models are used in many studies to evaluate the risk of concussion and probability of TBI (Bruneau, 2019). The main benefit of using a FE head model is computational time efficiency compared to using a full HBM. A potential limitation of head-only FE models in predicting accurate brain tissue deformations during impact is the lack of a connecting spinal cord, which necessitates terminal boundary conditions at the end of the brain stem. This consideration of the brain stem boundary conditions with and without a spinal cord has not

been previous examined relative to brain tissue deformations and TBI risk during simulated impact conditions.

2.4.2 Brain Deformation Metrics in Human Body Model

A key benefit of developing FE HBM and head models is the ability to investigate injury risk at the tissue level under different loading conditions (Cronin, 2011; Schmitt et al., 2019). Researchers have developed several localized (element) metrics that have been shown to predict TBI more effectively than the gross kinematics of the head (Zhang et al., 2004; Giordano and Kleiven, 2014; Hernandez et al., 2015; Zhao et al., 2017). An important aspect that applies to the tissue level injury metrics is the dependence on the numerical threshold value connected to the specific FE model. For example, the threshold value of the MPS varies between 0.06 to 0.448 in the literature data for what.

The most common metric correlating TBI in FE models is a maximum principal strain (MPS), or the 95th percentile MPS (Post et al., 2013). The MPS metric was linked to observed concussion, and it was speculated that the MPS is a fidelic metric to represent the stretching of the axons (Ommaya and Gennarelli, 1974). However, the maximum 95th percentile MPS is a single value metric, insensitive to the respective element volume, nor does it consider strain distribution in the first 95% of the elements (Fahlstedt et al., 2022).

Cumulative strain damage measure (CSDM) is another metric frequently used to correlate FE model outputs to TBI risk (Giudice et al., 2019). CSDM indicates the brain tissue percentage (volume) exceeding a specific strain threshold value. The disadvantage of CSDM is extreme sensitivity to the chosen threshold value. Researchers have also used other metrics to predict neural tissue sequelae, such as strain rate, strain density energy, von-Mises stress, or maximum axonal strain. However, those metrics have not been used as frequently as MPS or CSDM (Bruneau, 2019). Ultimately, there is not yet consensus on the appropriate metric or threshold value for TBI or concussion (Kleiven, 2007; Giordano and Kleiven, 2014; Fahlstedt et al., 2021).

Chapter 3

Material Model Fitting and Validation for Spinal Cord-Pia Mater Complex

This chapter is an adapted version of the manuscript published in Frontiers in Bioengineering and Biotechnology: Biomechanics as 'Rycman, A., McLachlin, S., and Cronin, D. S. (2021). A Hyper-Viscoelastic Continuum-Level Finite Element Model of the Spinal Cord Assessed for Transverse Indentation and Impact Loading.' Reuse permitted under Creative Commons Attribution License (CC BY).

3.1 Introduction

Computational FE models can help to identify the salient mechanical properties that drive soft tissue behaviour in response to loading, to examine potentially injurious loading scenarios (Schmitt et al., 2019). In the context of SCI, the primary challenge with FE modelling lies in biofidelity, the ability of the model to accurately reproduce the behaviour of the simulated tissues (Cronin, 2011; Yang, 2017). Previous research has established that material properties and model validation are most important to the biofidelity of a FE model to predict mechanical response of the spinal cord tissue (Jones and Clarke, 2018). This is challenging due to the complexity of the spinal cord, consisting of multiple neural tissues, including the spinal cord parenchyma (white and gray matter), pia-arachnoid mater complex, and other connective tissues (Standring and Gray, 2009). Further, modeling spinal cord tissues in FE models is difficult due to the non-linear behaviour of the connected tissues, which includes hyperelastic and viscoelastic tissue response under deformation (Bilston, 2011).

The overarching objective of the current chapter was to develop non-linear material models applicable to a continuum-level spinal cord model that will be integrated into a contemporary HBM. As a first step, tissue-level experimental data (Jin et al., 2006; Jannesar et al., 2018) was utilized to fit parameters of the non-linear constitutive models. Validation of fitted material models was performed by recreating ex-vivo transverse indentation of the porcine Spinal Cord-Pia mater (SCP) complex (Fradet et al., 2016) and ex-vivo transverse impact test on the bovine SCP complex (Persson, 2009; Persson et al., 2009). The validation process was independent

of the fitting process; the values of the material parameters obtained in the fitting process were not altered in the indentation or impact model. Lastly, the role of the pia mater and its thickness during the dynamic impact of the SCP complex was examined.

3.2 Material and Methods

3.2.1 Spinal Cord and Pia Mater Material Models

The spinal cord material response was determined from experimental data of unconfined compression of non-human primate spinal white mater (Jannesar et al., 2018) and used to fit isotropic hyperelastic material coefficients using an Ogden constitutive model (Ogden, 1972). Viscoelastic effects were incorporated using a quasi-linear viscoelastic formulation (Fung, 1981; Xu et al., 2008) with normalized Prony series shear moduli (G_i) and relaxation times (β_i). The explicit FE software utilized a modified strain energy density Ogden function (Hallquist, 2006) for the deviatoric and hydrostatic components of deformation (Equation 3.1). The coefficients μ_i and α_i are i^{th} Ogden model material constants, λ^* are the deviatoric principal stretches, K is the bulk modulus and J is the relative volume.

$$W(\lambda_1, \lambda_2, \lambda_3) = \sum_{i=1}^{N} \frac{\mu_i}{\alpha_i} (\lambda_1^{*\alpha_i} + \lambda_2^{*\alpha_i} + \lambda_3^{*\alpha_i} - 3) + \frac{1}{2} K(J-1)^2$$

Equation 3.1: Modified Ogden strain energy density function including the hydrostatic component.

Stress in the quasi-linear viscoelastic formulation was represented in the form of the Boltzmann hereditary integral including the relaxation modulus (G) and strain rate ($\dot{\varepsilon}$) (Equation 3.2).

$$\sigma(t) = \int_0^t G(t - \tau, \varepsilon) \dot{\varepsilon}(t) d\tau$$

Equation 3.2: Quasi-linear viscoelastic constitutive model.

In quasi-linear viscoelasticity, the relaxation function can be separated into strain-dependant and time-depended parts (Xu et al., 2008) (Equation 3.3). The strain-dependant part ($\sigma^E (\varepsilon)$) is

derived from the Ogden strain energy density function (Equation 3.1); whereas the time-dependant part is formulated as a sum of the Prony series exponential relaxation functions (Equation 3.4).

$$G(t, \varepsilon) = g(t)\sigma^E(\varepsilon)$$

Equation 3.3: Separation of the relaxation function to time-dependent and stress-dependent components.

$$g(t) = \sum_{i=1}^{n} G_i e^{-\beta_i t}$$

Equation 3.4: The time-dependent part of the viscoelastic relaxation function formulated with the Prony series.

Finally, substituting Equation 3.3 and 3.4 to Equation 3.2, the stress in the quasi-linear viscoelastic material can be expressed in the form:

$$\sigma(t) = \int_0^t \sum_{i=1}^{n} G_i e^{-\beta_i(t-\tau)} \left[\frac{\partial \sigma^E}{\partial \varepsilon} \frac{\partial \varepsilon}{\partial \tau} \right] d\tau$$

Equation 3.5: Quasi-linear viscoelastic model total stress as a function of time and deformation.

The hyperelastic and viscoelastic coefficients were determined using commercial optimization software (LS-OPT v6.0.0, LST, Livermore, CA,). Single element test cases were simulated at each experimental strain rate (i.e., 0.32 s^{-1}, 2.83 s^{-1}, 25.47 s^{-1}, and 77.22 s^{-1}) and the material parameters were determined using the curve mapping optimization method (LS-OPT Manual, LST, Livermore, CA). The lowest strain rate data (0.32 s^{-1}) was treated as quasi-static and used to fit the hyperelastic function. Three sets of viscoelastic constants (G_i and β_i), with β_i values corresponding to the strain rates were used as initial guesses for the fitting algorithm. The normalized shear coefficient (G_i) values were constrained such that their sum was less than unity, and initial guesses were set to 0.25 with a maximum value of 1.0. The optimization algorithm compared the uniaxial compression response of the single element for each strain rate and the range of strains reported in the experiments (Jannesar et al., 2018). The results of each model were combined using a multi-objective function that gave the results from each strain rate an equal weighting and sought to minimize the difference between the areas under experimental stress-strain curves with the calculated single element response. Specifically, a

robust curve mapping algorithm (LS-OPT Manual, LST, Livermore, CA) was used to compare the predicted and experimental responses. Convergence was achieved when the difference between the curves was less than 0.5%.

The pia mater mechanical response under deformation exhibits a typical response for collagen-rich tissue with distinct toe, linear, traumatic, and post-failure regions. Tissue-level tensile experimental test data (Jin et al., 2006) was utilized to fit the hyperelastic coefficients of the Ogden model for the pia mater. Quasi-static (0.05 s^{-1}) experimental stress-strain curves were used to fit a single term Ogden model. Model coefficients were found using GNU Microsoft Excel solver (Microsoft, Redmond, WA) with an optimization target to maximize the coefficient of determination. The fit was confirmed by comparing a single element verification model to the experimental data.

3.2.2 Transverse Indentation Test

The indentation validation case was simulated (Figure 3.1) by recreating ex-vivo experimental setup where porcine cervical SCP complex specimen was indented by a small cylinder (Fradet et al., 2016). A computational FE model was established to recreate the experimental setup, consisting of the porcine tissue specimen, 25 mm in length, a rigid posterior support, and a cylindrical indenter with a diameter of 5 mm (cross-sectional area of 19.6 mm^2). Anterior-posterior and lateral dimensions of the porcine spinal cord were adopted from experimental measurements of the cord cross-section (Fradet et al., 2016). The spinal cord and pia mater tissues were modelled using fully integrated hexahedral elements. Since the impactor was relatively small compared to the specimen dimensions, a smaller mesh was required for the spinal cord to accurately predict loading at the boundary between spinal cord and indenter. The indentation model was simulated using three mesh sizes: 0.8 mm, 0.6 mm, and 0.45 mm to establish convergence. The mesh sizes of 0.6 and 0.45 mm converged to a similar force value at 10%, 20%, 30% 40% and 50%, transverse compression. However, some contact instabilities, attributed to mesh locking on the indenter, were observed while using a mesh size of 0.8 mm and 0.6 mm; therefore, a mesh size of 0.45 mm was used for the simulations in this study. The static and dynamic friction coefficients between the pia mater and the metal impactor were

assumed to be 0.1, following a value proposed for brain tissue and metal (Rashid et al., 2012). To achieve stable contact between tissue and cylinder, a pre-load of 0.2 N was applied as in the experiment. Indentation simulations were performed for three strain rates: 0.5 s^{-1}, 5 s^{-1}, and 50 s^{-1}. The resulting force acting on the cylinder from deformation of the SCP complex was compared to experimental data (Fradet et al., 2016). The thickness of the pia mater was 0.13 mm, as previously reported for the porcine specimens (Kimpara et al., 2006).
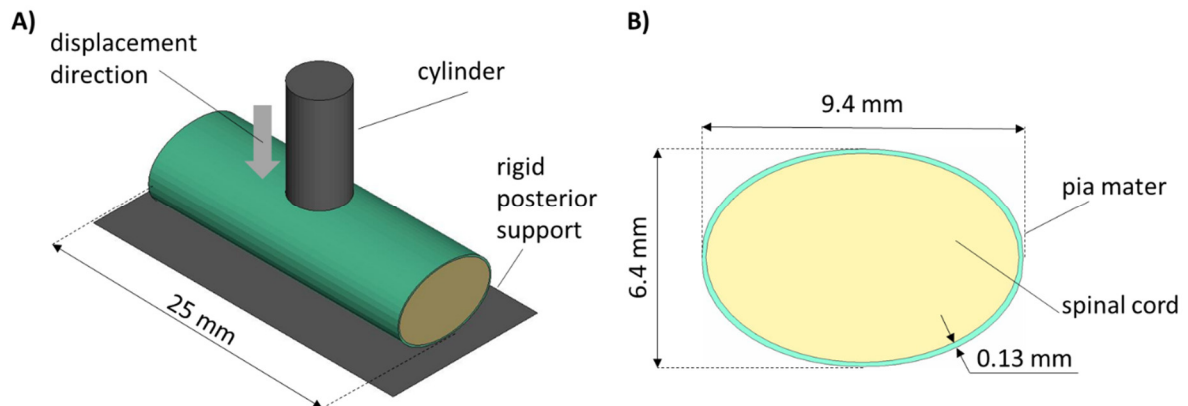
Figure 3.1: (A) Indentation test simulation setup, isometric view. (B) Transverse cross-sectional view of the spinal cord-pia mater complex with the dimensions used in the indentation simulations.

3.2.3 Transverse Impact on the Spinal Cord-Pia Mater Complex

Transverse impact on the SCP complex was simulated by replicating ex-vivo experimental tests on bovine spinal cord-pia mater specimens. The test specimens were 140 mm long and were subjected to 8% engineering strain preload along the length, followed by a dynamic relaxation period of 60 seconds. Next, a pellet was accelerated with a pneumatic actuator and impacted the mid-span of the bovine specimen that was resting on a supporting surface. In total, three pellet impacts were conducted at the reported velocity of 4.5 m/s. The trajectories of the pellets (displacement versus time) were reported at 4500 Hz (Persson, 2009; Persson et al., 2009). A three-dimensional FE model (Figure 3.2A), which included the cervical nervous tissues (the spinal cord and pia mater), the rigid parts of the support wall, and the three impactors (pellets), was designed based on previously published experimental and computational literature data (Persson et al., 2011). The model did not include spinal nerves as

they were trimmed in the experiment. A commercial meshing software (HyperMesh, Altair Engineering, Troy, MI) was used to generate the FE mesh. The spinal cord and pia mater were represented by 37,100 and 9,100 fully integrated hexahedral elements, respectively, with an average element size of 0.8 mm. Mesh convergence was conducted by a simulating model with three average mesh sizes 0.8 mm, 0.4 mm, and 0.2 mm. The maximum deformations of the SCP complex were used with Richardson extrapolation (Roache, 1998) to estimate the 0 mm element solution. It was found that all three mesh sizes were located in the asymptotic convergence region and the percent difference between meshes was less than 1.5%; therefore, an average element size of 0.8 mm was identified as sufficient to model the dynamic behaviour of the SCP complex. In the experiments, the three pellets had the same mass (7g) but different impact areas: 314 mm^2 (Pellet I), 157 mm^2 (Pellet II), and 78,5 mm^2 (Pellet III) (Figure 3.2C). For the same impact velocity, decreasing the impact area of the pellets creates a more aggressive insult to the SCP complex and provides a range of validation data that achieve varying levels of strain and strain rate within the tissues.
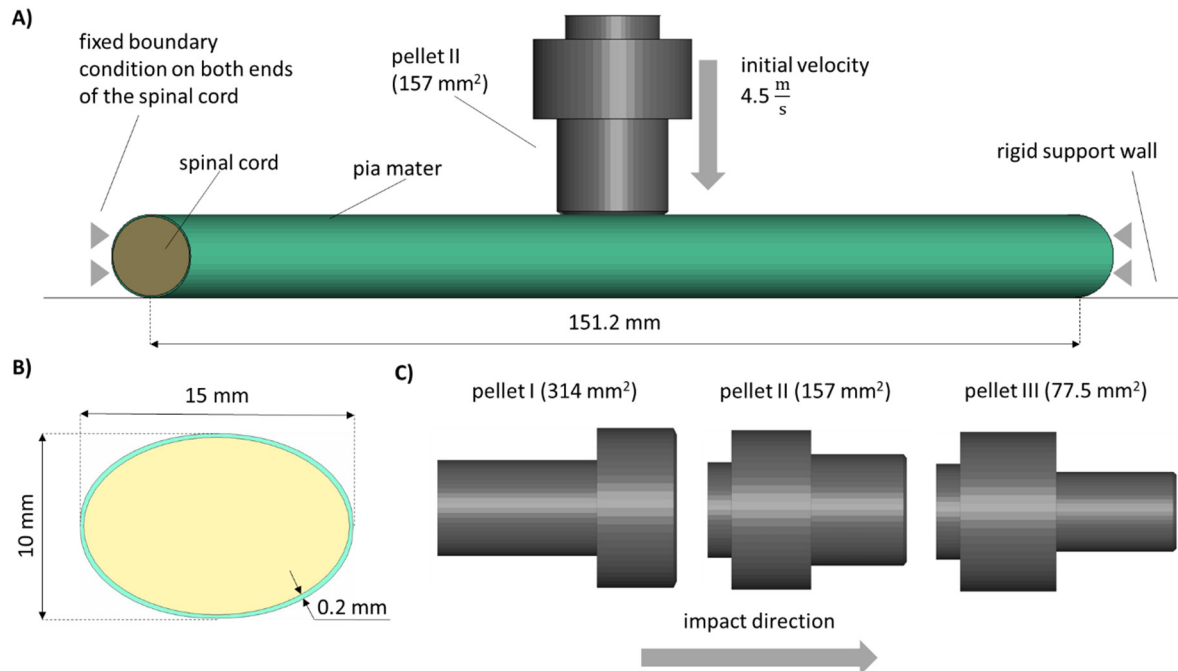
Figure 3.2: (A) Impact test simulation setup with the Pellet II case. (B) Sagittal view of the spinal cord-pia mater complex dimensions used in the impact simulations. (C) Numerical representations of the three pellets.

43

The static and dynamic friction coefficient between the pia mater and the impactor was 0.1 (Rashid et al., 2012). A velocity sensitivity study was conducted using the maximum, minimum, and average velocities for each pellet. The pellet velocities were calculated based on the initial slope of the experimental pellet trajectory curves to quantify the experimental variability in the context of the reported typical 4.5 m/s pellet velocity (Figure 3.10). Finally, a thickness sensitivity study was conducted for the pia mater to evaluate the overall effect of the pia mater thickness (0, 0.13, 0.20 and 0.27 mm) on the spinal cord complex compression during impact (Kimpara et al., 2006; Ramo et al., 2018). The proposed pia mater constitutive model for the current study was compared to a widely used linear elastic model (E = 39.3 MPa) (Kimpara et al., 2006). The pia mater thickness and material variations were assessed using the maximum principal strain induced in a volume of the pia mater in the impact zone. The volume considered comprised the diameter of the pellet plus one diameter of the spinal cord on either side of the pellet (Figure 3.13), which was the highly deformed length of the spinal cord.

3.2.4 Software and Dana Analysis

A commercial meshing software (HyperMesh, Altair Engineering, Troy, MI) was used to generate the geometry and FE mesh for the spinal cord parenchyma and pia mater for both models. Material coefficients for the hyper-viscoelastic model for the spinal cord parenchyma were obtained using commercial optimization software (LS-OPT v6.0.0, LST, Livermore, CA,) with an embedded version of a commercial explicit FE solver (LS-DYNA R9.3.1 double-precision). Hyperelastic parameters for the pia mater material model were fitted using GNU Microsoft Excel solver (Microsoft, Redmond, WA). Transverse indentation and impact models were solved using with a commercial explicit FE software (LS-DYNA version R9.3.1 MPP, double-precision, LST, Livermore, CA, on Intel Xeon E5-2683 2.1 GHz processors). The simulation results that included the displacement of the pellet, the internal energy of the individual tissues, the strain rate history of the spinal cord elements, and contact force between the cylinder and tissue were analyzed using a commercial post-processing software (LS-PrePost version 4.7.9). Fit of the material models were quantified using the coefficient of

determination (R^2), defined as the proportion of variance of the model to the experimental data (Equation 3.6).

$$R^2 = 1 - \frac{RSS}{TSS} \ where: RSS = \sum_{i=1}^{N}\left(y_{exp,i} - y_{model,i}\right)^2 ; TSS = \sum_{i=1}^{N}\left(y_{exp,i} - y_{exp,mean}\right)^2$$

Equation 3.6: Definition of the coefficient of determination (R^2).

In addition, the root-square-mean error (RSME) was calculated for the fitted spinal cord tissue and pia mater material models. Experimental trajectories of the pellets were digitized (Engauge Digitizer v10.6) from the published experimental data (Persson, 2009). To obtain the average trajectory for each pellet, a previously published methodology was adopted (Mattucci and Cronin, 2015). Experimental trajectories of pellets were divided into three regions based on the SCP complex state: 1 - loading, 2 - rebound, 3 - unloading (Figure 3.3). Loading and unloading regions were fitted with a linear polynomial, whereas a 3rd order polynomial was used to approximate the rebound phase. The average response was determined by calculating pointwise average. Additionally, results of the impact model were compared to the average experimental curve using CORrelation and Analysis method (CORA) (Gehre et al., 2009) (Figure 3.3), with equally weighted size and shape ratings of 0.5. The size rating compares the area under the curves, while the shape rating compares the trend in slopes between the curves.
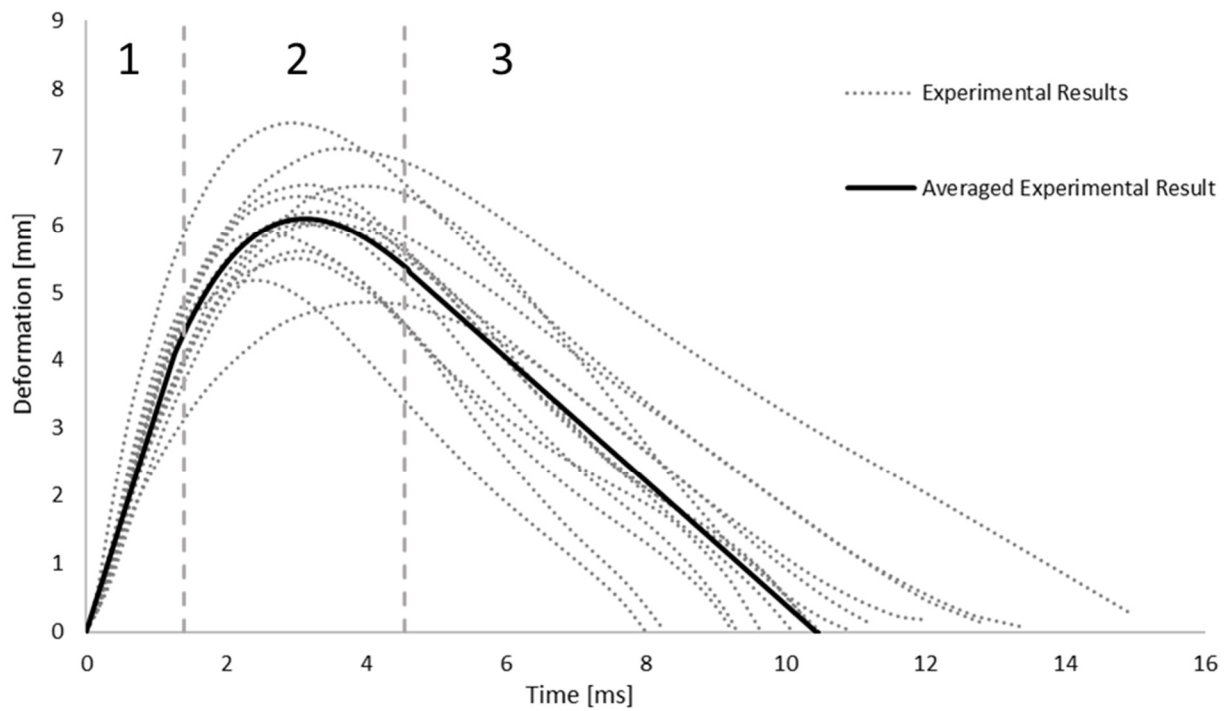
Figure 3.3: Experimental trajectories including the average response for all impacts of Pellet I on the spinal Cord-pia mater complex divided into three regions: 1) loading, 2) rebound, and 3) unloading (Persson 2009).

3.3 Results

3.3.1 Spinal Cord and Pia Mater Material Models

A one-term Ogden model with quasilinear viscoelasticity (Table 3.1) provided an excellent fit to all four stress-strain experimental curves: 0.32 s^{-1}, 2.83 s^{-1}, 25.44 s^{-1}, and 77.22 s^{-1}. Single element simulations verified the curve fit (Figure 3.4). The coefficient of determination (R^2) ranged from 0.976 to 0.994, with an average RSME of 1.01 kPa.
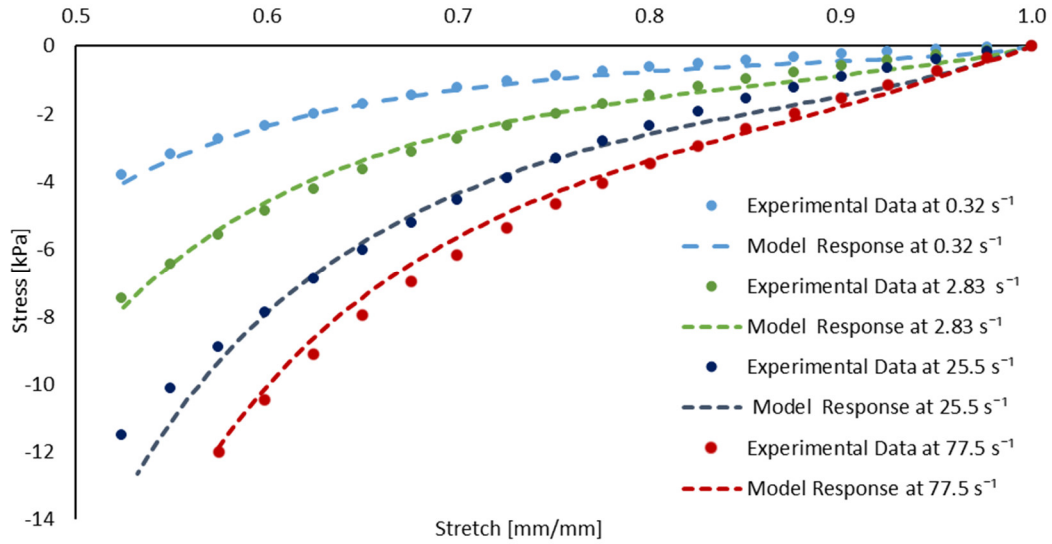
Figure 3.4: Optimized response of the hyper-viscoelastic Ogden material model in single element test cases compared to unconfined compression test data of the spinal cord tissue (Jannesar et al., 2018).

The one-term hyperelastic Ogden representation of the tensile mechanical response of the pia mater was fitted to the average experimental curve (Table 1). The model response fell within the scatter of the experimental data (Figure 3.5). The RSME for this fit was 29.38 kPa.
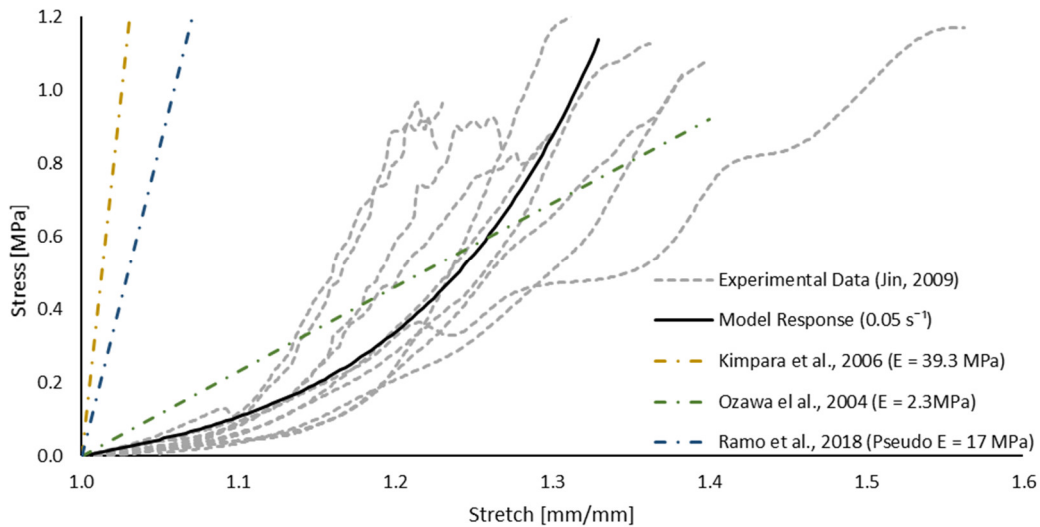
Figure 3.5: Optimized response of the hyperelastic Ogden material model in a single element test case compared to tensile test data of the pia mater (Jin et al., 2006). Other strain- stress curves with different Young's modulus reported in studies were presented.

Table 3.1: Summary of the material properties of the spinal cord and pia mater.

Material	Constitutive Model	Model Parameters and Coefficients				References
Spinal Cord	Hyperelastic (Ogden model) with quasi-linear viscoelasticity	$\mu = 209$ Pa $\nu = 0.499$	$\alpha = 7.52$	$G_1 = 0.033$ $G_2 = 0.296$ $G_3 = 0.406$	$\beta_1 = 2$ s^{-1} $\beta_2 = 13$ s^{-1} $\beta_3 = 406$ s^{-1}	Jannesar et al., 2018
Pia mater	Hyperelastic (Ogden model)	$\mu = 42$ kPa	$\alpha = 12.58$	$\nu = 0.49$		Jin et al., 2006

3.3.2 Indentation Test Simulation

The SCP complex was evaluated in the transverse indentation test for three experimental strain rates: 0.5 s^{-1}, 5 s^{-1}, and 50 s^{-1}. The force acting on the cylinder versus transverse compression of the specimen was compared to reported experimental curves. Simulation results were within one standard deviation for all three strain rates up to 60% of transverse compression of the SCP complex (Figure 3.6).
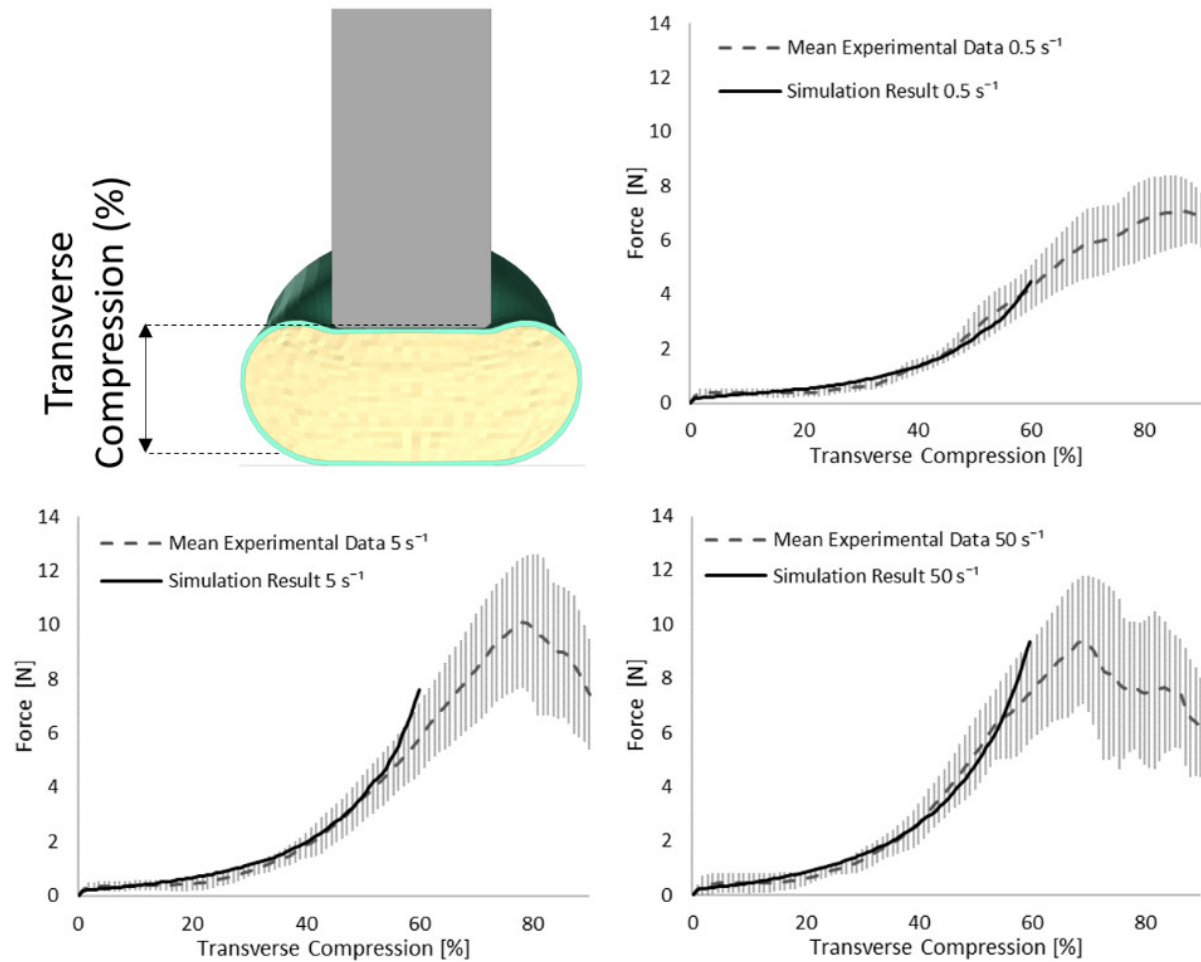
Figure 3.6: Stress-transverse compression plots for the indentation simulations for three experimental strain rates 0.5 s^{-1}, 5 s^{-1}, and 50 s^{-1}; error bars represent standard deviation of the experimental data (Fradet et al., 2016).

3.3.3 Impact Test Simulation

The SCP complex FE model was evaluated using experimentally reported data for three transverse pellet impacts on bovine SCP specimens (Persson, 2009; Persson et al., 2009). The model accurately predicted kinematics of the pellets in the loading phase up to the maximum deformation of the SCP complex (Figure 3.7). The percentage difference between reported maximum deformation (Persson et al., 2009) and the computed values was 6.63% for Pellet I, 4.00% for Pellet II and 10.17% for Pellet III.
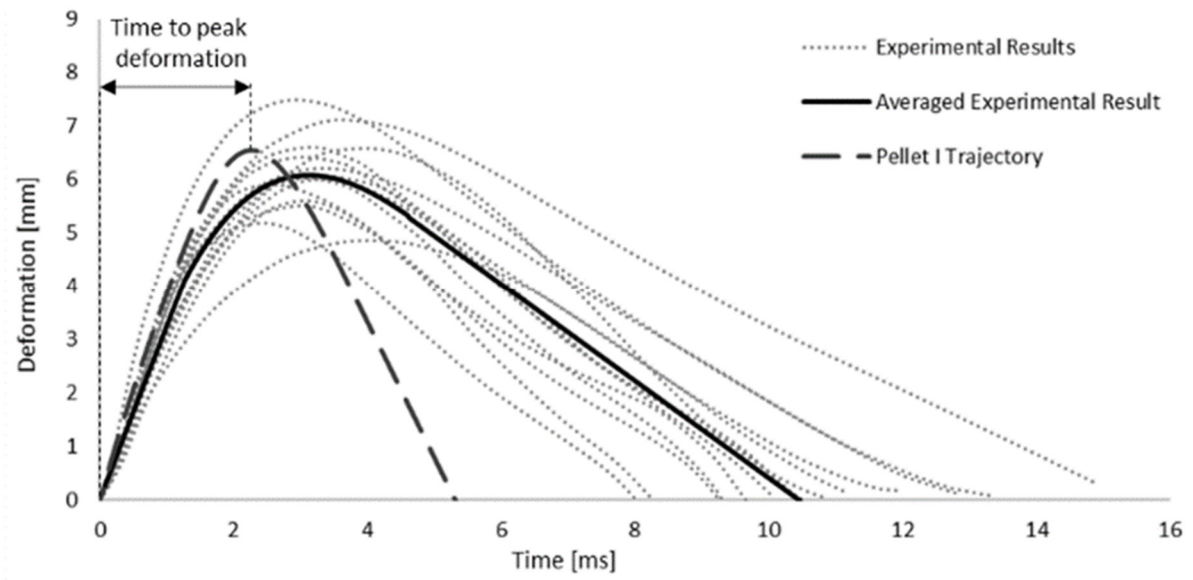
Figure 3.7: Kinematic response of Pellet I compared to the experimental data (Persson 2009).

The maximum deformation of the SCP complex for all three pellets fell within the reported range of the experimental data. The maximum deformation for Pellet I and Pellet II was slightly above the experimental average, whereas the maximum deformation of the Pellet III was just above the lower bound of the reported experimental data (Figure 3.8).
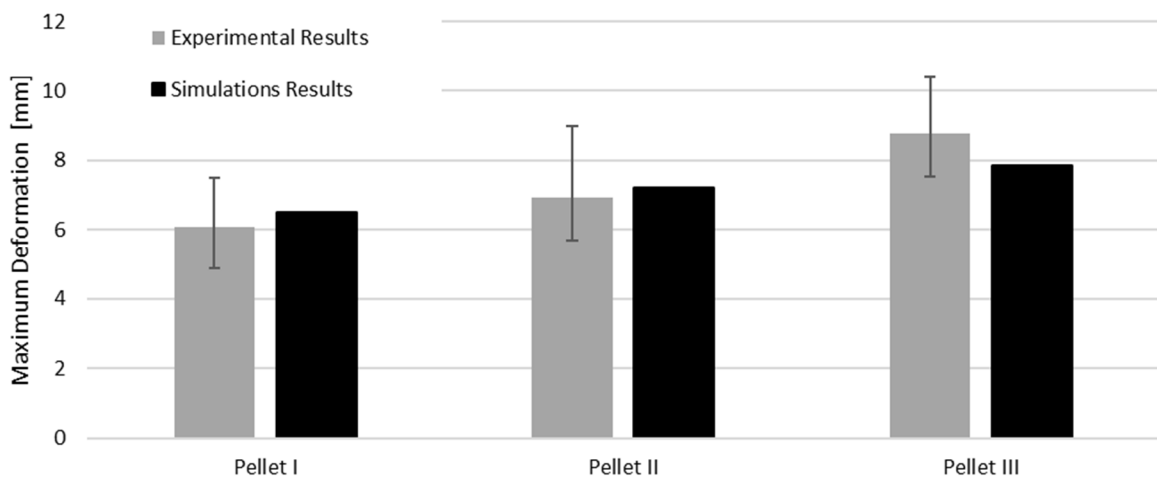
Figure 3.8: Comparison of the maximum deformation of the SCP complex for three impacts with experimental data.

The kinematics of the pellet during the unload phase happened faster than the experimental data suggested (Figure 3.7; Figure 3.9). Results of the impact model were compared to the average experimental curve using CORA. The CORA rating ranged from 0.747 to 0.858, with an average of 0.815. Varying the thickness of the pia mater revealed that the maximum compression of the SCP complex was within 1% across the range of four different values tested (Figure 3.12). Simplifying the pia mater to linear elastic material properties resulted in maximum deformation below the experimental range. On average the maximum deformation of the SCP complex with elastic pia mater was lower by 38.5% compared to the experimental mean value (Figure 3.12).
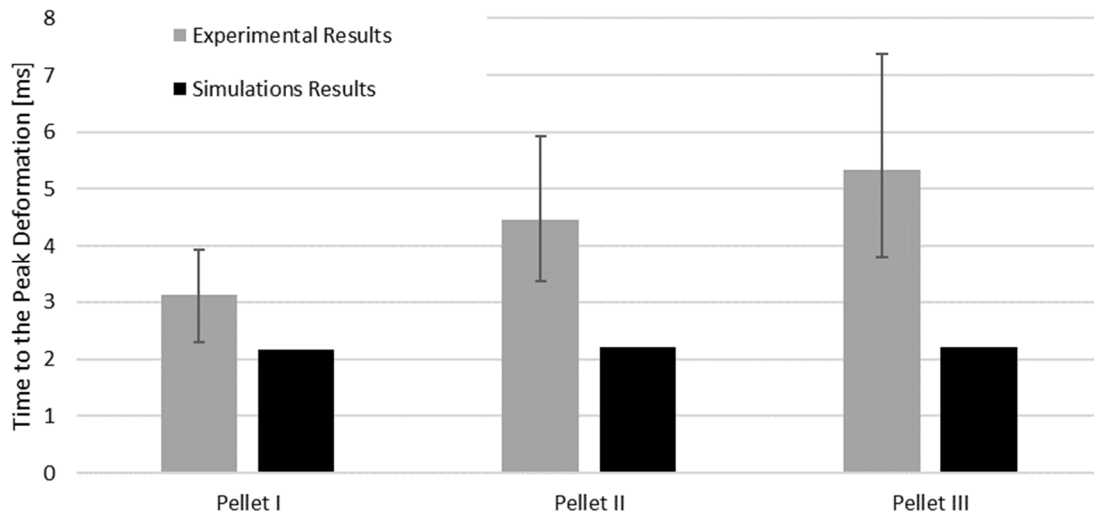
Figure 3.9: Comparison of the time to the peak deformation for three impacts with experimental data.

3.4 Discussion

3.4.1 Material Properties of the Spinal Cord-Pia Mater Complex

The SCP complex constitutive models were based on measured primate tissue material properties for the spinal cord parenchyma and bovine tissue for the pia mater. The neural system of the non-human primate and human were found to be very similar (Jannesar et al., 2018). Thus, the obtained constitutive models can be taken as a reasonable representation of the expected human neural tissue response under dynamic loading. In experimental studies,

other mammalian tissues may be used due to availability and convenience in testing. Several studies have reported similarities between bovine and human spinal cord mechanical properties (Bilston & Thibault, 1995; Oakland et al., 2006). In other studies, porcine tissues were used and have been suggested to be a reasonable surrogate for human tissues (Sparrey and Keaveny, 2011; Shetye et al., 2014; Kim et al., 2018).

The constitutive model parameters identified in this study were not calibrated or altered to improve the expected results of the validation cases. Adjusting or calibrating constitutive model parameters to one specific loading scenario can lead to unphysical response in other types or modes of loading (Cronin, 2011; Yang, 2017). Further, calibration to specific cases can result in material properties outside of the physical bounds for a given material and can lead to changes in FE model behaviour (e.g., contact stiffness, mechanical wave speed propagation). The validation process performed in this study used independent sets of tissue data for fitting material parameters and two independent transverse deformation cases to assess the resulting properties. Applying proposed material parameters (Jannesar et al. 2018) for a 1st order Ogden quasi-linear viscoelastic model for the spinal cord resulted in significantly lower deformations in the impact model on average by 27% compared to average experimental results, attributed to material constants that differed by as much as one order of magnitude, compared to the values in the present study.

3.4.2 Transverse Indentation of the Spinal Cord-Pia Mater Complex

A comparison of the force acting on the cylinder during the indentation experiment showed an excellent match with the average force-compression curves for all experimental strain rates, up to 60% transverse compression of the SCP complex. Above the 60% transverse compression, the simulation results diverged from the experimental results, showing a higher overall stiffness. Local or element-level strains that occur in the spinal cord at such high transverse compression values exceed the range of strains for which the constitutive model was fitted. Fradet et al. (2016) reported failure of the specimen, tearing of the pia mater and expulsion of the white matter. Damage and failure of the material were not incorporated into the fitted constitutive models but should be considered for future models. The mesh sensitivity

study revealed that, due to the small size of the indenter (5 mm diameter), accurate representation of the spinal cord deformation required an average spinal cord size mesh of 0.45 mm. However, other studies simulating bone fragments representative for burst fracture have suggested impactor sizes with a diameter of 20 mm (Hall et al., 2006; Jones et al., 2008), which could be modeled with the large mesh sizes proposed in this study.

3.4.3 Transverse Pellet Impact of the Spinal Cord-Pia Mater Complex

Results from the impact test simulations were within the experimental variability up to the maximum deformation. On average, the percent difference in maximum deformation between the model and experiments was 7% for all three pellets, but the unloading phase of the FE model was shorter than the experimental unloading phase on average by 60% (5.2ms) (Figure 3.7, Figure 3.9). Moreover, the velocity sensitivity study addresses, in part, the observed variability in the measured spinal cord deformation reported in the experimental data (Figure 3.10).

	Simulation Velocity [m/s]		
Case	Min	Average	Max
Pellet I	2.63	3.23	4.97
Pellet II	2.25	2.92	4.59
Pellet III	2.84	3.49	5.09
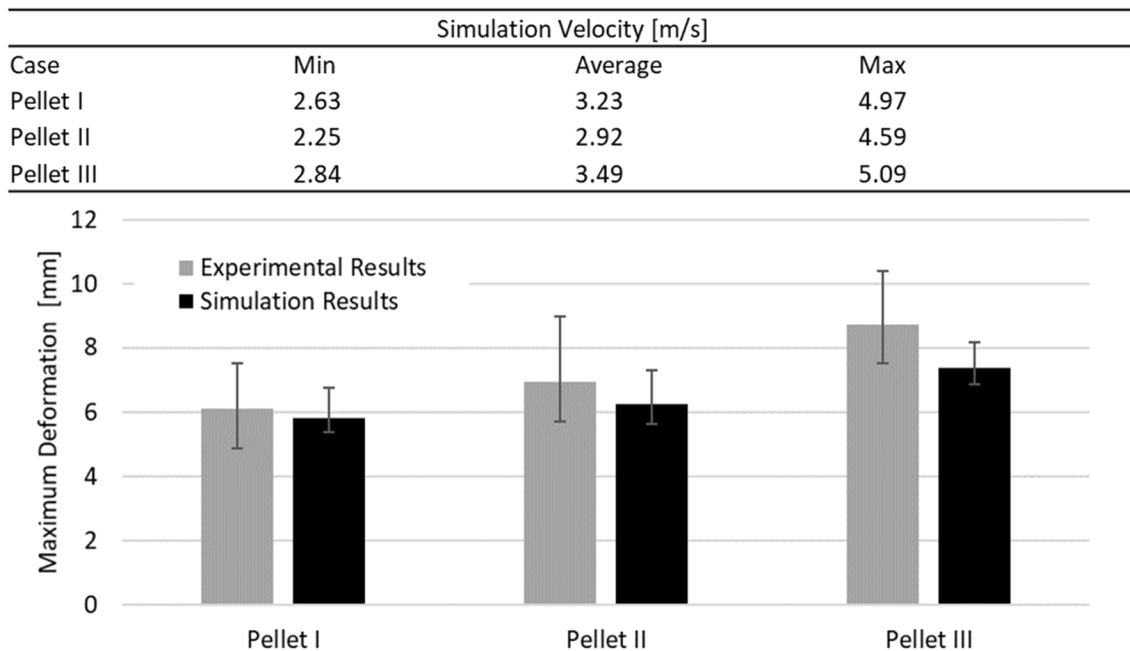
Figure 3.10: Spinal cord impact model velocity sensitivity study. Values of minimum, maximum and average velocities were calculated from based on initial slope of the experimental data (pellet trajectories).

53

Nervous tissues are composed of 75 to 77% fluid (Keep et al., 2012; LoPachin et al., 1991). Arguably, during dynamic transverse impact on the SCP complex, highly deformable materials can flow and move out of the impact zone. Inherently a Lagrangian mesh formulation introduces challenges in predicting flow of material. This represents one potential possibility as to why there was a large difference in the unloading phase of the FE model compared to the experimental data. Furthermore, the reported range of strain rates of the tissue-level experimental data of the spinal white matter did not correspond fully to the range of strain rates that was observed during pellet impacts. The maximum mean strain rate that was observed in the spinal cord was measured as a fraction of the volume of the spinal cord (Figure 3.11). On average, 20.9% (Pellet I - 27.4 %; Pellet - II 21.4%, Pellet III - 14.0 %) of the volume of the spinal cord experienced a strain rate above the maximum strain rate (77.22 s^{-1}) reported in the tissue-level experiment (Jannesar et al., 2018).
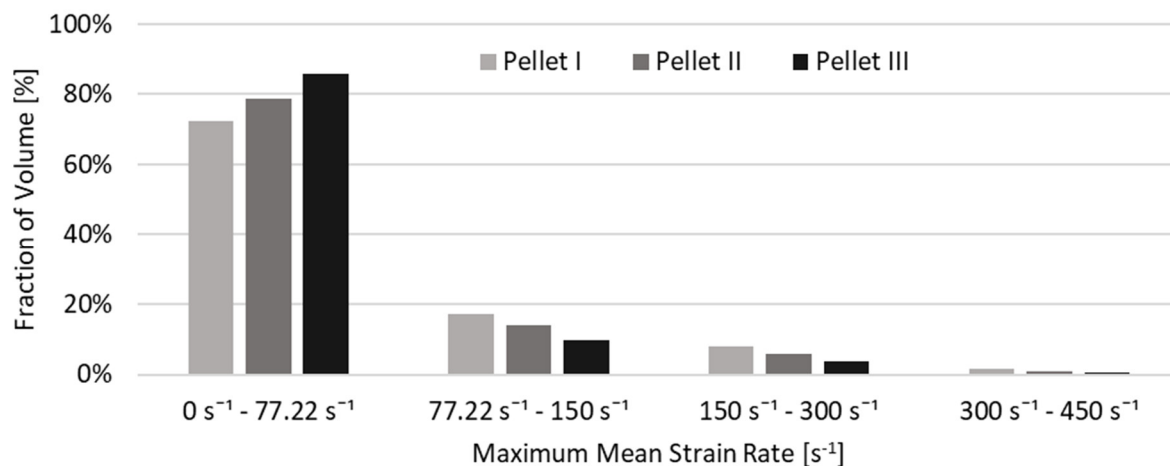
Figure 3.11: Volume fraction of the spinal cord that was subjected to maximum mean strain rate.

Although the quasi-linear viscoelastic model formulation extrapolates stresses beyond those for which the model was calibrated, it is not clear whether extrapolated stresses are represented faithfully. In summary, it is unknown if the model underestimates or overestimates the extrapolated stresses for strain rates exceeding 77.22 s^{-1}. Lastly, Fradet et al. (2016) reported

that for the highest transverse compression rate (50 s^{-1}) of the SCP complex, damage occurred at compression of 66.9% and for some cases tearing of the pia mater and expulsion of the white matter occurred. Further, some studies have demonstrated that damage of soft tissues is progressive and depends on the applied strain rate (Mattucci et al., 2013). In the impact test simulations, strain rates higher than 50 s^{-1} and similar values of transverse compression (63% to 76%) were observed. These experimental results suggest that damage could occur in the spinal cord under aggressive impact conditions and future models should consider incorporating damage when sufficient experimental data is available. It can only be hypothesized that damage in the spinal cord tissues could have occurred in the physical test, while no visible tear or failure of the tissue was reported in the experiments (Persson, 2009). Lack of a material damage model could explain the difference between the experiment and FE model in the unloading phase for the pellet impacts (Figure 3.7).

3.4.4 Importance of the Pia Mater on Response of the Spinal Cord-Pia Mater Complex

Previously published studies indicated greater stiffness of the pia mater compared to the spinal cord (Ozawa et al., 2004; Ramo et al. 2018; Tunturi 1978). Further, the reinforcing properties of the pia mater and the influence on the SCP complex were previously acknowledged in the literature (Clarke et al., 2009; Galle et al., 2010). Ozawa et al. (2004) observed that pia mater restores a deformed spinal cord to the original shape after transverse compression and estimated that pia mater was around 460 times stiffer than the spinal cord (Ozawa et al., 2004), in agreement with the material data used in this study (Figures 3.4; Figure 3.5). Ramo et al. (2018) recognized that pia-arachnoid mater influenced the longitudinal mechanical response of the SCP complex, despite the relatively low thickness (0.2 mm) of this membrane-like tissue (Watson et al., 2009). Moreover, Ramo et al. (2018) reported that the pia-arachnoid complex comprises up to 5.5% of the transverse area of the SCP complex. In the proposed models in this study, the pia-arachnoid complex area was 7% in the indentation model and varied from 4.54 % (0.13 mm) to 9.53% (0.27 mm) for the impact model.

Comparison between the impact models with incorporated pia mater and without showed that the presence of the pia mater reduced the maximum compression of the SPC by 9% on average

55

(Figure 3.12). The sensitivity study confirmed that pia mater confining effects play a strong role in the spinal cord deformation rather than the pia mater thickness. Jin et al. (2006) reported damage of some pia mater specimens as low as 20% tensile strain (Figure 3.5), while Kimpara et al. (2004) reported failure of the pia mater under tensile strain in the strain range of 28% to 48%.
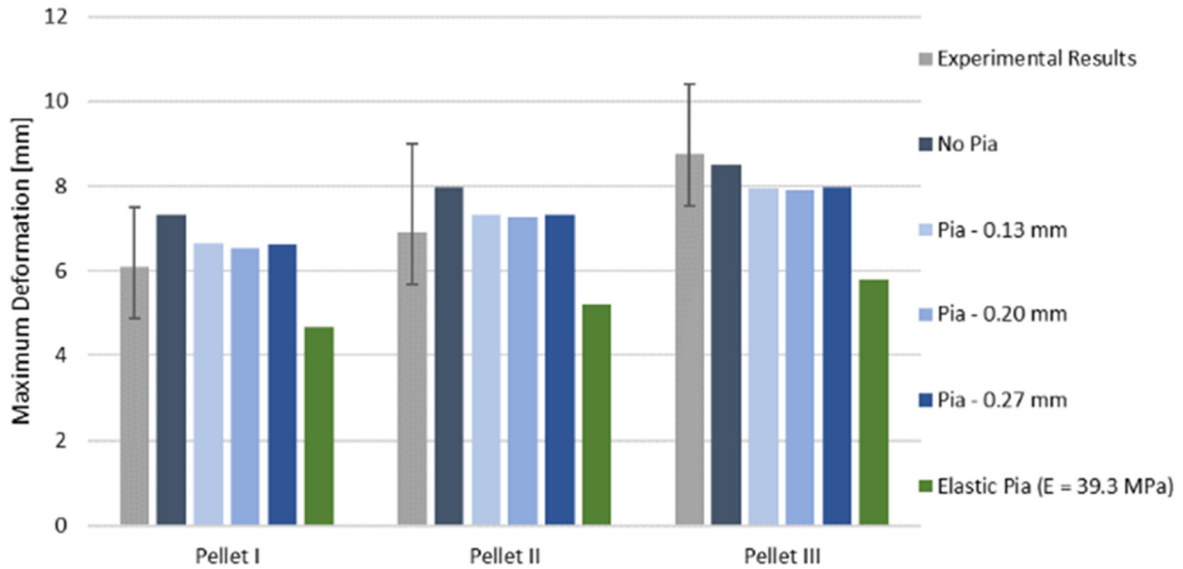
Figure 3.12: Variation of the peak deformation in the impact model for three pellets with respect to varying thickness of the pia mater.

In the vicinity of the impactor, the strains in the pia mater are in the reported failure range, which supports that tearing of the pia mater may have occurred in the impact experiments, resulting in the identified changes to the unloading phase. Further, this agrees with observations that pia mater significantly affects mechanical response of the SCP complex (Jannesar et al., 2016).
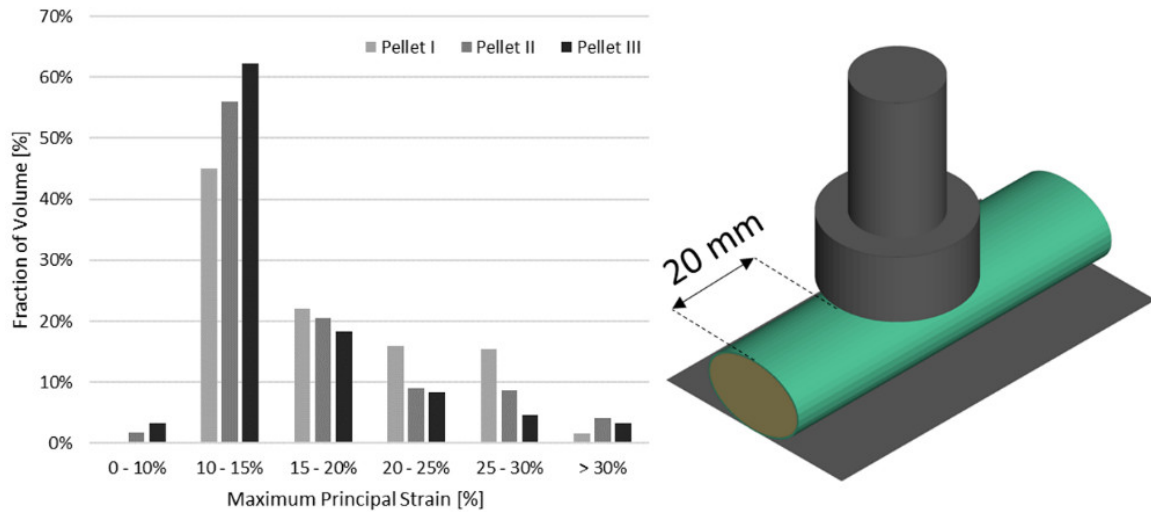
Figure 3.13: Volume fraction of the pia mater that was subjected to maximum principal strain in the impact model in the vicinity of the impact.

Several studies have been conducted to investigate a correlation between spinal cord transverse compression and neurological deficit. Anderson (1985) found that a compression of 50% of the spinal cord leads to neurological sequela. Moreover, Anderson (1985) reported that the deformation rate plays a role, in addition to compression magnitude in SCI severity. Sparrey et al. (2008) performed histological studies on rat spinal cord at two impact velocities (fast and slow), reporting that the velocity of the deformation has a significant effect on SCI and the related internal hemorrhage. Kearney et al. (1988) observed an absence of neuron transmission after 65% transverse compression of the spinal cord. FE simulation of the impacts of the pellets resulted in transverse compression of the spinal cord by 63%, 70%, and 76%, for Pellet I, Pellet II, and Pellet III, respectively. Penning et al. (1986) reported neurological sequela when the transverse cross-sectional area of the spinal cord was reduced by 30% or more. In the simulations from the current study, transverse cross-sectional areas of the spinal cord were reduced by 37%, 44%, and 46% for Pellet I, Pellet II, and Pellet III, respectively. Both injury thresholds (i.e., transverse compression of the spinal cord and reduction of the transverse area) indicate the potential for SCI if the deformations resulting from the pellets impact occurred within a living subject.

3.5 Conclusions

The presented FE model has several recognized limitations:

- The obtained hyper-viscoelastic material parameters for the spinal cord parenchyma provided excellent fit to the experimental data (R^2=0.98) and demonstrated good correspondence to independent experimental data through the validation cases. However, it is difficult to absolutely determine if the fitting method used identified the best global material model parameters.

- The model used a single representation of the transverse dimensions of the SCP complex, and a sensitivity study regarding the expected variation in spinal cord diameter and pia mater thickness was not investigated. In the simulated FE models, the thickness of the pia mater was in the reported range of 130 to 270µm (Kimpara et al., 2006).

- This study focused on examining the effects of material properties that drive the dynamic response of the SCP complex; however, variations in material properties were not investigated and should be considered in future studies. This may have contributed to differences between reported ex-vivo experimental data and simulations results.

- The material models used to represent spinal cord were isotropic.

- The spinal white matter was calibrated to the experimental data in the strain rate regime up to 77.22 s^{-1}. The volume fraction analysis revealed that, on average, 20.9% of the spinal cord volume exceeded a strain rate of 77.22 s^{-1}. Additional experimental testing at higher strain rates is needed to assess this limitation.

- The mechanical properties of the pia mater were obtained from quasi-static experimental data (Jin et al., 2006). Additional test data at elevated deformation rates are needed and should be included in future work.

- The properties of the spinal cord grey and white matter were lumped together in the present study. The primary intention of the spinal cord FE model developed in this

study was to provide a continuum model amenable to implementation in a full HBM for prediction of spinal cord deformation following impact. In this context, modeling the white and gray matter as separate entities would present challenges due to the requisite small element size (0.4 mm) for differentiation of this tissue boundaries in comparison to the relatively large whole-body average element size of 1.8mm of the HBM (Barker and Cronin, 2021). Moreover, the white matter of the spinal cord has been more frequently characterized in the published data at the strain-rate regime corresponding to the dynamic compression that can be observed during SCI (Sparrey and Keaveny, 2011; Jannesar et al., 2018). Furthermore, previously published studies revealed that separating the spinal cord to white and gray matter had little effect on the resulting deformation under transverse impact loading (Persson et al., 2011). Although modeling the individual white and grey matter tissues may be beneficial in understanding SCI at a local level, additional work is required to identify specific injury thresholds for the individual spinal cord white and grey matter tissues.

The current study identified and validated material parameters in a continuum-level hyper-viscoelastic constitutive model for the spinal cord tissue and parameters of a hyperelastic constitutive model for the pia mater. Data used in fitting the material parameters were independent of the impact test validation data; once obtained, material model parameters were not changed to improve the outcome of the validation simulations. The pia mater reduced the deformation of the SCP complex resulting from transverse loading. The fitted constitutive models were validated against two tissue-level experiments with an overall good correlation to independent experimental data.

Chapter 4

Comparison of Numerical Methods for Cerebrospinal Fluid Representation and Fluid-Structure Interaction During Transverse Impact of a Finite Elements Spinal Cord Model

This chapter is an adapted version of the manuscript published in the International Journal for Numerical Methods in Biomedical Engineering as 'Rycman, A., McLachlin, S., and Cronin, D. S. (2022). Comparison of Numerical Methods for Cerebrospinal Fluid Representation and Fluid-Structure Interaction During Transverse Impact of a Finite Element Spinal Cord Model'. Publisher reuse certificate was granted and is attached at the end of this thesis.

4.1 Introduction

The presence of the CSF layer in spinal cord FE models is crucial for obtaining accurate deformation of the spinal cord under different loading conditions (Horgan and Gilchrist, 2003). However, the degree of influence of the FSI between the CSF and spinal cord deformation during impact for different numerical implementations of the CSF is unknown. Moreover, some numerical approaches for FSI may be more suitable and practical (i.e., computationally efficient) for incorporation into full HBM for spinal cord injury risk prediction during impact, while also retaining sufficient biofidelity. To better understand this phenomenon, the objectives of this chapter were two-fold. First, an orthotropic hyperelastic constitutive model was fit to experimental data for the dura mater. Second, building on the FE model of the spinal cord complex (i.e., spinal cord and pia mater) presented in Chapter 3, the dura mater and CSF were incorporated to examine four numerical methods: Lagrange, Pressurized Volume, Smoothed Particle Hydrodynamics, and Arbitrary Lagrangian-Eulerian to represent FSI of the spinal cord during impact. The computational models were quantitatively assessed with an experimental dataset comprising three transverse pellet impacts to the spinal cord complex to assess the accuracy of the impact response and computational efficiency of the FSI methods.

4.1.1 Experimental Investigations of Spinal Cord Impacts

Several experiments investigating the spinal neural tissues response to impact have been conducted using live in vivo animal tests with exposed spinal tissues (Kearney et al., 1988; Kloos et al., 2005; Maikos and Shreiber, 2007; Sparrey et al., 2008; Salegio et al., 2016). However, recreating these complex environmental and boundary conditions in the FE environment is challenging due to complicated interactions of the tissues and subject-specific spinal cord geometry. A detailed experimental study by Persson et al., 2009 considered in vitro impacts on the bovine cord complex (spinal cord-pia mater surrounded by the CSF and dura mater) (Persson, 2009; Persson et al., 2009) (Figure 4.1A). The impacts were conducted with well-defined boundary conditions and impact severities approximating those of a vertebral burst fracture. In the experiment, the spinal cord complex specimens were 140 mm in length. The experimental protocol stated that the natural CSF was replaced with the pseudo-CSF (0.9% saline solution) with similar mechanical properties to the CSF (Ellis et al., 1992; Brydon et al., 1995). Spinal cord complex specimens were freeze-clamped at both ends using dry-ice (Persson, 2009). Then, specimens were subjected to 8% engineering tensile pre-strain in the longitudinal direction, followed by a relaxation period. Three pellets of the same mass but with differing impact face areas were used (314 mm^2, 157 mm^2, and 77.5 mm^2) (Figure 4.1B) to impact the specimens at a nominal velocity of 4.5 m/s. The impact event was recorded with a high-speed camera (4500 fps) from which the displacement-time response of the pellet was determined.
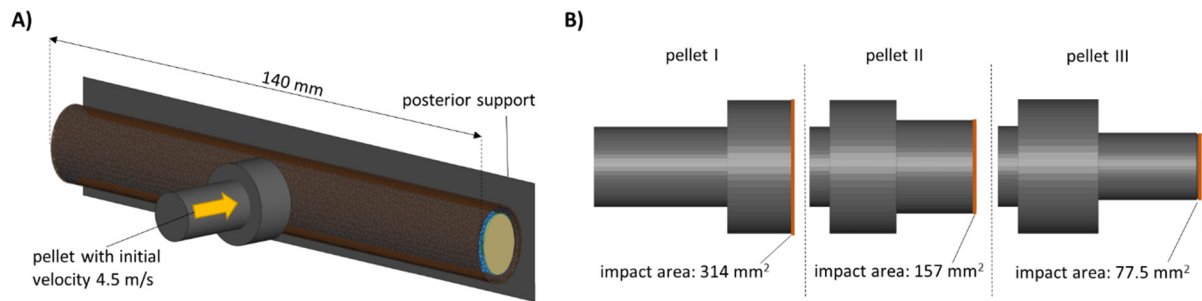
Figure 4.1: A) FE model of transverse pellet impact on spinal cord complex used to assess four different numerical approaches to model CSF. B) Geometry and impact area of the three different pellet configurations; impact surface was highlighted with red lines on each pellet (Persson et al., 2011b).

4.2 Material and Methods

4.2.1 Spinal Cord Material Models and Parameters

A nonlinear orthotropic hyperelastic constitutive model was identified to represent the tissue-level experimental data for the dura (Borrvall et al., 2015). Experimental stress-strain curves in the longitudinal and circumferential directions were implemented directly into the constitutive model (Shetye et al., 2014) (Table 4.1). Single element and multi-element verification simulations were performed to confirm the material response was in agreement with the experimental data prior to implementation in the spinal cord complex model. In the current study, a value of 0.35 mm was used to represent the thickness of the dura mater (Shetye et al., 2014).

Two material models were used to model mechanical response of the CSF. The first was a Newtonian Fluid material model that was previously used to represent the mechanical behaviour of cranial CSF (Chafi et al., 2009; Singh et al., 2014; Yucesoy et al., 2018). This material model calculates hydrostatic (pressure) stresses using a linear bulk modulus multiplied by volumetric strains, whereas the deviatoric stresses are calculated based on the viscous damping coefficient (VC), element characteristic length (ΔL), sound speed (C_0), fluid current density (ρ), and deviatoric strain rate ($\dot{\varepsilon}_{ij}$) (Hallquist, 2006) (Equation 4.1).

$$S_{ij} = VC * \Delta L * C_0 * \rho * \dot{\varepsilon}_{ij}$$

Equation 4.1: Relationship used to calculate deviatoric part of stress (Sij) in a Newtonian fluid material model.

The second material model characterized the bulk mechanical response of the CSF with a Mie-Grüneisen equation of state (EOS) (Equation 4) including a dynamic viscosity of 8.9×10^{-10} GPa*ms (Panzer et al., 2012) and cavitation pressure cut-off value (P_{cut}) of -180kPa (Bustamante and Cronin, 2019) (Table 4.1).

$$p = \rho_0 C^2 \mu \frac{\left[1 + \left(1 - \frac{\gamma}{2}\right)\mu\right]}{[1 - (S_1 - 1)\mu]^2} \ (\mu > 1); p = \rho_0 C^2 \mu \ (\mu < 1); \text{where } \mu = \frac{\rho}{\rho_0} - 1$$

Equation 4.2: Mie-Grüneisen equation of state (EOS) that relates the pressure with change in density for expanded and compressed material (Hallquist, 2006).

Table 4.1: Summary of the material properties dura mater, and CSF used in the finite element model.

Material	Constitutive model	Model Parameters				References
Dura mater	Orthotropic hyperelastic	Material stress-strain curves for the longitudinal and circumferential directions.	$v = 0.45$	$\rho = 1000$ kg/m^3		Shetye, Deault, and Puttlitz 2014
CSF	Newtonian fluid	K = 2.19 GPa	$\rho = 1000$ kg/m^3		VC = 0.1	Chafi et al. 2009; Richardson and Wissler 1996
	Mie-Grüneisen EOS	C = 1483 m/s $S_1 = 1.75$ $\gamma = 0.28$	$\rho = 1000$ kg/m^3 $P_{cut} = -180$ kPa		$\mu = 8.9 \times 10^{-10}$ GPa*ms	Tan, Lee, and Tsangalis 2009

4.2.2 Computational Modelling of Ex-vivo Impact Experiments

The experiments undertaken on the bovine spinal cord complex (Persson et al., 2009) were used for model assessment in the current study. The FE model matched the average geometry of the bovine spinal cord complex in the experiment, reportedly elliptical with an anterior-posterior diameter of 13.92 ± 2.31mm and average aspect ratio to the sagittal diameter of 0.76 (Jones et al., 2008; Persson, 2009; Persson et al., 2009) (Figure 4.1). Nerve roots were not present in the experiment (Persson et al., 2009) and were not included in the current FE model.

63

The geometry was meshed using a commercial pre-processor (HyperMesh, Altair Engineering, Troy, USA). The dura was meshed with an average shell element length of 0.8 mm (11,200 shell elements), the spinal cord was meshed with an average element size of 0.8 mm (37,100 hexahedral elements) and the pia mater was meshed with 9,100 hexahedral elements, using coincident nodes to the outer surface of the spinal cord. Convergence of the spinal cord-pia mater complex mesh was conducted previously (Rycman et al., 2021), and was used in the current study.

The CSF was modeled using four numerical methods (Figure 4.2): (1) pressurized volume requiring no additional elements and modelled as an enclosed space with a prescribed pressure-volume response, (2) traditional Lagrangian hexahedral elements (22,400 elements), (3) a SPH grid (43,049 elements), and (4) an ALE mesh with an average domain element size of 0.45 mm (140,600 grid elements). In addition, a control model without CSF was created to understand the overall effect of the CSF. The Lagrange mesh was simulated using a Newtonian fluid model, denoted as Lagrange Fluid. The SPH and ALE methods were simulated using both a Newtonian fluid model (SPH Fluid, ALE Fluid) and a Mie-Grüneisen EOS (SPH EOS and ALE EOS) (Table 2).

Table 4.2: Simulation matrix and nomenclature used in the study.

	Lagrange	Pressurized Volume	SPH	ALE	Control Model
Newtonian Fluid	Lagrange Fluid	PV (requires no material model)	SPH Fluid	ALE Fluid	Control Model (CSF not included)
Mie-Grüneisen EOS	Not Applicable		SPH EOS	ALE EOS	

The PV approach required defining the enclosed space between the spinal cord and dura using a surface or segments created from element faces. The implementation then calculates the enclosed change in volume between the dura mater and the pia mater and corresponding change in pressure at each time step. The pressure-volume relationship was linear (with a slope of 2.19 GPa) for the CSF (Bilston, 2011). The Lagrange mesh was implemented using hexahedral

elements since tetrahedral elements may overestimate pressure (Puso and Solberg, 2006; Singh et al., 2014). Implementation of the SPH elements required the definition of nodes within the CSF space between the dura and pia mater. SPH elements were then defined at the location of each node.

For each numerical method, the size of the mesh was determined through a convergence study using Richardson extrapolation to estimate the mechanical response of the theoretical 0 mm mesh size. The Lagrange implementation was simulated with 1.6 mm, 0.8 mm, and 0.4 mm mesh size; the SPH implementation was simulated with 10,594, 43,049, and 156,931 SPH elements, and the ALE implementation was simulated using a Eulerian domain element size of 0.8, 0.6, and 0.45 mm. All mesh sizes investigated provided converged results with respect to the maximum deformation and were in the asymptotic solution region, with the fractional error estimator (E) not exceeding 3% (Roache, 1997, 1998).
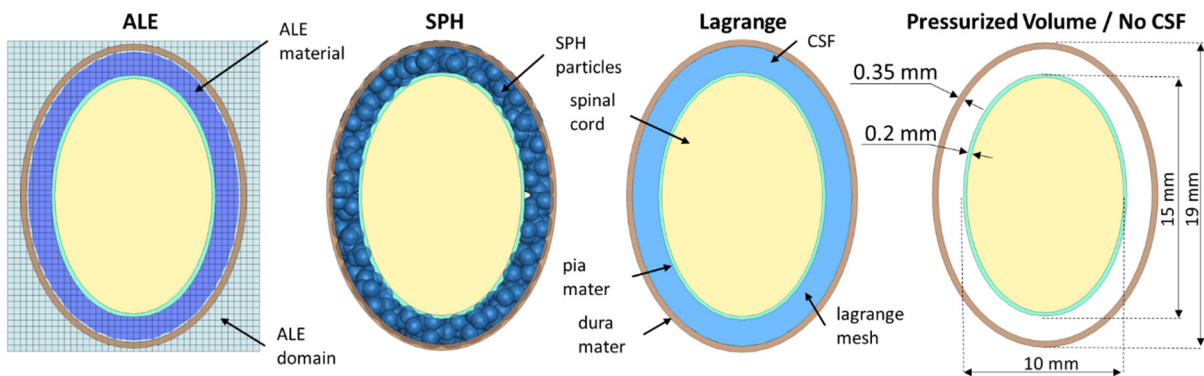
Figure 4.2: Approximation of spinal cord complex cross-sectional geometry (spinal cord: yellow, pia mater: green, CSF: blue, dura mater: brown) with four different numerical implementations of the CSF layer.

The pellets were meshed using hexahedral elements (Figure 4.1B) with an element size of 0.8 mm to ensure an accurate representation of the pellet impact area and mass. An initial velocity-based boundary condition was prescribed to the pellets to match the nominal 4.5 m/s velocity reported in the description of the experiment.

The FE models were solved using a commercial explicit FE code (LS-DYNA MPP R10.1, double-precision, LST, Livermore, CA) on Intel Xeon E5-2683 2.1 GHz processors. The simulation results, including the pellet trajectories, CSF layer compression, and internal energy states were extracted and analyzed using a commercial post-processing software (LS-PrePost version 4.5.24). Pellet trajectories obtained from the simulation results were compared to the average experimental results with cross-correlation analysis (Gehre et al., 2009). Finally, the computation times of the simulations were compared between different numerical approaches, normalized to the traditional Lagrangian numerical solution time.

4.3 Results

4.3.1 Dura Material Model and Parameters

The orthotropic hyperelastic constitutive model for the dura mater provided an excellent fit (R^2 = 0.99) in the range of the reported experimental data (Shetye et al., 2014) (Figure 4.3). Beyond the range of the reported experimental data, the material model response was extrapolated with the slope calculated based on the last two data points for each curve.
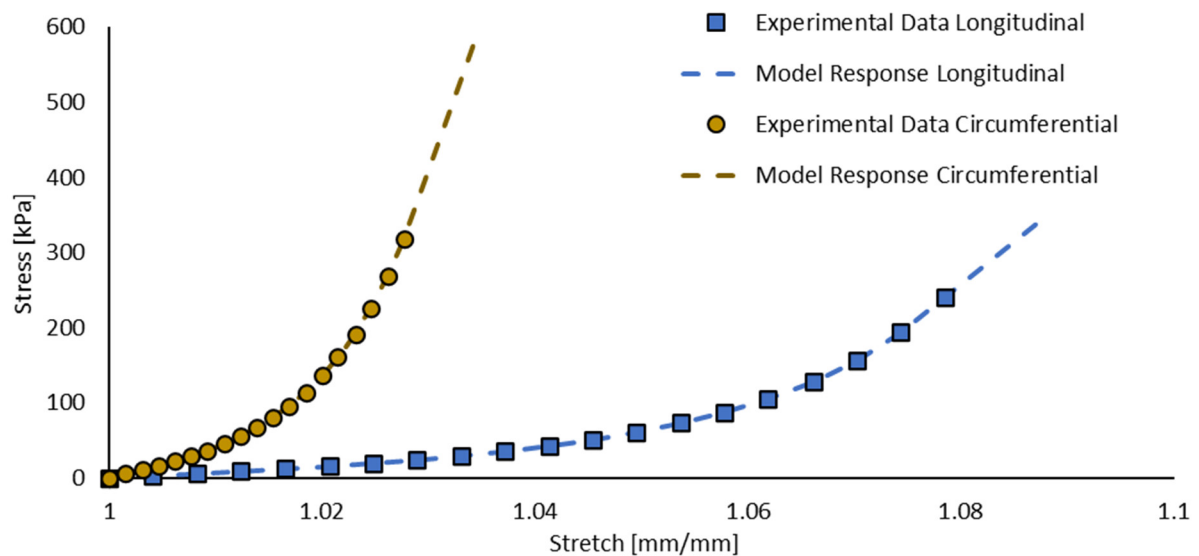
Figure 4.3: Single element verification of the dura mater material model in the circumferential and longitudinal directions, compared to experimental data (Shetye et al., 2014).

4.3.2 Computational Modelling of Ex-vivo Impact Experiments

A typical simulation involved the pellet, with an initial velocity of 4.5 m/s, initially impacting the dura mater. As the impact progressed (approach phase, 0 to ~3 ms in Figure 4.4), the dura mater deformed into the CSF space by local bending around the circumference of the pellet. Deformation of the dura resulted in a local increase in the CSF pressure. At the same time, load was transferred to the spinal cord, resulting in localized compression of the cord beneath the impact site and stretching of the cord around the periphery of the impact zone. As the impact progressed in time, the deformation of the spinal cord complex, specifically the cord itself, increased as the pellet decelerated, reaching a maximum when the pellet velocity reached zero (t~3 ms). The pellet velocity then reversed as the spinal cord complex unloaded (t>3 ms), demonstrating asymmetry between loading and unloading.

Implementing the CSF layer with the four different numerical methods resulted in the peak deformation values that occurred at a similar time (~3 ms). The peak deformation magnitudes of the spinal cord complex varied from -8% to +26% compared to the average kinematic experimental data from the three pellet impacts (Persson, 2009; Persson et al., 2009) (Figure 4.4). For each of the numerical approaches, a consistent pattern was observed: the maximum deformation of the spinal cord complex increased as the impact area of the pellet decreased (Figure 4.5).
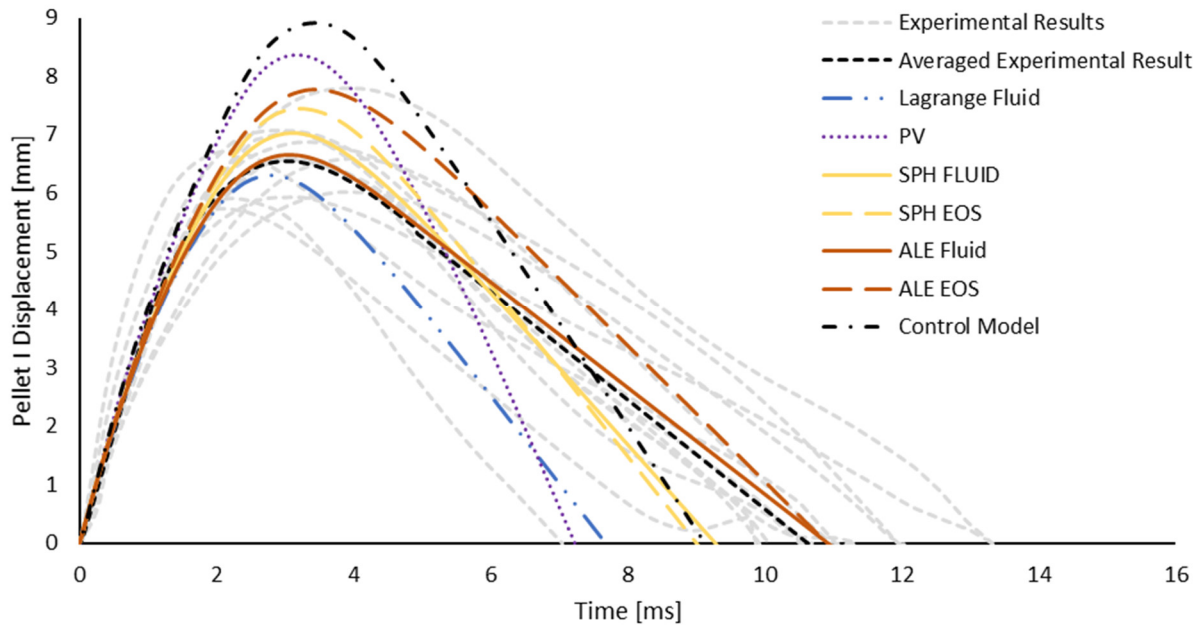
Figure 4.4: Kinematics of Pellet I response using Lagrange Fluid, Pressurized Volume (PV), Smoothed Particle Hydrodynamics (SPH), and Arbitrary Lagrangian-Eulerian (ALE) to model the CSF in comparison to the control model and experimental data. ALE and SPH methods were simulated using both an elastic fluid model (FLUID) and an equation of state model (EOS).

Three of the numerical methods used for FSI modelling of the CSF layer (ALE, SPH, and Lagrange) resulted in a maximum deformation of the spinal cord complex in the range of the reported experimental data for all three pellets. The maximum deformation exceeded the reported experimental data, on average by 21%, when the CSF was implemented using the pressurized volume approach. Further, the pressurized volume approach had little effect on the maximum deformation, with similar results to the control model where there was no CSF implemented in the model (Figure 4.5). Implementing CSF with Lagrange elements predicted the stiffest response, with the maximum deformations of the spinal cord complex below, on average by 5%, the experimental average for all three pellets.
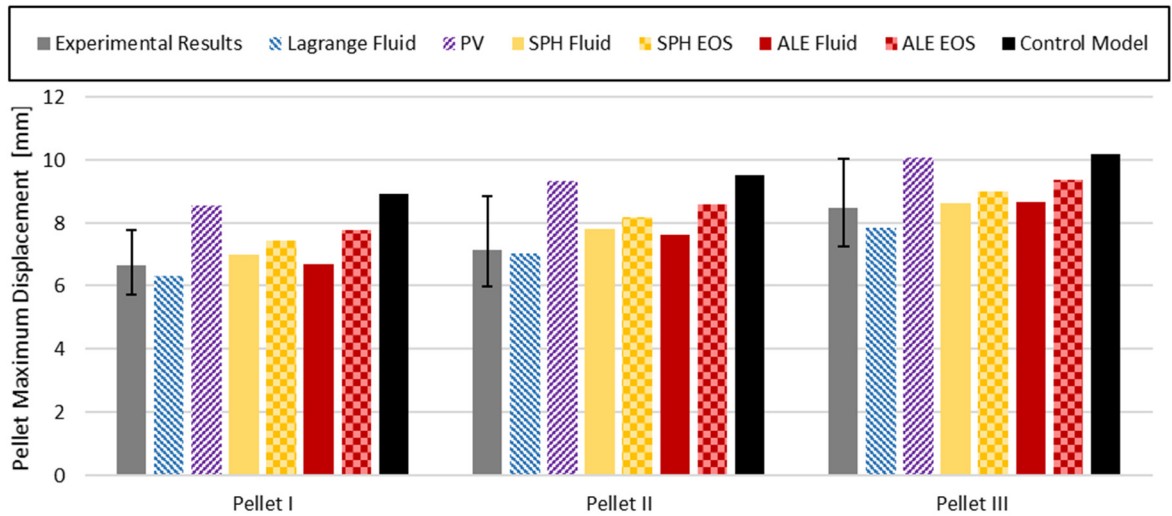
Figure 4.5: Deformation of the spinal cord complex for four numerical methods to model the CSF, compared to experimental data. The error bars represent the minimum and maximum deformations measured in the experimental data (Persson et al., 2009).

Two characteristic time results from the model, (1) total duration of the impact and (2) time to maximum deformation, were compared to experimental data. The SPH, ALE and PV numerical methods predicted the time to maximum deformation within the experimental range (Figure 4.6). The ALE and SPH methods predicted time to maximum deformation with the smallest error (16.4%) with respect to the mean experimental results. Lagrange formulation showed the highest percentage error of 28.1% in predicting the time to maximum deformation compared to the experimental average. In general, all numerical approaches predicted the total duration of the impact to be lower than the experimental average at least for one pellet. The ALE Fluid approach resulted in an impact duration within the experimental results for all three pellets and the lowest percentage error of 9.13% from the experimental average results.
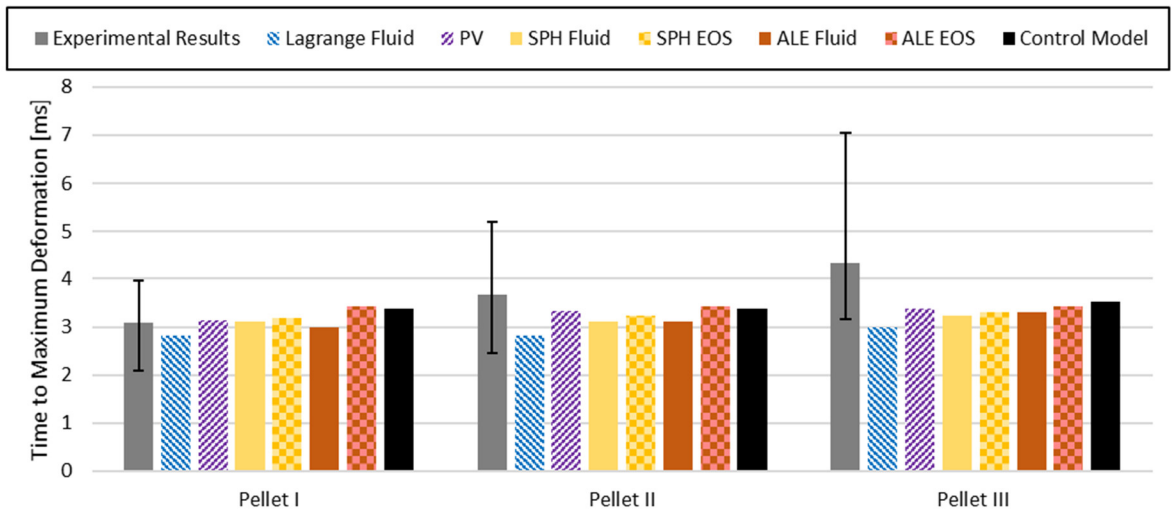
Figure 4.6: Time to maximum deformation of the impact for four numerical methods to model CSF, compared to experimental data. The error bars represent the minimum and maximum values.

The thickness of the CSF layer at the maximum pellet displacement was calculated as a ratio of the change in thickness to the initial CSF thickness (Figure 4.7). Finally, the cross-correlation rating and computational time (Table 3) were calculated for each impact case.
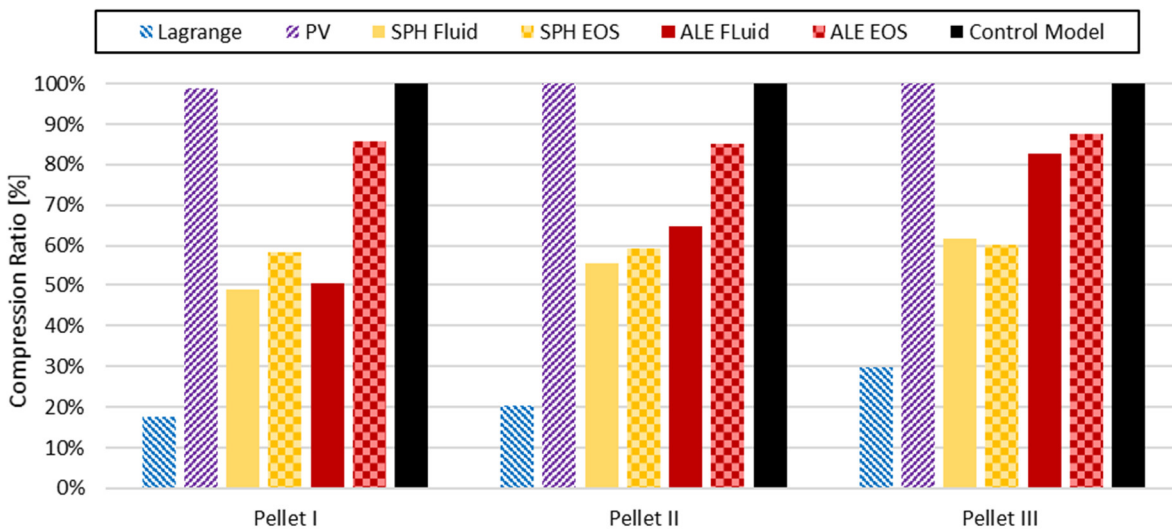
Figure 4.7: Change in annular dimension (CSF thickness) for the four numerical methods, expressed as percent compression and measured at the maximum pellet displacement.

70

Table 4.3: Cross-correlation ratings and normalized computation time to the Lagrange Fluid implementation of four numerical methods for CSF representation and control model without CSF.

CSF Representation	Cross-Correlation Rating				Normalized Computation Time
	Pellet I	Pellet II	Pellet III	Average	
Lagrange Fluid	0.86	0.84	0.79	0.83	1.00
PV	0.86	0.87	0.98	0.90	0.59
SPH Fluid	0.98	0.98	0.88	0.94	0.87
SPH EOS	0.94	0.96	0.92	0.94	0.89
ALE Fluid	0.96	0.98	0.92	0.96	5.00
ALE EOS	0.85	0.89	0.97	0.90	4.97
Control Model	0.80	0.84	0.96	0.87	0.59

4.4 Discussion

Simulation results from the current study revealed the importance of the non-linear material model used to represent dura mater tissue and capture deformation energy during spinal cord impact modelling. At the state of maximum deformation, nearly all of the kinetic energy of the pellet was transformed into internal energy stored in the soft tissues, approximately 32-35% of which was stored in the dura mater. This contrasts other recent FE spinal cord models, where a linear elastic modulus was used to characterize the dura mater, ranging from 2.3 MPa to 231 MPa (Henao et al., 2018; Stoner et al., 2020). Linear elastic models do not consider the non-linear response and orthotropy of the dura mater that will influence the prediction of overall strains and stresses in the spinal cord, leading to inaccuracies in predicting spinal cord deformation during impact. The non-linear material properties used in the current study better captures orthotropic material behaviour of the dura mater reported in experimental studies (Runza et al., 1999; Persson et al., 2010; Shetye et al., 2014).

The predicted asymmetry of the pellet response (loading and unloading), also reported in the experiments, was attributed to the viscoelastic nature of the materials models used for the spinal cord and pia mater, and the implementation of the CSF. The presence of the CSF layer reduced the overall deformation of the spinal cord complex under transverse impacts relative to the control model without CSF. The PV approach had very little effect on the spinal cord

71

deformation relative to the control model without CSF, suggesting that inertial forces acting on the fluid during impact have a more dominant role in stopping the impactor than the pressure induced inside the CSF layer alone. A limitation of the PV method is that the same pressure was applied to the whole volume such that there was no pressure gradient in the impact zone. Arguably, the PV numerical implementation of the CSF assumed constant pressure and did not accurately represent the mechanical response of the tissue during focal impact. Opposingly, the Lagrange mesh did not allow for significant flow of the CSF material out of the direct impact zone, resulting in overall lower deformation to the spinal cord and a stiffer response compared to the other methods. The cross-correlation ratings indicated that modelling CSF with either the SPH or ALE numerical approaches, regardless of the material model used, resulted in a high biofidelity compared to the experimental dataset. Of note, none of the material models used in the current study were calibrated or altered to improve the cross-correlation ratings of the impact simulations relative to the impact test data, and the same material properties with converged mesh sizes for each CSF representation were used.

There is currently limited understanding of the CSF movement and flow during focal impact of the spinal cord complex. This study predicted CSF outflow directly beneath the pellets during impact and the associated deformation of the spinal cord as a result. In the control case, without CSF implementation, and in the PV approach, the CSF layer collapsed entirely, denoted by a 100% compression ratio of the initial thickness compared to the thickness at maximum deformation (Figure 4.7). The Lagrange Fluid formulation had the smallest deformation of the CSF layer (23%), with most of the total deformation of the spinal cord complex being concentrated in the spinal cord and pia mater tissue. Surprisingly, the CSF layer modelled with the ALE Fluid and ALE EOS approach did not entirely collapse even under the most severe impact case. The SPH Fluid and SPH EOS methods predicted compression of the CSF layer ranging from 44 to 62% for different pellet impacts. Although the experiments assumed collapse of the CSF layer, there was no experimental measurement to support this finding (Persson, 2009; Persson et al., 2009). Therefore, it is unknown whether the CSF layer should fully collapse under the transverse impacts investigated in the present study.

Two material models were investigated for the CSF Fluid and EOS. Modeling the CSF using the Mie-Grüneisen EOS provided stable results for the SPH and ALE methods; however, the Lagrange implementation terminated early due to negative volume in the solid elements. All simulations ran to completion with the Fluid material model. The main difference between the Fluid and EOS material models was the representation of fluid dynamic viscosity. The EOS used a traditional viscosity value, while the Fluid model used a Viscosity Coefficient (VC). The VC resulted in more resistance to fluid motion so that the compression of the CSF layer and maximum displacement of the pellets were lower than in the EOS model. Ultimately, the EOS model is recommended, since it utilizes physically measured values of viscosity and bulk modulus, while the VC approach in the Fluid model, which has been used in other studies, has a direct dependency on element size and can therefore introduce unphysical response.

In the subarachnoid space, which is occupied by the CSF, fibrous tissues are present i.e., dente ligaments, arachnoid matter, blood vessels (Nicholas and Weller, 1988) that were not represented in the present model. Such tissues could restrict CSF flow in the subarachnoid space. In a previous two-dimensional FE study of the cranial CSF, the Fluid material model provided fair match to the experimental data (cross correlation = 0.4) while the EOS model provided lowest match (cross correlation = 0.27) to the experimental data (Duckworth et al., 2021). However, it should be cautioned that compensating for the additional tissues through modifications to the fluid viscosity representation requires additional experimental data.

The characteristic length and number of elements in a FE mesh primarily drives the calculation time of the simulation. As the finite elements are deformed and the characteristic length changes, the FE explicit solver adjusts the time step to fulfill the Courant-Friedrichs-Lewy condition (Hallquist, 2006). The control model had the shortest computation time due to the reduced number of elements relative to models including CSF. Although the ALE method produced excellent quantitative results, a significant drawback to this numerical method was the increased computation time (Table 4.3), requiring five times the computational time relative to the Lagrangian mesh. The SPH method produced pellet response comparable to those of ALE but with a massively reduced computational time. The SPH computation time

was slightly shorter (0.87 to 0.89) compared to the Lagrange method, since the Lagrangian approach suffers from decreased time step as the elements are deformed. Further, the deformations with the Lagrange approach tend to be larger than other methods since these elements are limited in terms of overall motion. Even though the explicit code solves more complex functions to calculate stress states in SPH elements (Xu and Wang, 2014; Yreux, 2018), the SPH elements were able to flow out of the high pressure zone, resulting in a similar overall computation time.

The developed FE model of the spinal neural tissues has some recognized limitations. The dura mater constitutive material model was based on the tensile response of the ovine spinal dura mater due to the lack of available test data on bovine or human dura mater. The geometrical dimensions of the dura mater and CSF thickness were fixed for all numerical simulations in this study. A previous study established that a thicker CSF layer leads to smaller deformations in the spinal cord (Persson et al., 2011a). Moreover, the variability of the experimental results may be explained in part by variability of the tissue dimensions, which were not examined in this study. Neither the experimental study or the FE model used in the current study included the effect of nerve roots or denticulate ligaments which could potentially limit translation to in vivo studies.

4.5 Conclusions

This chapter highlighted that the dura mater and CSF layer have an important effect on spinal cord compression under transverse impact loading. Continuum numerical approaches used in this study (ALE, SPH and Lagrangian) resulted, on average, in lower deformation of the neural tissues by 22.3% compared to the control model without the CSF layer. Modelling the CSF layer using the ALE approach with a Fluid material model matched the experimental results with the highest cross-correlation rating (0.96); however, the SPH method resulted in a very good match (0.94), for both material models used, with the reported experimental data, and a significantly reduced computational time compared to the ALE approach (Table 4.3). In this case, the use of SPH for numerical modelling of the FSI of the spinal cord may be most suitable for incorporating the CSF in HBM examining spinal cord impact and injury risk prediction.

Chapter 5

Development of Geometry and Mesh of the Cervical Spinal Cord Tissues for the GHBMC 50th Percentile Male Model

This chapter was previously submitted to the Annals of Biomedical Engineering as 'Rycman, A., McLachlin, S., and Cronin, D. S. (2022).' Cervical spinal cord boundary conditions affect brain tissue strains in frontal, lateral, rear, and oblique impact simulations.' The publisher allows to reuse author's content. If accepted authors will apply for reuse certificate.

5.1 Introduction

Yet, to date, there has been no implementation of the cervical spinal cord and surrounding neural tissues in any HBM. Incorporating an anatomically correct spinal cord model into a full HBM like GHBMC M50 requires altering the brain tissue boundary conditions, which has the potential of affecting the resulting brain tissue deformations during simulated impact conditions.

The aim of this chapter was to address current limitations of the GHBMC M50 model by developing an implementation of a comprehensive spinal cord model. This chapter describe the process of creating a subject-specific mesh geometries of the spinal cord, nerve roots, CSF, dura mater and neural ligaments based on a magnetic resonance imaging (MRI) dataset (Gayzik et al., 2011b, 2011a) and literature data (Okada et al., 1994) and integrating into the GHBMC M50 Head-Neck model.

5.2 Material and Methods

5.2.1 Geometry of the Cervical Spine Neural Tissues

The geometry of the cervical spinal cord was created based on the subject-specific MRI scan used previously to develop the GHBMC M50 model (Gayzik et al., 2011b). The MRI dataset was collected using a 1.5T Twin Speed scanner (GE, Milwaukee, WI) with a matrix resolution of 256 x 192 pixels (Gayzik et al., 2011a). The MRI volumes were imported to the imaging

software (3D Slicer v4.8.1) for 3D image segmentation and measurement of the spinal cord tissue dimensions. From the MRI transverse cross-sections of the M50 subject, the sagittal (depth) and coronal (width) dimensions of the spinal cord were measured at the midpoint of each cervical vertebral level (C1 to C7). Cross-sectional dimensions measured from the subject-specific MRI were compared to the literature data to verify anatomical differences (Kameyama et al., 1996; Fountas et al., 1998; Ko et al., 2004).
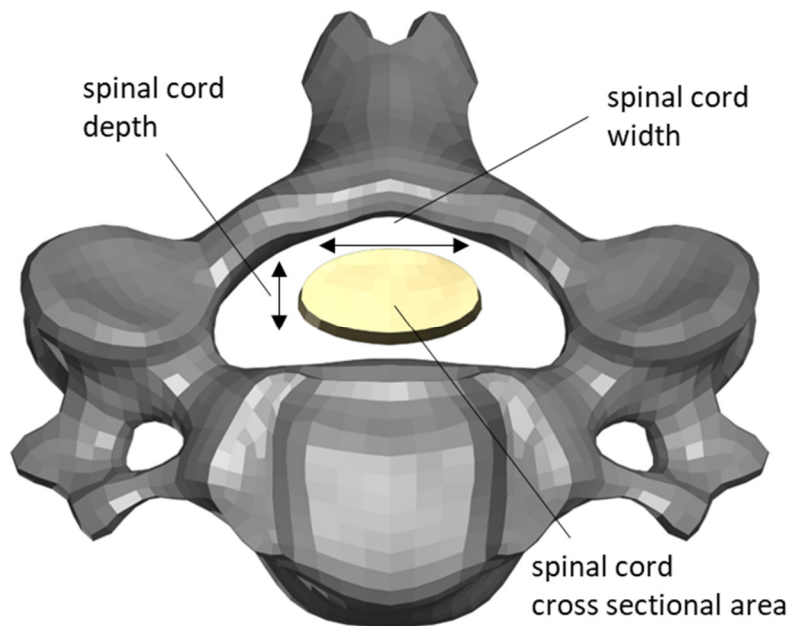
Figure 5.1: Spinal cord dimensions: depth, width, and transverse cross-sectional area compared to experimental data.

Accurate measurement and the identification of the dura mater shape and thickness from MRI scans was limited by poor contrast between of the adjacent tissues. Instead, the geometry of the dura mater was based on the calculation of the area ratio of the dura mater in the spinal canal. The transverse areas of the dura mater and the spinal canal at each cervical level were reported in the literature (Okada et al., 1994).

5.2.2 Development of the Nerve Roots

The diameter of the nerve roots was challenging to consistently measure from MRI scans due to the limited resolution and contrast in the existing MRI dataset. The nerve roots emerge from the spinal cord in the form of many rootlets that also introduce an additional challenge in acquiring nerve roots dimensions. Hence, the geometry of the nerve roots was determined from measurements reported in the literature (Liu et al., 2015), defined as a circular cross-sectional shape using the reported diameter for each of the vertebral levels (Table 5.1). However, it was not feasible to model dorsal and ventral nerve roots separately and maintain a computationally feasible mesh size. As such, the dorsal and ventral bundles for each level were merged and represented by a single bundle in the detailed GHBMC M50 Head-Neck model.

Table 5.1: Calculated cervical nerve roots area and diameters (based on Liu et al., 2015).

Nerve root	Area [mm^2]	Diameter [mm]
C1	1.9	1.6
C2	6.8	2.9
C3	7.0	3.0
C4	6.4	2.9
C5	14.1	4.2
C6	16.4	4.6
C7	20.6	5.1
C8	14.4	4.3

The neural ligaments were incorporated (i.e., denticulate (Tubbs et al., 2001; Ceylan et al., 2012) dorsal meningovertebral (Shi et al., 2014; Chen et al., 2015), anterior dural (Hofmann's) (Wadhwani et al., 2004; Tardieu et al., 2016) and extraforaminal ligaments (Kraan et al., 2011)) to provide attachment to the cervical spinal cord in the spinal canal and anchor the cervical spinal nerves in the extraforaminal magnum. The placement of each ligament was reviewed against anatomical description provided in the literature (Kraan et al., 2011; Ceylan et al., 2012; Shi et al., 2014; Chen et al., 2015). All implemented neural ligaments were represented using

one-dimensional axial elements with a formulation allowing only tensile loading transfer. This meshing strategy was previously used to represent spine ligaments in the detailed GHBMC M50 Head-Neck model (Barker et al., 2017; Lasswell et al., 2017)

The spinal cord, dura mater, and nerve root geometries were meshed using a commercial finite element pre-processor (HyperMesh, Altair Engineering, Troy, USA) (Figure 1). The neural tissues were represented using fully integrated Lagrange elements (solid or shell). Cerebrospinal fluid (CSF) was modelled using meshless Smoothed Particle Hydrodynamics (SPH) particles, following a previously reported implementation, which was demonstrated to be computationally efficient and biofidelic for modeling fluid-structure interaction between the spinal cord, SPH and dura (Rycman et al., 2022).

5.3 Results

5.3.1 Spinal Cord Geometry

For the GHBMC M50 scanned subject, the width of the spinal cord reached a peak of 14.2 mm at the C4 level, then decreased to 10.3 mm at the C7 level (Figure 5.2). A similar pattern was observed in the reported literature data (Kameyama et al., 1996; Fountas et al., 1998; Ko et al., 2004). The depth of the spinal cord also followed trends observed in the literature data, with the depth of the spinal cord gradually decreasing with vertebral levels (Figure 5.3). The measured transverse cross-sectional area was within the variability of the reported data (Kameyama et al., 1996; Ko et al., 2004) (Figure 5.4).
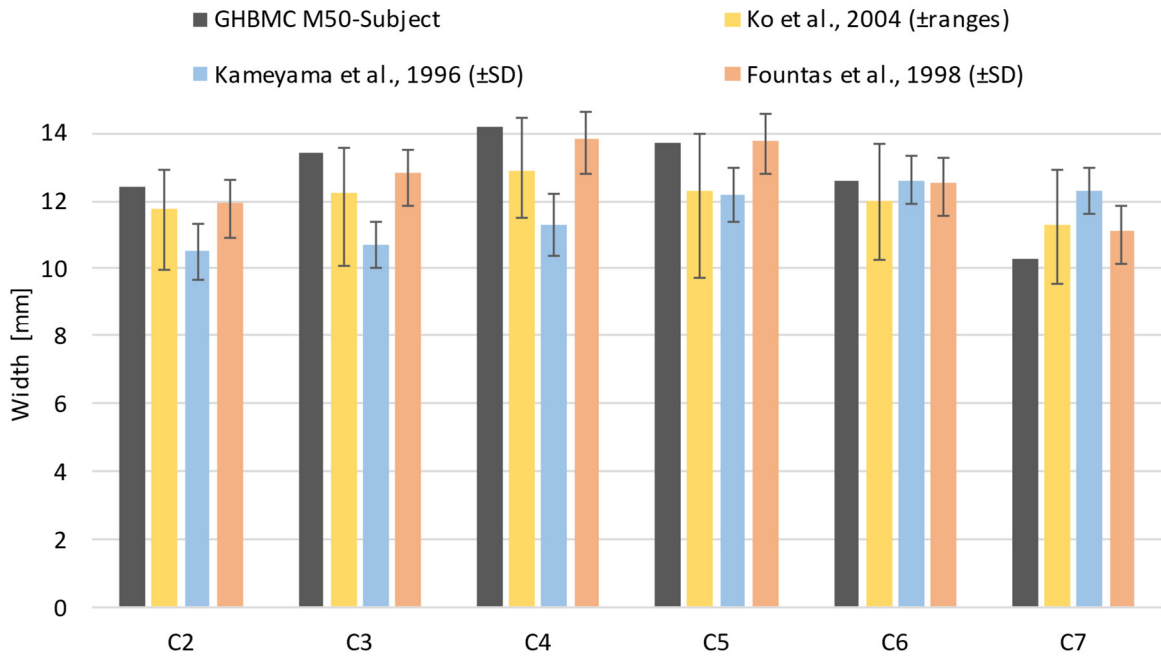
Figure 5.2: Spinal cord width compared to the literature data.
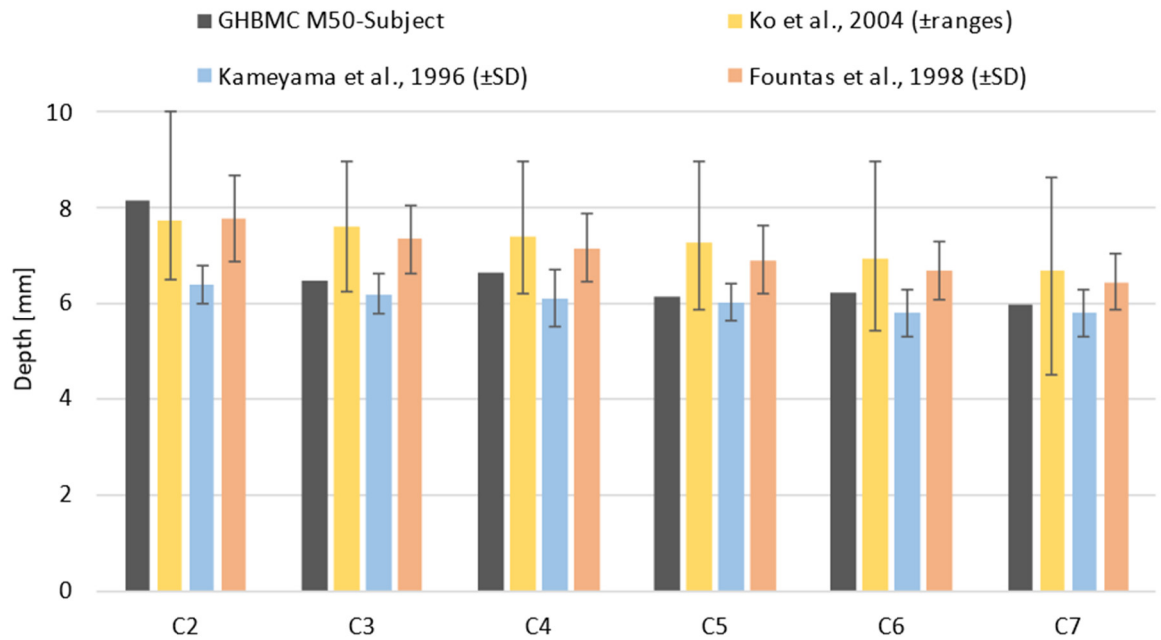
Figure 5.3: Spinal cord depth compared to the literature data.
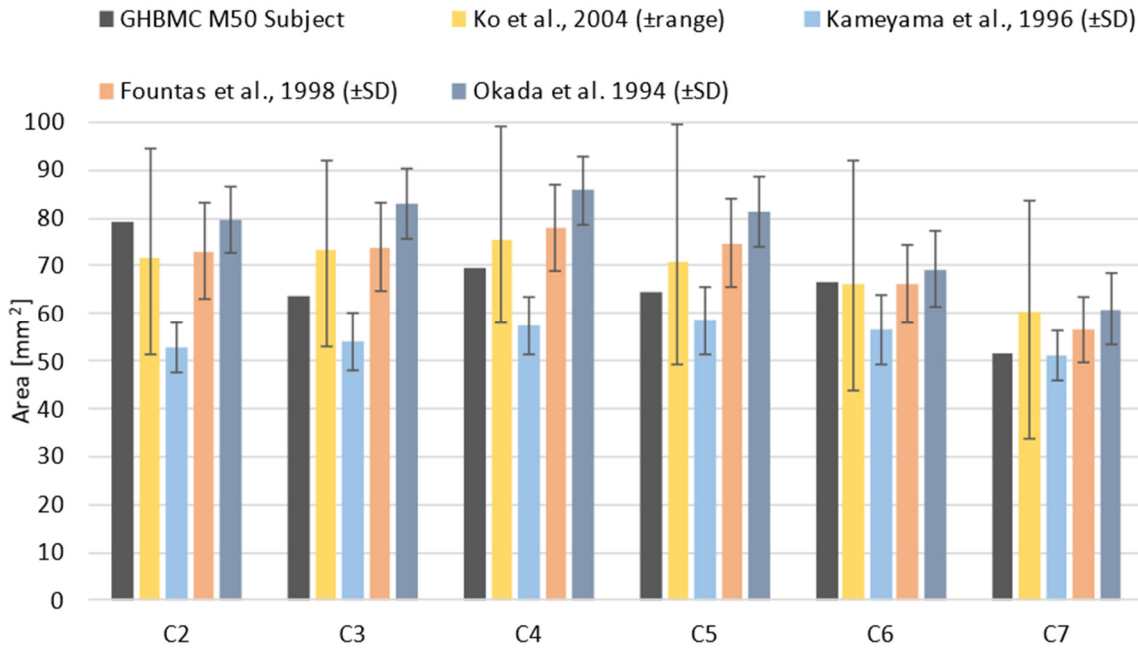
Figure 5.4: Spinal cord cross sectional area compared to the literature data.

The meshing process generated 9,798 hexahedral elements and 13,744 shell elements for the spinal cord model, with an average characteristic length of 0.84 mm and 0.94 mm for solid and shell elements, respectively. More than 99.5% of the elements met rigorous mesh quality standards; Jacobians were greater than 0.3 for solid elements and 0.4 for shell elements, aspect ratios were less than 5.0 for shell and solid elements. The cervical subarachnoid volume was populated with 6,106 SPH elements that represented the CSF. All neural ligaments were implemented using single dimension beam elements that transfer only tensile loading.

5.3.2 Implementation of the Cervical Neural Tissues into the GHBMC M50 Head-Neck Model.

Generated meshes of the cervical neural tissues were integrated into the detailed GHBMC M50 Head-Neck model (Barker and Cronin, 2021). The spinal cord and superior end of the dura mater were connected to the existing cranial neural tissues through shared nodes (Figure 5.5). The superior surface nodes of the created cervical nervous tissues were merged with the

existing inferior surface nodes of the cranial nervous tissues: brain stem, dura mater, and pia mater. The dorsal meningovertebral, extraforaminal and anterior dural ligaments connect the bony part of cervical vertebrae to the dura mater, whereas the denticulate ligaments provide a connection between the spinal cord and dura mater. The inferior part of the spinal cord terminated with an elastic boundary condition that was represented by the implemented cervical neural ligaments, primarily anterior dural ligaments, at the height of the first thoracic vertebra.
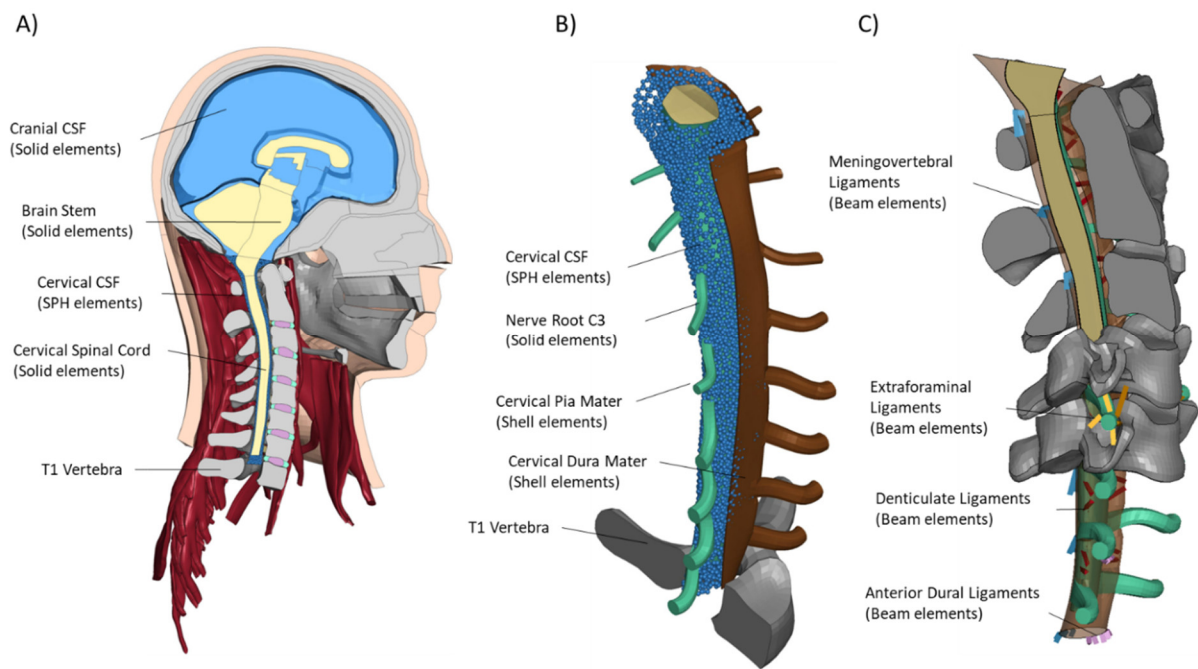
Figure 5.5: A) Median plane section through the GHBMC M50 Head-Neck model, with implemented cervical neural tissues including cerebrospinal fluid (CSF) using smoothed particle hydrodynamics particles; B) isometric and sectioned view of the spinal cord model and associated tissues; C) sagittal view with implemented neural ligaments. Note: some parts were cut in the median plane, and the dura mater was made partially transparent to show the ligaments.

5.4 Discussion

In this chapter, a detailed spinal cord model including neural tissues and CSF was developed, meshed, and integrated into the GHBMC M50 Head-Neck model. In terms of the spinal cord model geometry, the cross-sectional dimensions from the subject-specific MRI dataset were

within the reported averages from the available literature (Kameyama et al., 1996; Fountas et al., 1998; Ko et al., 2004). Possible differences in the spinal cord dimensions between datasets can be explained as a result of different measurement techniques such as MRI, CT myelography, and post-mortem examination. A reinforcing argument for anatomical correctness of the implemented spinal cord geometry in the current study is that the transverse occupation ratio of the spinal cord in the dural sac (39.90%) was almost the same as the calculated average from the published literature data (40.04%) (Kato et al., 2012). As a result, the created geometry and mesh were considered representative of the population and appropriate for the 50th percentile male model.

The SPH approach representing the CSF layer previously demonstrated biofidelic behaviour of the fluid-structure interaction in simulations of spinal cord impact experiments (Rycman et al., 2022). Notably, only the THUMS model contains cervical CSF represented with solid (Lagrangian) elements. However, Lagrangian elements have been shown to exhibit an overly stiff response during the deformation of the spinal cord (Rycman et al., 2022). Arguably, representing the CSF with Lagrangian elements might also overly constrain and anchor the spinal cord in the spinal canal. The SPH approach allows the CSF to flow naturally without applying axial deformations to the spinal cord.

5.5 Conclusions

Implementation of the comprehensive spinal cord in the GHBMC M50 Head-Neck model serves two important objectives. Firstly, this development had provided new capabilities of the HBM to quantify the risk of spinal cord injury during simulated impact conditions. Secondly, the attachment of the spinal cord provides anatomically correct representation of the connection between the brain stem and spinal cord, which was found to influence the deformation pattern of the whole brain tissue in non-injurious impact cases, that are presented in Chapter 6.

Chapter 6

Cervical Spinal Cord Boundary Conditions Affect Brain Tissue Strains in Frontal, Lateral, Rear, and Oblique Impact Simulations

This chapter was previously submitted to the Annals of Biomedical Engineering as 'Rycman, A., McLachlin, S., and Cronin, D. S. (2022).' Cervical spinal cord boundary conditions affect brain tissue strains in frontal, lateral, rear, and oblique impact simulations.' The publisher allows reusing author's content. If accepted, authors will apply for a reuse certificate.

6.1 Introduction

Despite the global effort to prevent traumatic brain injuries (TBI), an upward trend is still observed (Taylor et al., 2017). According to the Centers for Disease Control and Prevention (2019) Surveillance Report, the number of TBI cases doubled between 2006 to 2014, reaching a record high of more than 2.5 million cases. Moreover, literature data (Wedekind and Lippert-Grüner, 2005) suggests that the damage to the brain stem in severe TBI survivors has a negative impact on long-term clinical outcomes. To date, experimental data, animal injury models, and field data have provided crucial knowledge to understand TBI (Meaney et al., 2014). However, the ability to obtain detailed insights into TBI mechanisms remains limited. As an alternative, investigations using FE HBM can be used to augment and enhance understanding of TBI by quantifying brain and cervical spine neural tissue deformations during simulated impact conditions (Melvin and Yoganandan, 2015; Bruneau and Cronin, 2021).

The aim of this chapter was to investigate the effect of the implemented cervical spinal cord on the brain tissue deformation over a range of simulated impact conditions. For the second aim, the influence of the cervical spinal cord model on the whole brain and brain stem tissue deformations were quantified by computing the MPS_{95} during simulated frontal, lateral, rear, and oblique impact scenarios. Moreover, the cumulative strain distribution curves were plotted as a comprehensive way to analyze deformation in the brain tissue and brain stem tissue.

Lastly, a new metric that compared the cumulative strain curves of the brain and brain stem between the models with the spinal cord and without was proposed.

6.2 Material and Methods

6.2.1 Material Properties of the Cervical Neural Tissues

Previously validated material models and constitutive model parameters for the spinal cord, pia mater, dura mater, and the CSF implementation were used in this study (Rycman et al., 2021, 2022) (Table 6.1). With no human cadaveric data available, mechanical properties of porcine denticulate ligaments were used for all cervical levels using available literature data (Polak et al., 2014). The stress-strain curves were digitized (Engauge Digitized v10.6), normalized, averaged, and rescaled to represent the average force-displacement curve (Figure 6.1)
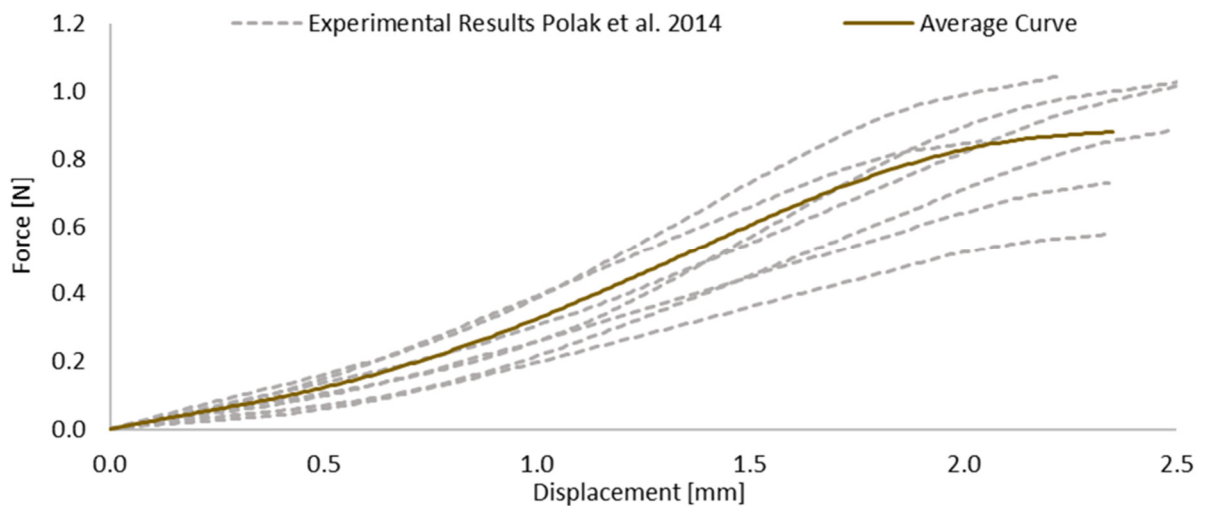
Figure 6.1: Experimental force-displacement curves of the porcine denticulate ligament averaged to one curve that was implemented in the GHBMC M50-O model.

The response of the meningovertebral ligaments to mechanical loading has not been reported in the literature. However, the thickness and diameter of the meningovertebral ligaments at each cervical level has been reported (Shi et al., 2014). Since the meningovertebral ligaments are emerging from the ligamentum flavum, the tensile force-displacement curves (Mattucci,

2012) of the ligamentum flavum were scaled based on the area ratio of the meningovertebral ligaments to ligamentum flavum. As a result of this operation, the force-displacement curve for each cervical level meningovertebral ligament was obtained. Mechanical properties of the anterior dural and extraforaminal ligaments have not been characterized so far; thus, response of those ligaments was assumed to be similar to the denticulate ligaments, and the same force-displacement curves were used.

Table 6.1: Neural tissues implemented in the GHBMC M50 Head-Neck model material laws, mesh, material parameters.

Material	Constitutive law	Mesh	Material properties			Reference
Spinal Cord	Hyperelastic (Ogden model) with quasi-linear viscoelasticity	Solid	$\mu = 209$ kPa	$\alpha = 7.52$	$\nu = 0.499$	(Jannesar et al., 2018; Rycman et al., 2021)
			$G_1 = 0.033$	$\beta_1 = 2$ s^{-1}		
			$G_2 = 0.296$	$\beta_2 = 13$ s^{-1}		
			$G_3 = 0.406$	$\beta_3 = 406$ s^{-1}		
Pia mater	Hyperelastic (Ogden Model)	Shell	$\mu = 4.2$ MPa	$\alpha = 12.58$	$\nu = 0.49$	(Jin et al., 2006; Rycman et al., 2021)
CSF	Newtonian fluid	SPH	$K = 2.19$ GPa	$VC = 0.1$		(Richardson and Wissler, 1996)
Dura mater	Orthotropic hyperelastic	Shell	Input stress-strain curves in circumferential and longitudinal direction			(Shetye et al., 2014; Rycman et al., 2022)
Denticulate Ligaments	Hyperelastic spring	Beam elements	Input force-displacement curve for each cervical level from C0 to C7			(Polak et al., 2014)
Meningovertebral Ligaments	Hyperelastic spring	Beam elements	Input force-displacement curve for each cervical level from C0 to C7			(Mattucci, 2012; Shi et al., 2014)

6.2.2 HBM Impact Simulation

The detailed M50 Head-Neck model with the spinal cord, denoted by SC$_{T1}$, and without the spinal cord, denoted by SC$_{C0}$, were assessed against human volunteer impact test cases conducted by the Naval BioDynamics Laboratory (NBDL) (Wismans and Spenny, 1983; Wismans et al., 1986, 1987; Thunnissen et al., 1995). In the experiments, each male subject

was seated and belted using a five-point harness to a rigid seat that was accelerated in frontal, lateral, rear, and oblique directions with severities ranging from 4g to 15g (Figure 6.2). High-speed cameras, accelerometers, and gyroscopes were used to acquire the kinematic quantities of the head center of gravity and 1st thoracic vertebra. Translational and angular velocities of the 1st thoracic vertebra were used as a boundary condition in the simulations of the GHBMC M50 Head-Neck model (Barker and Cronin, 2021).
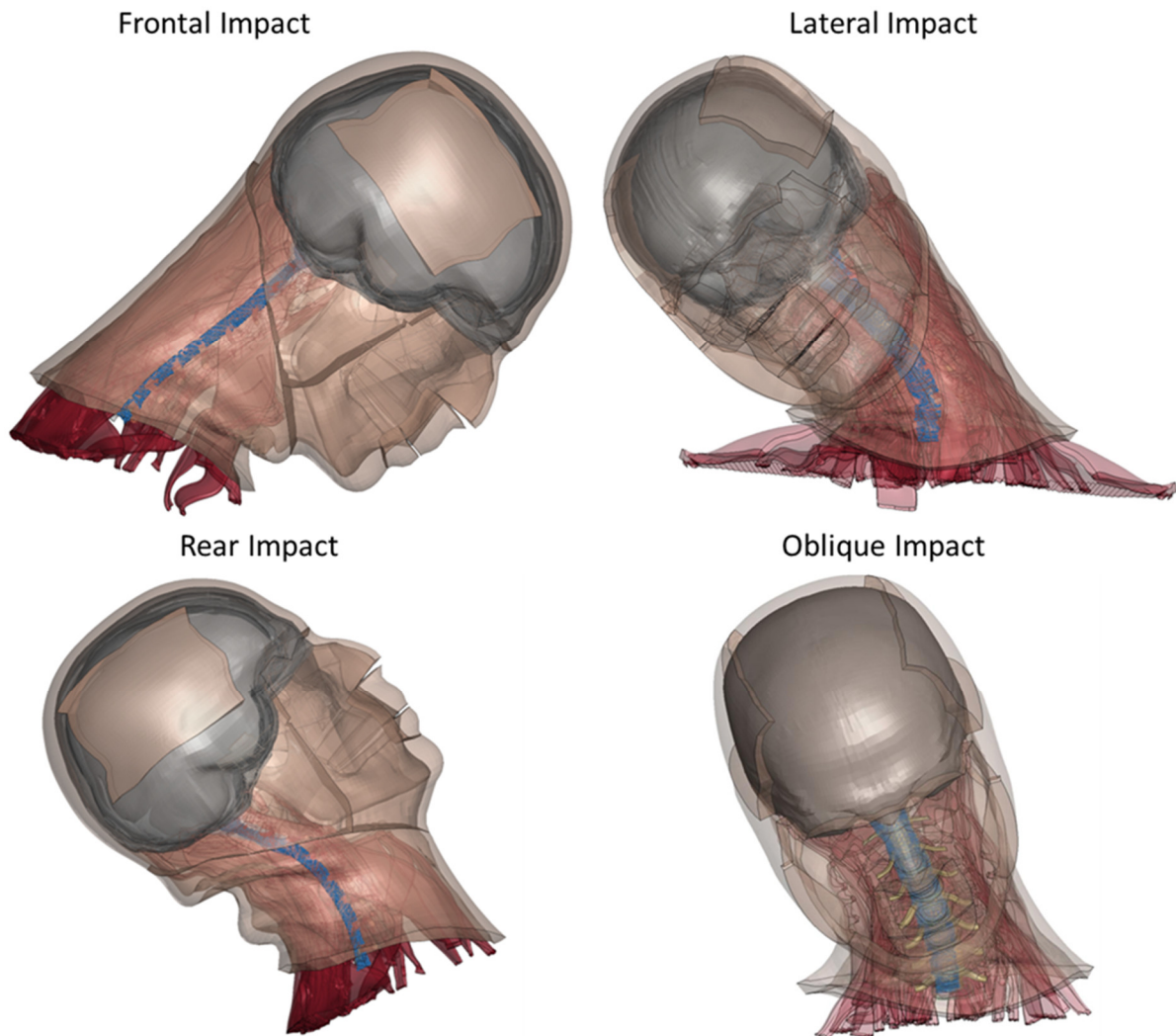
Figure 6.2: NBDL directions used to assess the influence of the spinal cord to the brain tissue.

6.2.3 Quantification of the Neural Tissue Deformation during Head Acceleration

In this chapter, MPS_{95} and a novel cumulative strain-volume curve approach were used as the metrics to evaluate the deformation of the brain and brain stem tissue. Differences between models (with and without the spinal cord) were quantified with a newly proposed volume-weighted average increase in the maximum MPS (VAI_{MPS}).

Firstly, the MPS was computed for each finite element of the neural tissues, throughout the simulation time, and then the maximum 95th percentile value was found (MPS_{95}). Similar to other studies (Rowson and Duma, 2013; Miller et al., 2019), the 95th percentile was used instead of the 100th percentile to filter out heavily distorted elements and better represent the overall deformation of the brain tissue. Then, based on the maximum MPS for each element the cumulative strain-volume distribution curves were plotted. The MPS_{95} and the cumulative strain-volume curves were calculated and plotted for three volumes of interests: the whole brain tissue, brain stem, and spinal cord. Finally, to compare differences between model with the spinal cord (SC_{T1}) with model without the spinal cord (SC_{C0}) the newly proposed VAI_{MPS} were used as the metrics to evaluate the deformation of the brain and brain stem tissue.
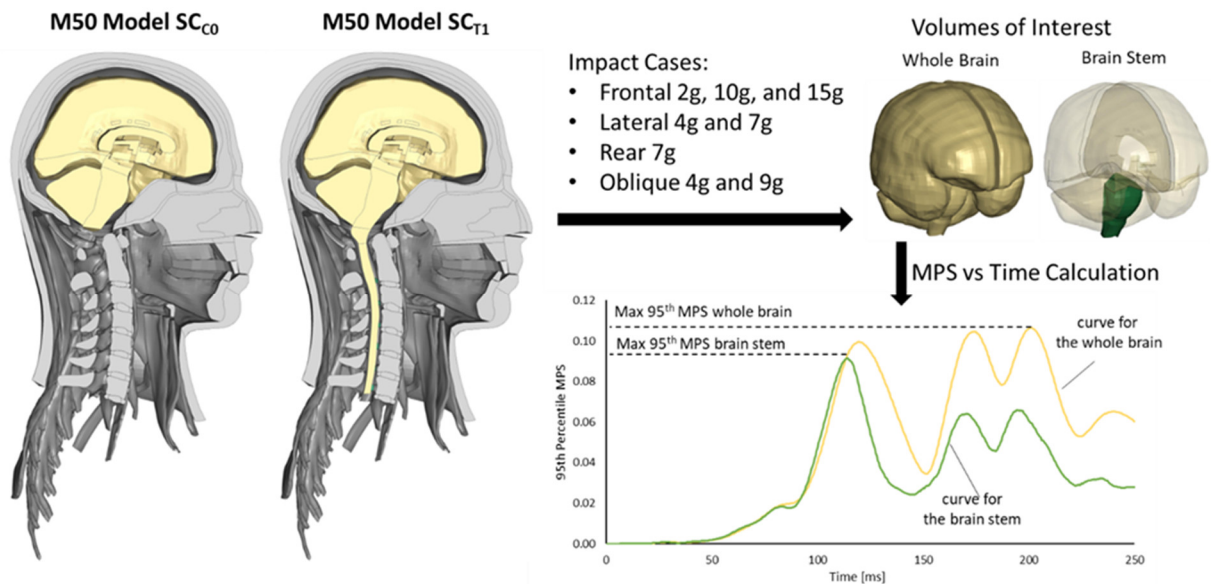
Figure 6.3: Post-processing flow chart of the quantification of the deformation in the whole brain, and in the brain stem tissue, for the M50 Head-Neck model without (SC_{C0}) and with (SC_{T1}) the spinal cord implementation.

The cumulative strain curves were generated as follows. Firstly, for each element initial fraction of volume and maximum MPS were calculated. Then, the elements were listed in order of increasing maximum MPS. Finally, from the initial volume of 100% the fraction of volume of each element was subtracted and cumulative strain curves were plotted for each impact case. The VAI$_{MPS}$ metric was calculated to assess the difference between cumulative strain distribution curves and quantify differences between the models with and without the spinal cord. Firstly, for each element the magnitude of MPS was found and multiplied by the element initial volume $((V_i * |MPS_{iT1}|))$. Next, the sum of this multiplication for all the elements was calculated for both head and neck models (SC$_{C0}$ and SC$_{T1}$). Finally, the ratio between the sums was calculated (Figure 6.4, Equation 6.1). The VAI$_{MPS}$ metric was calculated for two volumes the whole brain tissue (global assessment) and for the brain stem (local assessment) between the models with the implemented spinal cord (SC$_{T1}$) and without (SC$_{C0}$) (Figure 6.4).

$$VAI_{MPS} = \frac{\sum_{i=1}^{N} V_i * |MPS_{iT1}|}{\sum_{i=1}^{N} V_i * |MPS_{iC0}|} - 1 \quad \text{(Equation 6.1)}$$
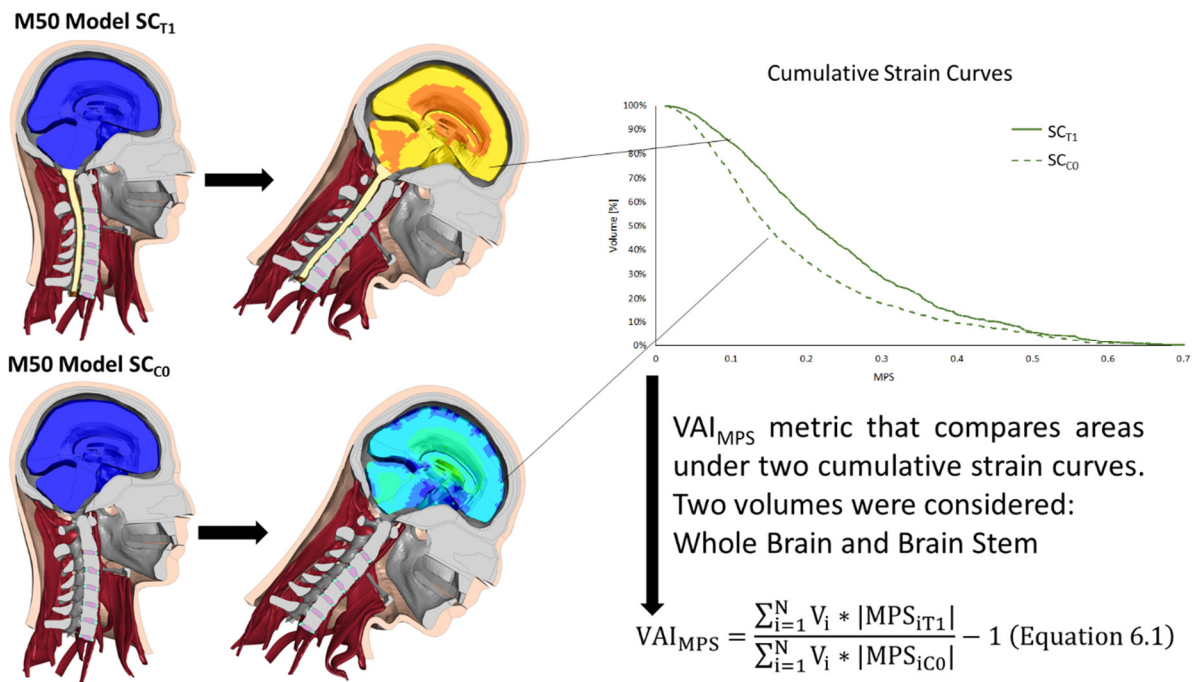
Figure 6.4: Proposed cumulative strain curves and VAI$_{MPS}$ metric to compare tissue deformation between two models. The plot represents the fraction of volume as a function of the sorted maximum MPS for each brain stem element. The VAI$_{MPS}$ was computed for the whole brain and the brain stem region.

All models were solved using a commercial finite element software (LS-DYNA MPP 9.2, single-precision on 32 Intel Xeon E5-2683 2.1 GHz processors). All simulations terminated normally in less than 10 hours of computation time. Data processing was accomplished using a custom-written script to extract the MPS_{95} (Python 3.9) and commercial post-processing software (LS-PrePost v4.7.9).

6.3 Results

6.3.1 NBDL Impact Cases

All the simulated impact cases using GHBMC M50 Head-Neck model ran to completion (250ms). Head kinematics (i.e., linear acceleration and angular displacement) were compared with the reported NBDL data for two simulated models SC_{C0} and SC_{T1}. No difference in the traces of the head center of gravity were observed between the models (Figure 6.5).
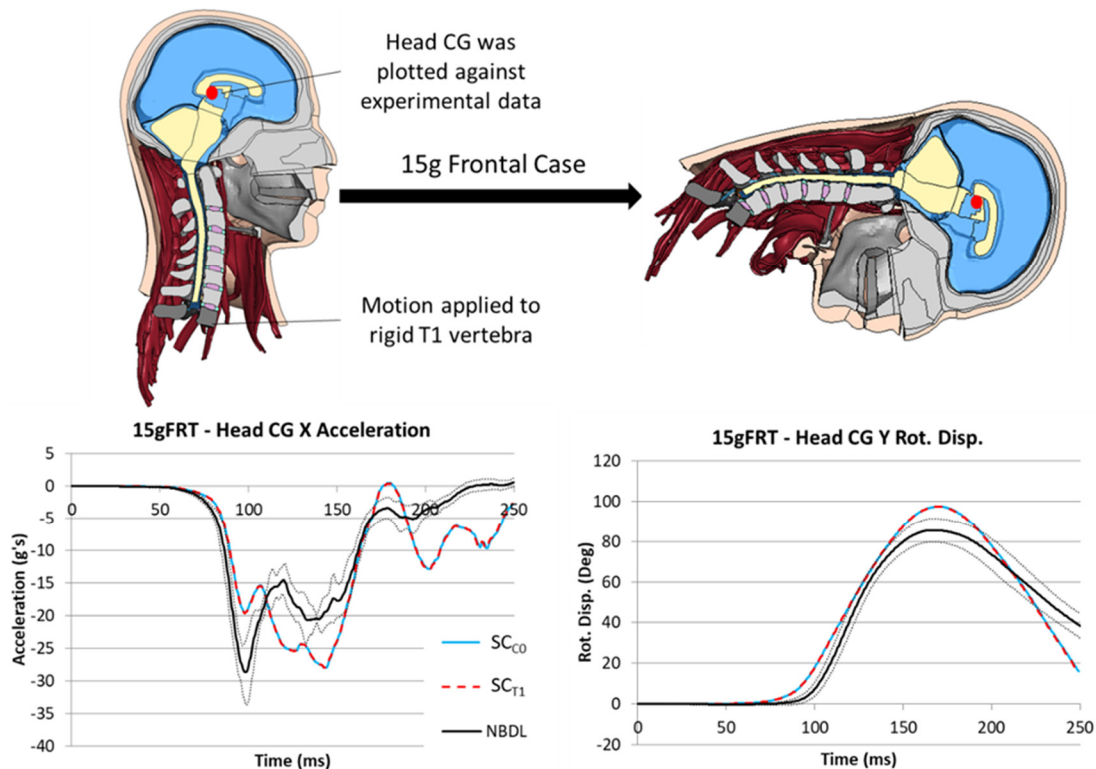
Figure 6.5: Exemplar head center of gravity (CG) kinematics for two models compared to NBDL data. Note that SC_{C0} and SC_{T1} curves are overlapping each other.

89

6.3.2 Brain Tissue Deformation

The FE model with the implemented spinal cord (SC_{T1}) showed marginally higher results of the MPS_{95} of the whole brain tissue (solid green bars) in lateral, rear, oblique compared to the model without spinal cord (SC_{C0}) (Figure 6.6). The biggest difference in the MPS_{95}, when the volume of the whole brain tissue was considered, occurred in the 15g frontal impact case simulation, with a 5.3% increase with the inclusion of the spinal cord.
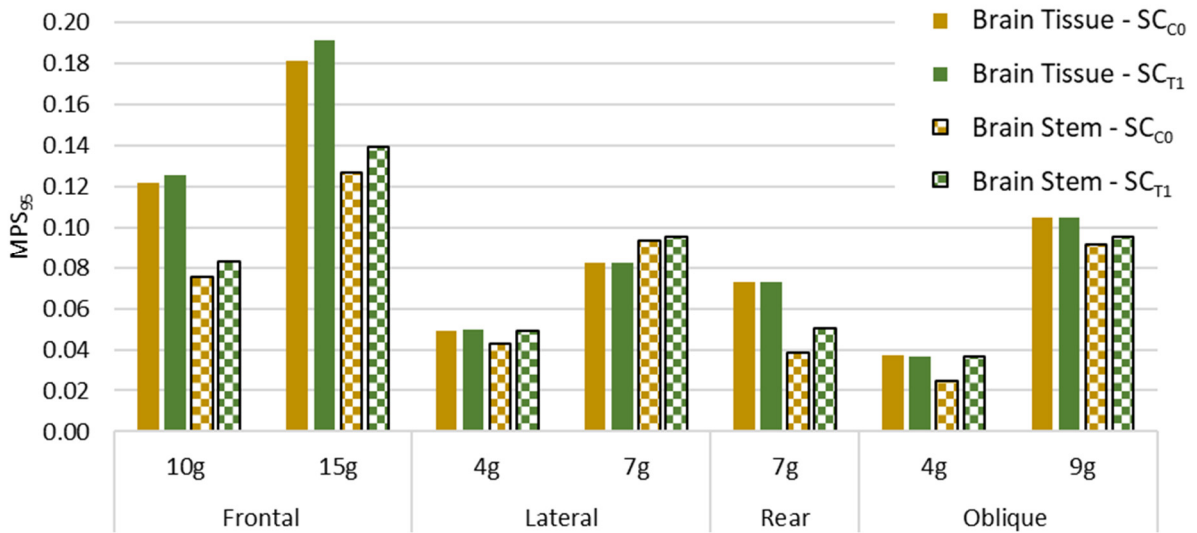
Figure 6.6: The MPS_{95} of the brain tissue (gold bars) and brain stem (green bars) in the model with spinal cord (full bars) and without spinal cord (pattern-filled bars) in different modes of loading and different severities.

The MPS_{95} in the brain stem for the model with implemented spinal cord demonstrated a visible increase throughout all the cases ranging between 2% (Lateral 7g) to 46% (Oblique 4g), with an average increase of 17% (Figure 6.6).

The cumulative strain curves showed that the change is the deformation field is localized in the brain stem. The strain cumulative curves for the whole brain (Figure 6.7) showed progression with increase of the severity of the impact but the differences were small, in opposition to the cumulative strain curves for the brain stem (Figure 6.8).
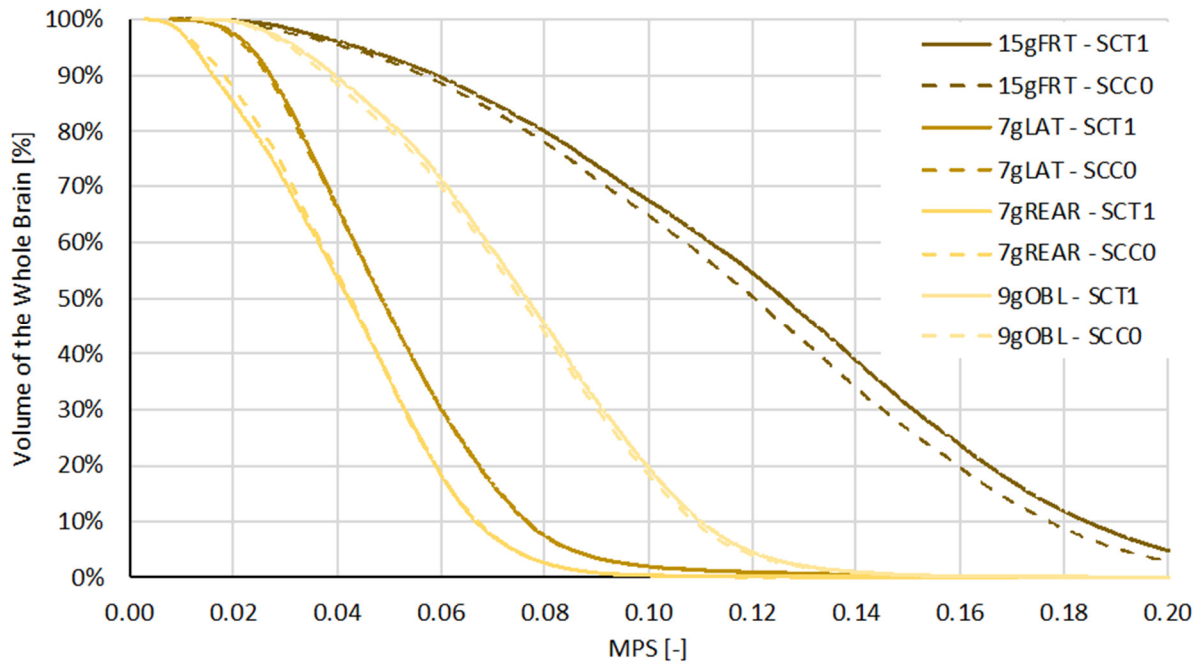
Figure 6.7: Cumulative strain curves for the whole brain.
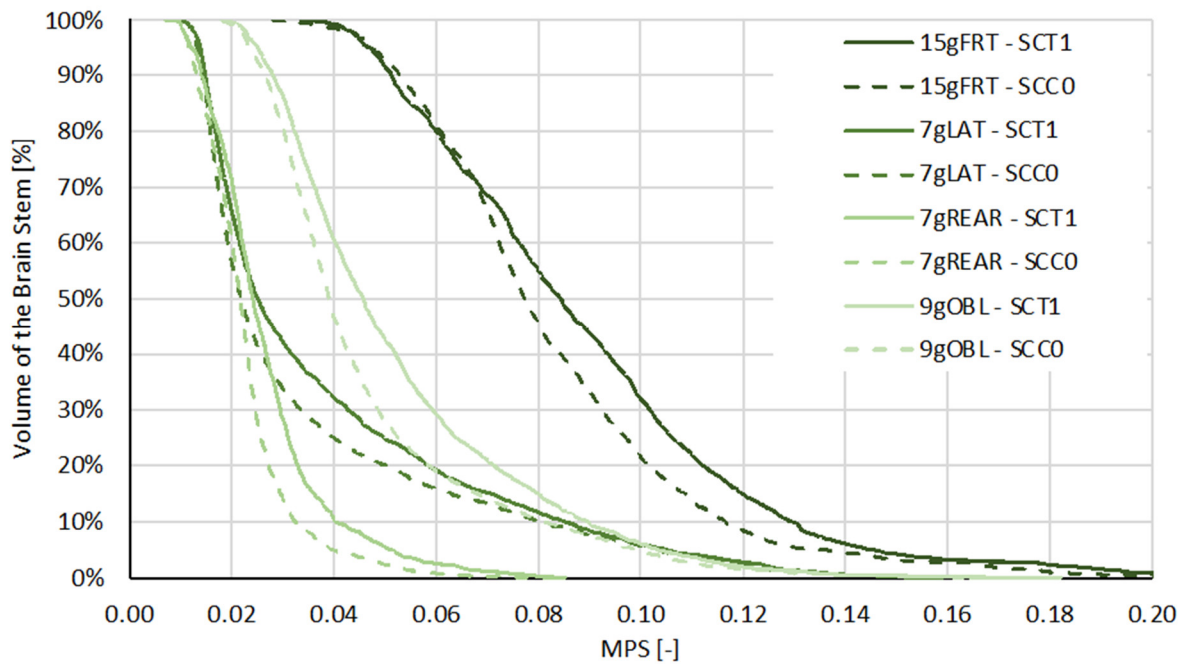
Figure 6.8: Cumulative strain curves for the brain stem.

The developed VAI_{MPS} metric highlights that the average largest increase in the maximum MPS for each element occurs locally in the brain stem up to almost 40% (Oblique 4g) with the implemented spinal cord. The whole brain tissue showed a smaller increase of the VAI_{MPS}, ranging from a 0.18% increase (Rear 7g) to 5.63% (Frontal 15g) (Figure 6.9).
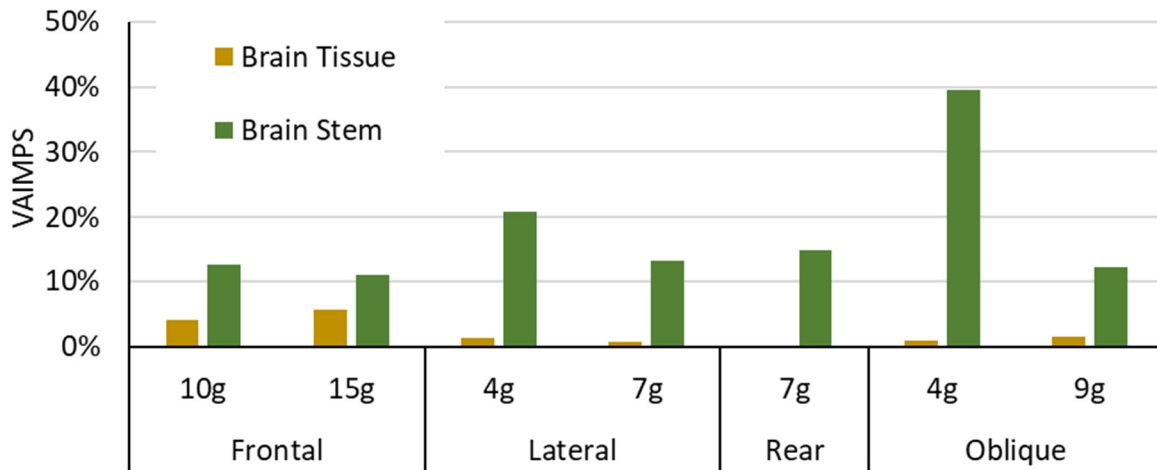
Figure 6.9: Newly developed VAI_{MPS} metric that compares the areas under the cumulative curves separately for the brain tissue and brain stem tissue between the SC_{C0} and SC_{T1} models.

6.3.3 Spinal Cord Tissue Deformation

The deformations in the spinal cord were also quantified using the MPS_{95} metric (Figure 6.10). The MPS_{95} for the spinal cord tissue ranged from 0.1195 (4gLAT) to 0.1980 (15gFRT). The gentle slope of the cumulative strain curves indicated that greater portion of the cervical spinal cord experienced relatively high strains (Figure 6.11).
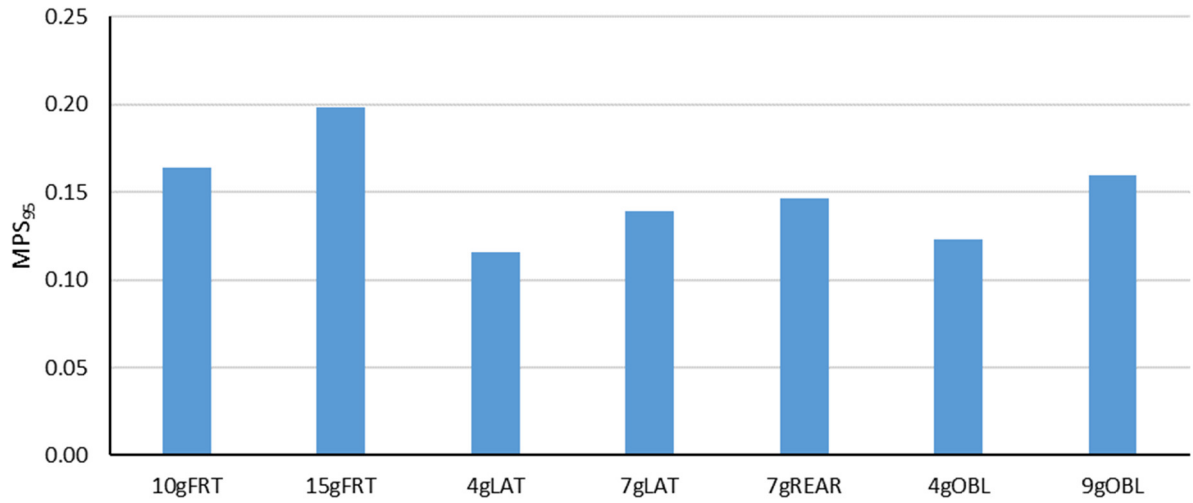
Figure 6.10: MPS$_{95}$ in the spinal cord.
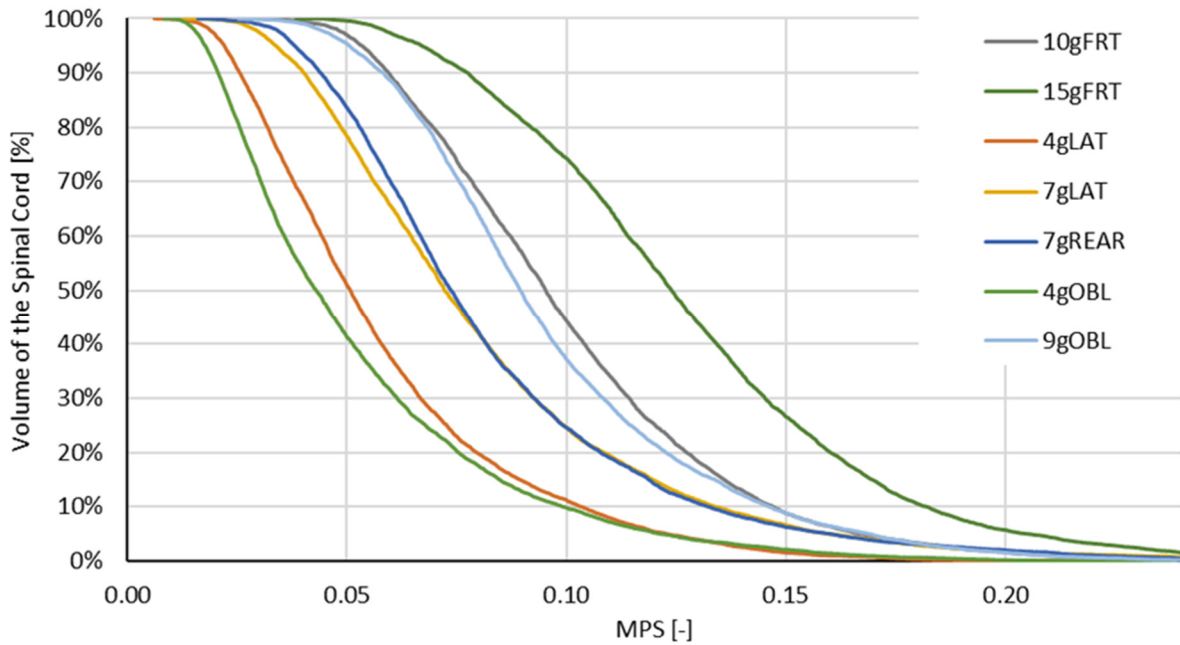
Figure 6.11: Cumulative strain curves for the spinal cord tissue.

6.4 Discussion

In this chapter, into the GHBMC M50 Head-Neck model with implemented spinal cord tissue was simulated in a range of impact conditions across different severities and directions. Further

analysis identified that incorporation of the cervical spinal cord influenced the brain tissue deformations, based on the changes in the MPS_{95}, cumulative strain curves and increase in newly proposed VAI_{MPS} metric.

The material models used to represent cervical neural tissues were previously validated in impact and indentation simulations (Rycman et al., 2021), while the SPH approach representing the CSF layer previously demonstrated biofidelic behaviour of the fluid-structure interaction in simulations of spinal cord impact experiments (Rycman et al., 2022).

Improving the brain stem boundary condition by integrating the spinal cord increased the deformation of the brain in all simulated impact cases, which was quantified by an increase in the MPS_{95}. The increased mass and inertial of the neural tissues in the model with the spinal cord led to increased strains, particularly in the region with the brain stem. During rapid movements of the head, the spinal cord motion led to greater interaction with the local brain tissues, generally leading to an increase in strain in this region.

The NBDL reports did not describe any brain injuries and the maximum MPS_{95} observed with the GHBMC M50 model was 0.1911 for whole-brain tissue with the spinal cord in the 15g frontal impact case. The difference in MPS_{95} compared to the model without the spinal cord (0.1815) may be exacerbated when the model is exercised in a more severe case. The MPS_{95} has been previously used to correlate outcomes of FE models to the concussive head injury; however, there is no consensus on the MPS_{95} threshold values for TBI. Reported threshold values ranged from 0.06 to 0.448, and they were dependent on the FE model used by the studies and specific regions of the brain (Bruneau, 2019).

The MPS_{95} for the spinal cord tissue showed in general higher results than the MPS_{95} results for the brain tissue. However, magnitude value did not exceed 0.20 in any impact case. Surprisingly, even for low severity impact case (4gLAT), the MPS_{95} observed in the spinal cord (0.1159) are high compared to the MPS_{95} values calculated for the brain tissue (0.0498). That might suggest that the cervical spinal cord has higher mobility in the cervical spinal canal and the higher observed strains in the spinal cord are anatomical.

Inherently, MPS_{95} as a metric of TBI is limited to representing the global deformation pattern and may obscure focal deformations occurring in the brain tissue. Further, the MPS_{95} does not quantify the volume of tissue that experiences high strains. Therefore, the MPS_{95} is an objective, single value, and consistent indicator of tissue deformation, but does not inform about the distribution of strains in the tissue; which is addressed by the cumulative strain curve approach. In addition, the developed VAI_{MPS} metric quantified the areal difference between the cumulative strain curves. The VAI_{MPS} slightly increased when the whole brain tissue elements were taken into consideration; however, there were large increases (10% to 40%) when only the brain stem tissue was considered. The higher strains in the brain stem support the idea that the compliance and inertia of the spinal cord results in locally higher deformation in the brain stem region.

The implementation of the spinal cord has several recognized limitations. First, force-displacement curves for the anterior dural and extraforaminal ligaments were approximated with denticulate ligament behaviour. Those ligaments have not yet been characterized in the literature. Secondly, the spinal cord tissue terminates at the first thoracic vertebra with elastic neural ligament attachment to the bony parts of the vertebra. A sensitivity study was conducted to evaluate how the boundary condition applied along the spinal cord influences the brain tissue deformation (Figure 6.12). A sensitivity study was conducted to evaluate the attachment of the spinal cord to the spinal canal and how it influences the brain tissue deformation. The GHBMC M50 Head-Neck model, with the implemented cervical spinal cord tissue (SC_{T1}), was simulated in three styles of attachment: anatomical ($SC_{T1\text{-}Anatomical}$), free ($SC_{T1\text{-}Free}$), and fixed ($SC_{T1\text{-}Fixed}$). The anatomical model contained elastic neural ligaments along the spinal cord. The inferior nodes of the dura mater were attached to the first thoracic vertebra. The free version of the SCT1 model was striped from all the ligaments and the inferior part of the dura mater was not attached to the first thoracic vertebra. The fixed version of the GHBMC M50 Head-Neck model contained all the neural ligaments and additionally the inferior nodes of the dura mater were rigidly connected to the first thoracic vertebra. The MPS_{95} of the whole brain and of the brain stem did not show any sensitivity to presented styles of attachment of the

spinal cord in the spinal canal. Therefore, changes in deformation pattern in the brain tissue between the SC_{T1} and SC_{C0} models cannot be attributed to the attachment style of the cervical spinal cord in the spinal canal.
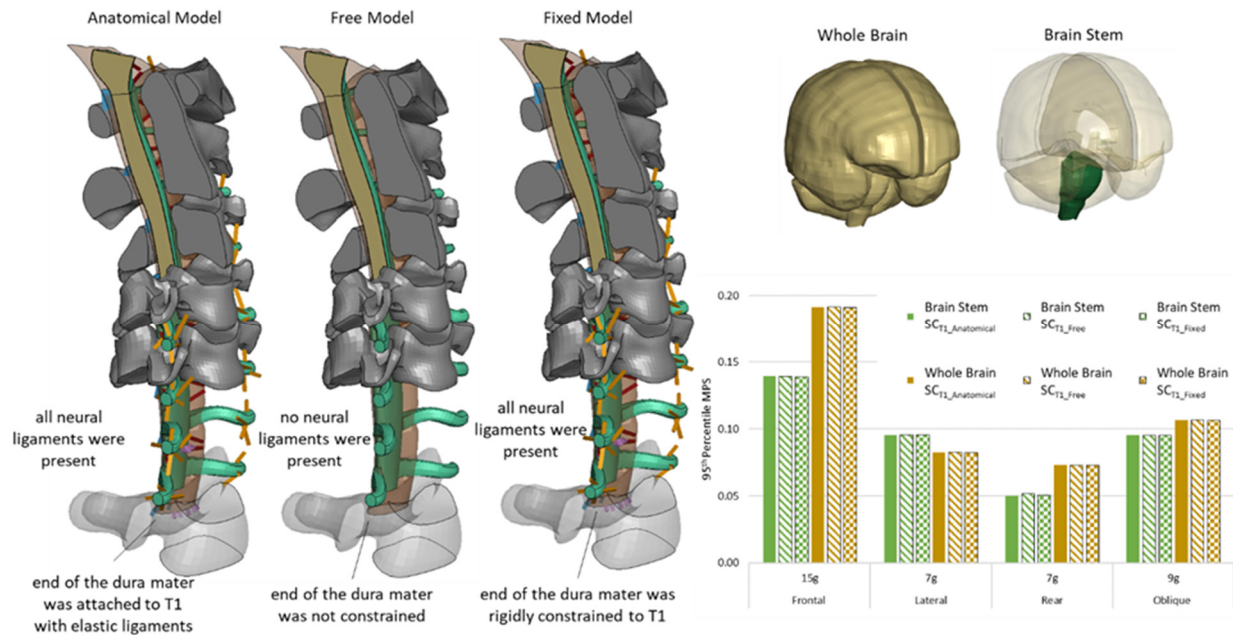
Figure 6.12: Sensitivity study of the attachment style of the spinal cord in the spinal canal and the influence of it on the brain tissue.

The sensitivity study indicated that the boundary condition applied along the spinal cord did not change the deformation pattern observed in the brain and brain stem. Finally, the MPS_{95} metric indicates that in general spinal cord, under the same impact condition, is deformed more than the brain tissue; however, due to the lack of validation data this finding cannot be confirmed.

6.5 Conclusions

Implementation of a spinal cord in the GHBMC M50 Head-Neck model serves two important objectives. Firstly, the inclusion of the spinal cord provides an anatomically correct representation of the connection between the brain stem and spinal cord, which was found to

influence the deformation pattern of the whole brain tissue in all impact cases examined. Further, the developed VAI$_{MPS}$ metric highlighted that the average increase of the MPS in each element occurred in the brain stem. Secondly, the implemented spinal cord provides new capabilities for the HBM to quantify spinal cord deformation and could be used in the future to investigate spinal cord injury. Towards addressing the problem of TBI, results from the current study highlight the importance of incorporating the cervical spinal cord in the HBM and analyzing the complex strain states in a comprehensive manner.

Chapter 7

Summary and Conclusions

This thesis work described the development and analysis of the first validated numerical model of the cervical spinal cord tissues for implementation in a contemporary HBM. Collectively, outcomes from this research contribute to the body of knowledge surrounding spinal cord impact mechanics and further opens the door to investigations of spinal cord injuries and nerve roots impingement using full HBM in desired impact scenarios. A key strength of this research lies in the hierarchical validation of the implemented tissues, with previous literature showing limited validation for the current FE spinal cord models. Moreover, the literature review identified relevant tissues from the biomechanical perspective of view, inter alia spinal cord, pia mater, dura mater, CSF and neural ligaments, which were each numerically designed and implemented in the HBM. Importantly, the presence of the spinal cord in the HBM provided more anatomically correct boundary condition for the brain stem and demonstrated an important contribution to the response of the brain tissue strains during impact. A brief summary of the key methodology and findings from each Chapter follows.

In Chapter 3, the model development process was initiated by fitting and validating material models of the spinal cord tissues. A robust and easy-to-apply fitting methodology, even for complex modes of loading, was proposed and utilized. The validation process was achieved by recreating two different experimental setups, spinal cord indentation and impact tests, that considered rapid transverse deformation of the spinal cord-pia mater complex. The impact model correctly predicted the impactor loading and displacement magnitude on the spinal cord-pia mater specimen, whereas the indentation simulation matched the experimental data up to 60% of the transverse compression. The mechanics of the pia mater were examined, and it was found that pia mater provided confining effects to the spinal cord and limits the transverse compression regardless of its thickness.

In Chapter 4, an efficient numerical implementation and the role of the CSF were investigated. Four numerical methods: SPH, ALE, Lagrange and PV were tested to model fluid-structure

interaction in the recreated transverse impact experiment on the spinal cord-pia mater-CSF-dura mater specimen. The ALE method provided an excellent match to the experimental data, however; it was the most computationally expensive. The SPH method provided a very good correlation between the simulation and experimental data in a fraction of the ALE computational time. Thus, the SPH method was implemented in the HBM.

In Chapter 5, the development of the representative geometries for the cervical spinal cord tissues were based on an MRI dataset augmented with available literature data. Achieved geometries of the spinal cord were compared to literature data. The measured dimensions of the spinal cord cross-sectional width, depth and area felt within the reported literature data. The developed geometries were meshed using a commercial preprocessor, meeting rigorous quality mesh standards. The meshing process proceeded with the implementation of the developed meshes into the detailed GHBMC 50th percentile M50 head and neck model.

In Chapter 6, stability of the models was assessed using NBLD impact test cases in multiple directions and severities. The models were stable and no change in the gross kinematics of the head center of gravity were observed after implementation of the spinal cord tissue. Importantly, analysis showed that the implementation of the spinal cord tissue indeed changed the deformation pattern in the brain tissue. The implementation of the spinal cord influenced the strain fields in the brain stem. The changes in strains between the model with and without the spinal cord were assessed using the tissue level metric (i.e., maximum 95th percentile MPS). Additionally, a novel FE cumulative strain metric was proposed to quantify the average increase of MPS in each element. This study showed that the implementation of the spinal cord not only expanded the GHBMC M50 model capabilities in predicting the SCI but also enhanced the prediction of the deformation in the brain tissue.

7.1 Future Work

The proposed model of the spinal cord tissue has some recognized limitations. Currently, the average mesh size of 1 mm, necessary for computational efficiency, prohibits the separation of the white and gray matter in the spinal cord. Secondly, more tissue-level experimental data

is needed to quantify any differences between cervical white and gray matter. Further, the current constitutive model representing the spinal cord was fitted considering only compressive data of the spinal cord white matter. Mechanical data for the spinal cord in multiple modes of loading (e.g., tension, shear) is needed to verify and improve the constitutive model parameters. Further, the thoracic, lumbar, sacral and coccyx segments of the spinal cord should be implemented in the HBM.

As a next step it would be necessary to obtain the mechanical properties of human tissues for varying age and sex. The developed FE model utilized the mechanical properties from animal testing including bovine, porcine, non-human primate and ovine test data. The questions regarding sex and age differences in mechanical properties of the cervical neural tissues remain unanswered. Importantly, the fitted material properties for the spinal cord, pia mater, dura mater, neural ligaments and numerical representation of the CSF developed in the current study can be directly implemented in child and female FE models.

7.2 Novelty and Significance of the Research

The novelty and significance of the developed numerical models of the cervical spinal cord tissues for the field of impact biomechanics can be recognized as follows:

1. New and optimized Ogden model material parameters with quasi-linear viscoelastic parameters were identified for the spinal cord tissue.

2. General and universal material model fitting methodology was developed, and the use was proved by fitting complex experimental data into the constitutive model. In the future the developed method can be applied to other modes of loading

3. The role of the pia mater during dynamic impact was quantified for the first time, including a sensitivity study of the pia mater thickness.

4. Investigation of the CSF implementation using four numerical approaches was undertaken, with a novel approach considered for the cervical CSF using SPH elements for fluid-structure interaction.

5. The potential of a contemporary HBM to assess spinal cord response at the tissue level over a range of impact severities was enabled by the development and successful integration of the spinal cord into the GHBMC M50 model.

6. The influence of the implementation of the cervical spinal cord model on brain tissue deformation in a head and neck HBM was assessed over a range of non-injurious impact severities and directions, demonstrating the key role of the anatomical boundary conditions between the brain and spinal cord.

Ultimately, these thesis contributions add meaningful technical and scientific knowledge to the field of spinal cord impact mechanics and are important steps towards addressing the societal burden of SCI.

Letters of Copyright Permission

JOHN WILEY AND SONS LICENSE
TERMS AND CONDITIONS

Jul 07, 2022

This Agreement between Mr. Aleksander Rycman ("You") and John Wiley and Sons ("John Wiley and Sons") consists of your license details and the terms and conditions provided by John Wiley and Sons and Copyright Clearance Center.

License Number	5296171380518
License date	Apr 25, 2022
Licensed Content Publisher	John Wiley and Sons
Licensed Content Publication	INTERNATIONAL JOURNAL FOR NUMERICAL METHODS IN BIOMEDICAL ENGINEERING
Licensed Content Title	Comparison of numerical methods for cerebrospinal fluid representation and fluid–structure interaction during transverse impact of a finite element spinal cord model
Licensed Content Author	Aleksander Rycman, Stewart McLachlin, Duane S. Cronin
Licensed Content Date	Jan 17, 2022
Licensed Content Volume	38
Licensed Content Issue	3

102

Licensed Content Pages	14

Type of use	Dissertation/Thesis

Requestor type	Author of this Wiley article

Format	Print and electronic

Portion	Full article

Will you be translating?	No

Title	Computational Modeling of the Cervical Spinal Cord: Investigation of Impact Response and Injury Risk

Institution name	University of Waterloo

Expected presentation date	Aug 2022

Requestor Location	Mr. Aleksander Rycman Attn: Mr. Aleksander Rycman

Publisher Tax ID	EU826007151

Total	0.00 USD

Terms and Conditions

Bibliography

Anderson, R. (2004). Finite Element Modelling of Impact-induced Axonal Injury in Sheep. *Int. Neurotrauma Symp.*, 1–7.

Anderson, T. E. (1985). Spinal cord contusion injury: Experimental dissociation of hemorrhagic necrosis and subacute loss of axonal conduction. *J. Neurosurg.* 62, 115–119. doi:10.3171/jns.1985.62.1.0115.

Antona-Makoshi, J. (2016). Traumatic Brain Injuries: Animal Experiments and Numerical Simulations to Support the Development of a Brain Injury Criterion. Available at: http://publications.lib.chalmers.se/records/fulltext/235126/235126.pdf%0Ahttps://trid.trb.org/view/1463190.

Antona-Makoshi, J., Davidsson, J., Ejima, S., and Ono, K. (2016). Development of a comprehensive injury criterion for moderate and mild traumatic brain injuries. *Int. J. Automot. Eng.* 7, 69–75. doi:10.20485/jsaeijae.7.2_69.

Antona-Makoshi, J., Davidsson, J., Risling, M., Susumu, E., and Ono, K. (2014). Validation of Local Brain Kinematics of a Novel Rat Brain Finite Element Model under Rotational Acceleration. *Int. J. Automot. Eng.* 5, 20144188. doi:10.20485/jsaeijae.5.1_31.

Antona-Makoshi, J., Eliasson, E., Davidsson, J., Ejima, S., and Ono, K. (2015). Effect of Aging on Brain Injury Prediction in Rotational Head Trauma—A Parameter Study with a Rat Finite Element Model. *Traffic Inj. Prev.* 16, S91–S99. doi:10.1080/15389588.2015.1021416.

ASME (2018). Assessing Credibility of Computational Modeling through Verification and Validation: Application to Medical Devices. 60.

Barker, J. B., and Cronin, D. S. (2021). Multilevel Validation of a Male Neck Finite Element Model With Active Musculature. *J. Biomech. Eng.* 143. doi:10.1115/1.4047866.

Barker, J. B., Cronin, D. S., and Nightingale, R. W. (2017). Lower Cervical Spine Motion Segment Computational Model Validation: Kinematic and Kinetic Response for Quasi-Static and Dynamic Loading. *J. Biomech. Eng.* 139, 061009. doi:10.1115/1.4036464.

Bartz, J. A. (1972). Development and Validation of a Computer Simulation of a Crash Victim in Three Dimensions. in doi:10.4271/720961.

Baudrit, P., Hamon, J., Song, E., Robin, S., and Le Coz, J.-Y. (1999). Comparative Studies of Dummy and Human Body Models Behavior in Frontal and Lateral Impact Conditions. in doi:10.4271/99SC05.

Beillas, P., Giordano, C., Alvarez, V., Li, X., Ying, X., Chevalier, M., et al. (2018). Development and performance of the PIPER scalable child human body models To cite this version : HAL Id : hal-01720414 Development and performance of the PIPER

scalable child human body models.

Bilston, L. E. (1998). Finite Element Analysus of Some Cervical Spinal Cord Injury Modes. *IRCOBI Conf. Proc.*, 365–376.

Bilston, L. E. (2011). *Neural Tissue Biomechanics.* , ed. L. E. Bilston Berlin, Heidelberg: Springer Berlin Heidelberg doi:10.1007/978-3-642-13890-4.

Bilston, L., and Thibault, L. (1995). The mechanical properties of the human cervical spinal cordIn Vitro. *Ann. Biomed. Eng.* 24, 67–74. doi:10.1007/BF02770996.

Borrvall, T., Ehle, C., and Stratton, T. (2015). A Fabric Material Model with Stress Map Functionality in LS-DYNA. in *10th European LS-DYNA Conference* (Würzburg, Germany).

Bostrom, O., Motozawa, Y., Oda, S., Ito, Y. I., and Mroz, K. (2003). Mechanism of reducing thoracic deflections and rib strains using supplemental shoulder belt during frontal impacts. *Proc 23th Int. Tech. Conf. Enhanc. Saf. Veh. Pap.*, 1–5.

Bruneau, D. (2019). Investigation of Head and Brain Response in Football Helmet Impacts using a Finite Element Model of the Head and Neck with Active Muscle by.

Bruneau, D. A., and Cronin, D. S. (2021). Brain response of a computational head model for prescribed skull kinematics and simulated football helmet impact boundary conditions. *J. Mech. Behav. Biomed. Mater.* 115, 104299. doi:10.1016/j.jmbbm.2020.104299.

Brydon, H. L., Hayward, R., Harkness, W., and Bayston, R. (1995). Physical properties of cerebrospinal fluid of relevance to shunt function. 1: The effect of protein upon CSF viscosity. *Br. J. Neurosurg.* 9, 639–644. doi:10.1080/02688699550040927.

Bustamante, M. C., and Cronin, D. S. (2019). Cavitation threshold evaluation of porcine cerebrospinal fluid using a Polymeric Split Hopkinson Pressure Bar-Confinement chamber apparatus. *J. Mech. Behav. Biomed. Mater.* 100, 103400. doi:10.1016/j.jmbbm.2019.103400.

Cao, Y., Chen, Y., and DeVivo, M. J. (2011). Lifetime direct costs after spinal cord injury. *Top. Spinal Cord Inj. Rehabil.* 16, 10–16. doi:10.1310/sci1604-10.

Centers for Disease Control and Prevention (2019). Surveillance Report of Traumatic Brain Injury-related Emergency Department Visits, Hospitalizations, and Deaths-United States, 2014. *Centers Dis. Control Prev. U.S. Dep. Heal. Hum. Serv.*, 24. Available at: www.cdc.gov/TraumaticBrainInjury.

Ceylan, D., Tatarli, N., Abdullaev, T., Seker, A., Yildiz, S. D., Keles, E., et al. (2012). The denticulate ligament: Anatomical properties, functional and clinical significance. *Acta Neurochir. (Wien).* 154, 1229–1234. doi:10.1007/s00701-012-1361-x.

Chafi, M. S., Dirisala, V., Karami, G., and Ziejewski, M. (2009). A finite element method

parametric study of the dynamic response of the human brain with different cerebrospinal fluid constitutive properties. *Proc. Inst. Mech. Eng. Part H J. Eng. Med.* 223, 1003–1019. doi:10.1243/09544119JEIM631.

Chang, G.-L., Hung, T.-K., and Feng, W. W. (1988). An in-vivo measurement and analysis of viscoelstic properties of the spinal cord of cats. *J. Biomech. Eng.* 110, 155–122.

Chen, R., Shi, B., Zheng, X., Zhou, Z., Jin, A., Ding, Z., et al. (2015). Anatomic study and clinical significance of the dorsal meningovertebral ligaments of the thoracic dura mater. *Spine (Phila. Pa. 1976).* 40, 692–698. doi:10.1097/BRS.0000000000000860.

Clarke, E. C., Cheng, S., and Bilston, L. E. (2009). The mechanical properties of neonatal rat spinal cord in vitro, and comparisons with adult. *J. Biomech.* 42, 1397–1402. doi:10.1016/j.jbiomech.2009.04.008.

Cronin, D. S. (2011). Explicit Finite Element Method Applied to Impact Biomechanics Problems. *IRCOBI Conf. Proc.*, 240–254.

Czyz, M., Ścigała, K., Bedziński, R., and Jarmundowicz, W. (2012). Finite element modelling of the cervical spinal cord injury-clinical assessment. *Acta Bioeng. Biomech.* 14, 23–29. doi:10.5277/abb120403.

Czyz, M., Ścigala, K., Jarmundowicz, W., and Bedzinski, R. (2011). Numerical model of the human cervical spinal cord–the development and validation. *Acta Bioeng. Biomech.* 13, 51–58. Available at: http://www.actabio.pwr.wroc.pl/Vol13No4/6.pdf.

Deck, C., and Willinger, R. (2008). Improved head injury criteria based on head FE model. *Int. J. Crashworthiness* 13, 667–678. doi:10.1080/13588260802411523.

Deng, Y. C. (1992). Development of a submarining model in the CAL3D program. *SAE Tech. Pap.* doi:10.4271/922530.

DeVivo, M. J. (1997). Causes and costs of spinal cord injury in the United States. *Spinal cord Off. J. Int. Med. Soc. Paraplegia* 35, 809–813. doi:10.1097/00005392-199812010-00135.

Diotalevi, L., Bailly, N., Wagnac, É., Mac-Thiong, J. M., Goulet, J., and Petit, Y. (2020). Dynamics of spinal cord compression with different patterns of thoracolumbar burst fractures: Numerical simulations using finite element modelling. *Clin. Biomech.* 72, 186–194. doi:10.1016/j.clinbiomech.2019.12.023.

Duckworth, H., Sharp, D. J., and Ghajari, M. (2021). Smoothed particle hydrodynamic modelling of the cerebrospinal fluid for brain biomechanics: Accuracy and stability. *Int. j. numer. method. biomed. eng.* 37, 1–17. doi:10.1002/cnm.3440.

Dumont, R. J., Okonkwo, D. O., Verma, S., Hurlbert, R. J., Boulos, P. T., Ellegala, D. B., et al. (2001). Acute spinal cord injury, part I: Pathophysiologic mechanisms. *Clin. Neuropharmacol.* 24, 254–264. doi:10.1097/00002826-200109000-00002.

Ellis, R. W., Strauss, L. C., Wiley, J. M., Killmond, T. M., and Ellis, R. W. (1992). A simple method of estimating cerebrospinal fluid pressure during lumbar puncture. *Pediatrics* 89, 895–897.

Fahlstedt, M., Abayazid, F., Panzer, M. B., Trotta, A., Zhao, W., Ghajari, M., et al. (2021). Ranking and Rating Bicycle Helmet Safety Performance in Oblique Impacts Using Eight Different Brain Injury Models. *Ann. Biomed. Eng.* 49, 1097–1109. doi:10.1007/s10439-020-02703-w.

Fahlstedt, M., Meng, S., and Kleiven, S. (2022). Influence of strain Post-Processing on brain injury prediction. *J. Biomech.* 132, 110940. doi:10.1016/j.jbiomech.2021.110940.

Fernandes, F. A. O., Tchepel, D., Alves de Sousa, R. J., and Ptak, M. (2018). Development and validation of a new finite element human head model: Yet another head model (YEAHM). *Eng. Comput. (Swansea, Wales)* 35, 477–496. doi:10.1108/EC-09-2016-0321.

Fiford, R. J., and Bilston, L. E. (2005). The mechanical properties of rat spinal cord in vitro. *J. Biomech.* 38, 1509–1515. doi:10.1016/j.jbiomech.2004.07.009.

Fountas, K. N., Kapsalaki, E. Z., Jackson, J., Vogel, R. L., and Robinson, J. S. (1998). Cervical Spinal Cord-Smaller Than Considered? *Spine (Phila. Pa. 1976).* 23, 1513–1516. doi:10.1097/00007632-199807150-00001.

Fradet, L., Cliche, F., Petit, Y., Mac-Thiong, J. M., and Arnoux, P. J. (2016). Strain rate dependent behavior of the porcine spinal cord under transverse dynamic compression. *Proc. Inst. Mech. Eng. Part H J. Eng. Med.* 230, 858–866. doi:10.1177/0954411916655373.

Fung, Y.-C. (1993). *Biomechanics*. New York, NY: Springer New York doi:10.1007/978-1-4757-2257-4.

Fung, Y. C. (1981). Biomechanics: Mechanical Properties of Living Tissues. *J. Biomech. Eng.* 103, 231–298. doi:10.1115/1.3138285.

Galford, J. E., and McElhaney, J. H. (1970). A viscoelastic study of scalp, brain, and dura. *J. Biomech.* 3, 211–221. doi:10.1016/0021-9290(70)90007-2.

Galle, B., Ouyang, H., Shi, R., and Nauman, E. (2010). A transversely isotropic constitutive model of excised guinea pig spinal cord white matter. *J. Biomech.* 43, 2839–2843. doi:10.1016/j.jbiomech.2010.06.014.

Gayzik, F. S., Moreno, D. P., Geer, C. P., Wuertzer, S. D., Martin, R. S., and Stitzel, J. D. (2011a). Development of a full body CAD dataset for computational modeling: A multi-modality approach. *Ann. Biomed. Eng.* 39, 2568–2583. doi:10.1007/s10439-011-0359-5.

Gayzik, S., Moreno, D., Vavalle, N., Rhyne, A., and Stitzel, J. (2011b). Development of the Global Human Body Models Consortium mid-sized male full body model. *Inj. Biomech.*

Res., 39–12.

Gehre, C., Gades, H., and Wernicke, P. (2009). Objective Rating of Signals Using Test and Simulation Responses. *Int. Tech. Conf. Enhanc. Saf. Veh.*, 1–8. doi:09-0407.

Giordano, C., and Kleiven, S. (2014). Evaluation of Axonal Strain as a Predictor for Mild Traumatic Brain Injuries Using Finite Element Modeling. *SAE Tech. Pap.* 2014-Novem. doi:10.4271/2014-22-0002.

Giudice, J. S., Zeng, W., Wu, T., Alshareef, A., Shedd, D. F., and Panzer, M. B. (2019). An Analytical Review of the Numerical Methods used for Finite Element Modeling of Traumatic Brain Injury. *Ann. Biomed. Eng.* 47, 1855–1872. doi:10.1007/s10439-018-02161-5.

Greaves, C. Y., Gadala, M. S., and Oxland, T. R. (2008). A three-dimensional finite element model of the cervical spine with spinal cord: An investigation of three injury mechanisms. *Ann. Biomed. Eng.* 36, 396–405. doi:10.1007/s10439-008-9440-0.

Guilcher, S. J. T., Munce, S. E. P., Couris, C. M., Fung, K., Craven, B. C., Verrier, M., et al. (2010). Health care utilization in non-traumatic and traumatic spinal cord injury: A population-based study. *Spinal Cord* 48, 45–50. doi:10.1038/sc.2009.78.

Hall, R. M., Oakland, R. J., Wilcox, R. K., and Barton, D. C. (2006). Spinal cord-fragment interactions following burst fracture: an in vitro model. *J. Neurosurg. Spine* 5, 243–50. doi:10.3171/spi.2006.5.3.243.

Hallquist, J. . (2006). *LS-DYNA® Theory Manual*.

Happee, R., Hoofman, M., Van Den Kroonenberg, A. J., Morsink, P., and Wismans, J. (1998). A mathematical human body model for frontal and rearward seated automotive impact loading. *SAE Tech. Pap.* doi:10.4271/983150.

Hartlieb, M., Mayer, C., Richert, J., Ozturk, A., Mayer, F., Pal, S., et al. (2015). Implementation of New Rib Material Models to a FE-Human Body Model for Evaluation of the Pre-Safe Impulse Side Restraint System for Side Impact Protection. *24th Int. Tech. Conf. Enhanc. Saf. Veh.*, 1–10.

Henao, J., Labelle, H., Arnoux, P. J., and Aubin, C. É. (2018). Biomechanical Simulation of Stresses and Strains Exerted on the Spinal Cord and Nerves During Scoliosis Correction Maneuvers. *Spine Deform.* 6, 12–19. doi:10.1016/j.jspd.2017.04.008.

Hernandez, F., Wu, L. C., Yip, M. C., Laksari, K., Hoffman, A. R., Lopez, J. R., et al. (2015). Six Degree-of-Freedom Measurements of Human Mild Traumatic Brain Injury. *Ann. Biomed. Eng.* 43, 1918–1934. doi:10.1007/s10439-014-1212-4.

Hong, J. Y., Suh, S. W., Park, S. Y., Modi, H. N., Rhyu, I. J., Kwon, S., et al. (2011). Analysis of dural sac thickness in human spine - Cadaver study with confocal infrared laser microscope. *Spine J.* 11, 1121–1127. doi:10.1016/j.spinee.2011.11.001.

Horgan, T. J., and Gilchrist, M. D. (2003). The creation of three-dimensional finite element models for simulating head impact biomechanics. *Int. J. Crashworthiness* 8, 353–366. doi:10.1533/ijcr.2003.0243.

Hung, T.-K., and Chang, G.-L. (1981). Biomechanical and neurological resoponse of the spinal cord of a puppy to uniaxial tension. *J. Biomech. Eng.* 103.

Hung, T. K., Chang, G. L., Lin, H. S., Walter, F. R., and Bunegin, L. (1981). Stress-strain relationship of the spinal cord of anesthetized cats. *J. Biomech.* 14, 269–276. doi:10.1016/0021-9290(81)90072-5.

Hung, T. K., Lin, H. S., Bunegin, L., and Albin, M. S. (1982). Mechanical and neurological response of cat spinal cord under static loading. *Surg. Neurol.* 17, 213–217. doi:10.1016/0090-3019(82)90284-1.

Ichihara, K., Taguchi, T., Shimada, Y., Sakuramoto, I., Kawano, S., and Kawai, S. (2001). Gray Matter of the Bovine Cervical Spinal Cord is Mechanically More Rigid and Fragile than the White Matter. *J. Neurotrauma* 18, 361–367. doi:10.1089/08977150151071053.

Ivancic, P. C., Pearson, A. M., Tominaga, Y., Simpson, A. K., Yue, J. J., and Panjabi, M. M. (2007). Mechanism of cervical spinal cord injury during bilateral facet dislocation. *Spine (Phila. Pa. 1976).* 32, 2467–2473. doi:10.1097/BRS.0b013e3181573b67.

Iwamoto, M., Nakahira, Y., and Kimpara, H. (2015). Development and Validation of the Total HUman Model for Safety (THUMS) Toward Further Understanding of Occupant Injury Mechanisms in Precrash and During Crash. *Traffic Inj. Prev.* 16, S36–S48. doi:10.1080/15389588.2015.1015000.

James, S. L., Bannick, M. S., Montjoy-Venning, W. C., Lucchesi, L. R., Dandona, L., Dandona, R., et al. (2019). Global, regional, and national burden of traumatic brain injury and spinal cord injury, 1990-2016: A systematic analysis for the Global Burden of Disease Study 2016. *Lancet Neurol.* 18, 56–87. doi:10.1016/S1474-4422(18)30415-0.

Jannesar, S., Allen, M., Mills, S., Gibbons, A., Bresnahan, J. C., Salegio, E. A., et al. (2018). Compressive mechanical characterization of non-human primate spinal cord white matter. *Acta Biomater.* 74, 260–269. doi:10.1016/j.actbio.2018.05.002.

Jannesar, S., Nadler, B., and Sparrey, C. J. (2016). The Transverse Isotropy of Spinal Cord White Matter Under Dynamic Load. *J. Biomech. Eng.* 138, 091004. doi:10.1115/1.4034171.

Jannesar, S., Salegio, E. A., Beattie, M. S., Bresnahan, J. C., and Sparrey, C. J. (2020). Correlating Tissue Mechanics and Spinal Cord Injury: Patient-Specific Finite Element Models of Unilateral Cervical Contusion Spinal Cord Injury in Non-Human Primates. *J. Neurotrauma*. doi:10.1089/neu.2019.6840.

Jin, X. (2009). Biomechanical Response and Constitutive Modeling of Bovine Pia-Archnoid

Complex.

Jin, X., Lee, J. B., Leung, L. Y., Zhang, L., Yang, K. H., and King, A. I. (2006). Biomechanical Response of the Bovine Pia-Arachnoid Complex to Tensile Loading at Varying Strain Rates. in *SAE Technical Papers*, 637–649. doi:10.4271/2006-22-0025.

Jin, X., Yang, K. H., and King, A. I. (2011). Mechanical properties of bovine pia-arachnoid complex in shear. *J. Biomech.* 44, 467–474. doi:10.1016/j.jbiomech.2010.09.035.

Jones, C. F., and Clarke, E. C. (2018). Engineering approaches to understanding mechanisms of spinal column injury leading to spinal cord injury. *Clin. Biomech.*, 1–13. doi:10.1016/j.clinbiomech.2018.03.019.

Jones, C. F., Kroeker, S. G., Cripton, P. A., and Hall, R. M. (2008). The effect of cerebrospinal fluid on the biomechanics of spinal cord: An ex vivo bovine model using bovine and physical surrogate spinal cord. *Spine (Phila. Pa. 1976).* 33, 580–588. doi:10.1097/BRS.0b013e31817ecc57.

Jones, C. F., Kwon, B. K., and Cripton, P. A. (2012). Mechanical indicators of injury severity are decreased with increased thecal sac dimension in a bench-top model of contusion type spinal cord injury. *J. Biomech.* 45, 1003–1010. doi:10.1016/j.jbiomech.2012.01.025.

Kaleps, I., and Marcus, J. H. (1982). Predictions of child motion during panic braking and impact. *SAE Tech. Pap.* doi:10.4271/821166.

Kameyama, T., Hashizume, Y., and Sobue, G. (1996). Morphologic Features of the Normal Human Cadaveric Spinal Cord. *Spine (Phila. Pa. 1976).* 21, 1285–1290. doi:10.1097/00007632-199606010-00001.

Kato, D., Nakahira, Y., Atsumi, N., and Iwamoto, M. (2018). Development of human-body model THUMS version 6 containing muscle controllers and application to injury analysis in frontal collision after brake deceleration. *Conf. Proc. Int. Res. Counc. Biomech. Inj. IRCOBI* 2018-Septe, 207–223.

Kato, F., Yukawa, Y., Suda, K., Yamagata, M., and Ueta, T. (2012). Normal morphology, age-related changes and abnormal findings of the cervical spine. Part II: Magnetic resonance imaging of over 1,200 asymptomatic subjects. *Eur. Spine J.* 21, 1499–1507. doi:10.1007/s00586-012-2176-4.

Kearney, P. A., Ridella, S. A., Viano, D. C., and Anderson, T. E. (1988). Interaction of Contact Velocity and Cord Compression in Determining the Severity of Spinal Cord Injury. *J. Neurotrauma* 5, 187–208. doi:10.1089/neu.1988.5.187.

Keep, R. F., Hua, Y., and Xi, G. (2012). Brain Water Content: A Misunderstood Measurement? *Transl. Stroke Res.* 3, 263–265. doi:10.1007/s12975-012-0152-2.

Khuyagbaatar, B., Kim, K., and Hyuk Kim, Y. (2014). Effect of bone fragment impact velocity on biomechanical parameters related to spinal cord injury: A finite element study. *J.*

Biomech. 47, 2820–2825. doi:10.1016/j.jbiomech.2014.04.042.

Kim, K. T., Streijger, F., Manouchehri, N., So, K., Shortt, K., Okon, E. B., et al. (2018a). Review of the UBC porcine model of traumatic spinal cord injury. *J. Korean Neurosurg. Soc.* 61, 539–547. doi:10.3340/jkns.2017.0276.

Kim, Y. H., Khuyagbaatar, B., and Kim, K. (2018b). Recent advances in finite element modeling of the human cervical spine. *J. Mech. Sci. Technol.* 32, 1–10. doi:10.1007/s12206-017-1201-2.

Kimpara, H., Nakahira, Y., Iwamoto, M., Miki, K., Ichihara, K., Kawano, S. I., et al. (2006). Investigation of Anteroposterior Head-Neck Responses during Severe Frontal Impacts Using a Brain-Spinal Cord Complex FE Model. *SAE Tech. Pap.* 2006-Novem, 509–544. doi:10.4271/2006-22-0019.

Kleinbach, C., Fehr, J., and Brolin, K. (2018). Simulation of Average Female Rear-End Volunteer Tests using the Active ViVA OpenHBM. *IRCOBI Conf. Proc.*, 237–238.

Kleiven, S. (2007). Predictors for Traumatic Brain Injuries Evaluated through Accident Reconstructions. *SAE Tech. Pap.* 2007-Octob. doi:10.4271/2007-22-0003.

Kleiven, S., and Hardy, W. N. (2002). Correlation of an FE Model of the Human Head with Local Brain Motion-Consequences for Injury Prediction. *SAE Tech. Pap.* 2002-Novem. doi:10.4271/2002-22-0007.

Kloos, A. D., Fisher, L. C., Detloff, M. R., Hassenzahl, D. L., and Basso, D. M. (2005). Stepwise motor and all-or-none sensory recovery is associated with nonlinear sparing after incremental spinal cord injury in rats. *Exp. Neurol.* 191, 251–265. doi:10.1016/j.expneurol.2004.09.016.

Ko, H. Y., Park, J. H., Shin, Y. B., and Baek, S. Y. (2004). Gross quantitative measurements of spinal cord segments in human. *Spinal Cord* 42, 35–40. doi:10.1038/sj.sc.3101538.

Kraan, G. A., Smit, T. H., and Hoogland, P. V. J. M. (2011). Extraforaminal ligaments of the cervical spinal nerves in humans. *Spine J.* 11, 1128–1134. doi:10.1016/j.spinee.2011.10.025.

Kwon, S., Suh, S.-W., Kim, D., Rhyu, I. J., Yu, H., Han, S. W., et al. (2018). Analysis of dural sac thickness in the human cervical spine. *Anat. Sci. Int.* 93, 284–290. doi:10.1007/s12565-017-0412-z.

Lakes, R. (2009). *Viscoelastic materials.* Cambridge University Press doi:10.1017/CBO9780511626722.

Lasswell, T. L., Cronin, D. S., Medley, J. B., and Rasoulinejad, P. (2017). Incorporating ligament laxity in a finite element model for the upper cervical spine. *Spine J.* 17, 1755–1764. doi:10.1016/j.spinee.2017.06.040.

Lee, B. B., Cripps, R. A., Fitzharris, M., and Wing, P. C. (2014). The global map for traumatic spinal cord injury epidemiology: Update 2011, global incidence rate. *Spinal Cord* 52, 110–116. doi:10.1038/sc.2012.158.

Li, X.-F., and Dai, L.-Y. (2009). Three-dimensional finite element model of the cervical spinal cord: preliminary results of injury mechanism analysis. *Spine (Phila. Pa. 1976).* 34, 1140–1147. doi:10.1097/BRS.0b013e31819e2af1.

Liu, Y., Zhou, X., Ma, J., Ge, Y., and Cao, X. (2015). The diameters and number of nerve fibers in spinal nerve roots. *J. Spinal Cord Med.* 38, 532–537. doi:10.1179/1079026814Z.000000000273.

Lizee, E., Robin, S., Song, E., Bertholon, N., Le Coz, J.-Y., Besnault, B., et al. (1998). Development of a 3D Finite Element Model of the Human Body. in *Risk Analysis* doi:https://doi.org/10.4271/99SC05.

LoPachin, R. M., Castiglia, C. M., and Saubermann, A. J. (1991). Elemental composition and water content of myelinated axons and glial cells in rat central nervous system. *Brain Res.* 549, 253–259. doi:10.1016/0006-8993(91)90465-8.

Loth, F., Yardimci, M. A., and Alperin, N. (2001). Hydrodynamic modeling of cerebrospinal fluid motion within the spinal cavity. *J. Biomech. Eng.* 123, 71–79. doi:10.1115/1.1336144.

Maikos, J. T., Elias, R. A. I., and Shreiber, D. I. (2008a). Mechanical Properties of Dura Mater from the Rat Brain and Spinal Cord. *J. Neurotrauma* 25, 38–51. doi:10.1089/neu.2007.0348.

Maikos, J. T., Qian, Z., Metaxas, D., and Shreiber, D. I. (2008b). Finite Element Analysis of Spinal Cord Injury in the Rat. *J. Neurotrauma* 25, 795–816. doi:10.1089/neu.2007.0423.

Maikos, J. T., and Shreiber, D. I. (2007). Immediate damage to the blood-spinal cord barrier due to mechanical trauma. *J. Neurotrauma* 24. doi:10.1089/neu.2006.0149.

Mao, H., Zhang, L., Jiang, B., Genthikatti, V. V., Jin, X., Zhu, F., et al. (2013). Development of a finite element human head model partially validated with thirty five experimental cases. *J. Biomech. Eng.* 135. doi:10.1115/1.4025101.

Mao, H., Zhang, L., Yang, K. H., and King, A. I. (2006). Application of a Finite Element Model of the Brain to Study Traumatic Brain Injury Mechanisms in the Rat. *SAE Tech. Pap.* 2006-November. doi:10.4271/2006-22-0022.

Mattucci, S. (2012). Strain rate dependent properties of younger human cervical spine ligaments. *J. Mech. Behav. Biomed. Mater.* 10, 216–226. doi:10.1016/j.jmbbm.2012.02.004.

Mattucci, S. F. E., and Cronin, D. S. (2015). A method to characterize average cervical spine ligament response based on raw data sets for implementation into injury biomechanics

models. *J. Mech. Behav. Biomed. Mater.* 41, 251–260. doi:10.1016/j.jmbbm.2014.09.023.

Mattucci, S. F. E., Moulton, J. A., Chandrashekar, N., and Cronin, D. S. (2013). Strain rate dependent properties of human craniovertebral ligaments. *J. Mech. Behav. Biomed. Mater.* 23, 71–79. doi:10.1016/j.jmbbm.2013.04.005.

Mazgajczyk, E., Ścigała, K., Czyz, M., Jarmundowicz, W., and Będziński, R. (2012). Mechanical properties of cervical dura mater. *Acta Bioeng. Biomech.* 14, 51–58.

Mazuchowski, E. L. (2001). Investigation of the biomechanical properties of the human spinal cord and its connective tissue. *Diss. available from ProQuest*, 1–138. Available at: http://repository.upenn.edu/dissertations/AAI3003660.

Mazuchowski, E., and Thibauld, L. (2003). Biomechanical Properties of the Human Spinal Cord. *Proc. 2003 Summer Bioeng. Conf. Florida*, 25–29.

Meaney, D. F., Morrison, B., and Bass, C. D. (2014). The mechanics of traumatic brain injury: A review of what we know and what we need to know for reducing its societal burden. *J. Biomech. Eng.* 136. doi:10.1115/1.4026364.

Melvin, J. W., and Yoganandan, N. (2015). "Biomechanics of Brain Injury: A Historical Perspective," in *Accidental Injury* (New York, NY: Springer New York), 221–245. doi:10.1007/978-1-4939-1732-7_9.

Miller, L. E., Urban, J. E., Kelley, M. E., Powers, A. K., Whitlow, C. T., Maldjian, J. A., et al. (2019). Evaluation of Brain Response during Head Impact in Youth Athletes Using an Anatomically Accurate Finite Element Model. *J. Neurotrauma* 36, 1561–1570. doi:10.1089/neu.2018.6037.

Miller, L. E., Urban, J. E., and Stitzel, J. D. (2016). Development and validation of an atlas-based finite element brain model. *Biomech. Model. Mechanobiol.* 15, 1201–1214. doi:10.1007/s10237-015-0754-1.

Nam, M. H., Baek, M., Lim, J., Lee, S., Yoon, J., Kim, J., et al. (2014). Discovery of a novel fibrous tissue in the spinal pia mater by polarized light microscopy. *Connect. Tissue Res.* 55, 147–155. doi:10.3109/03008207.2013.879864.

Network, S. cord injury information (2016). NSCISC Annual Report 2016. *Natl. Spinal Cord Inj. Center, Birmingham, Alabama*. Available at: https://www.nscisc.uab.edu/Public/2016 Annual Report - Complete Public Version.pdf.

Newell, R. L. M. (1999). The spinal epidural space. *Clin. Anat.* 12, 375–379. doi:10.1002/(SICI)1098-2353(1999)12:5<375::AID-CA7>3.0.CO;2-6.

Nicholas, D. S., and Weller, R. O. (1988). The fine anatomy of the human spinal meninges. A light and scanning electron microscopy study. *J. Neurosurg.* 69, 276–282. doi:10.3171/jns.1988.69.2.0276.

Noonan, V. K., Fingas, M., Farry, A., Baxter, D., Singh, A., Fehlings, M. G., et al. (2012). Incidence and prevalence of spinal cord injury in Canada: A national perspective. *Neuroepidemiology* 38, 219–226. doi:10.1159/000336014.

Oakland, R. J., Hall, R. M., Wilcox, R. K., and Barton, D. C. (2006). The Biomechanical Response of Spinal Cord Tissue to Uniaxial Loading. *Proc. Inst. Mech. Eng. Part H J. Eng. Med.* 220, 489–492. doi:10.1243/09544119JEIM135.

Ogden, R. W. (1972). Large deformation isotropic elasticity – on the correlation of theory and experiment for incompressible rubberlike solids. *Proc. R. Soc. London. A. Math. Phys. Sci.* 326, 565–584. doi:10.1098/rspa.1972.0026.

Okada, Y., Ikata, T., Katoh, S., and Yamada, H. (1994). Morphologic analysis of the cervical spinal cord, dural tube, and spinal canal by magnetic resonance imaging in normal adults and patients with cervical spondylotic myelopathy. *Spine (Phila. Pa. 1976).* 19, 2331–5. doi:10.1097/00007632-199410150-00014.

Ommaya, a K. (1968). Mechanical properties of tissues of the nervous system. *J. Biomech.* 1, 127–138. doi:10.1016/0021-9290(68)90015-8.

OMMAYA, A. K., and GENNARELLI, T. A. (1974). CEREBRAL CONCUSSION AND TRAUMATIC UNCONSCIOUSNESS. *Brain* 97, 633–654. doi:10.1093/brain/97.1.633.

Östh, J., Mendoza-Vazquez, M., Linder, A., Svensson, M. Y., and Brolin, K. (2017). The VIVA OpenHBM finite element 50th percentile female occupant model: Whole body model development and kinematic validation. *Conf. Proc. Int. Res. Counc. Biomech. Inj. IRCOBI* 2017-Septe, 443–466.

Östh, J., Mendoza-Vazquez, M., Svensson, M. Y., Linder, A., and Brolin, K. (2016). Development of a 50th percentile female human body model. *2016 IRCOBI Conf. Proc. - Int. Res. Counc. Biomech. Inj.*, 573–575.

Ozawa, H., Matsumoto, T., Ohashi, T., Sato, M., and Kokubun, S. (2001). Comparison of spinal cord gray matter and white matter softness: measurement by pipette aspiration method. *J. Neurosurg. Spine* 95, 221–224. doi:10.3171/spi.2001.95.2.0221.

Ozawa, H., Matsumoto, T., Ohashi, T., Sato, M., and Kokubun, S. (2004). Mechanical properties and function of the spinal pia mater. *J. Neurosurg. Spine* 1, 122–127. doi:10.3171/spi.2004.1.1.0122.

Padgaonkar, A. J., and Prasad, P. (1979). Simulation of side impact using the CAL3D occupant simulation model. *SAE Tech. Pap.* doi:10.4271/791007.

Palastanga, N., Field, D., and Soames, R. (1998). *Anatomy & Human Movemennt Structure & Function*.

Panjabi, M. M. (1998). Cervical Spine Models for Biomechanical Research. *Spine (Phila. Pa. 1976).* 23, 2684–2699. doi:10.1097/00007632-199812150-00007.

Panjabi, M., and White, A. (1988). Biomechanics of nonacute cervical spinal cord trauma. *Spine (Phila. Pa. 1976).* 13, 838–842. doi:10.1097/00007632-198807000-00024.

Panzer, M. B., Myers, B. S., Capehart, B. P., and Bass, C. R. (2012). Development of a finite element model for blast brain injury and the effects of CSF cavitation. *Ann. Biomed. Eng.* 40, 1530–1544. doi:10.1007/s10439-012-0519-2.

Penning, L., Wilmink, J. T., Van Woerden, H. H., and Knol, E. (1986). CT myelographic findings in degenerative disorders of the cervical spine: Clinical significance. *Am. J. Roentgenol.* 146, 793–801. doi:10.2214/ajr.146.4.793.

Persson, C. (2009). *Biomechanical Modelling Of The Spinal Cord And Bone Fragment Interactions During A Vertebral Burst Fracture*. Leeds: University of Leeds (School of Mechanical Engineering).

Persson, C., Evans, S., Marsh, R., Summers, J. L., and Hall, R. M. (2010). Poisson's Ratio and Strain Rate Dependency of the Constitutive Behavior of Spinal Dura Mater. *Ann. Biomed. Eng.* 38, 975–983. doi:10.1007/s10439-010-9924-6.

Persson, C., McLure, S. W. D., Summers, J., and Hall, R. M. (2009). The effect of bone fragment size and cerebrospinal fluid on spinal cord deformation during trauma: an ex vivo study. *J. Neurosurg. Spine* 10, 315–323. doi:10.3171/2009.1.SPINE08286.

Persson, C., Summers, J., and Hall, R. M. (2011a). The effect of cerebrospinal fluid thickness on traumatic spinal cord deformation. *J. Appl. Biomech.* 27, 330–335. doi:10.1123/jab.27.4.330.

Persson, C., Summers, J., and Hall, R. M. (2011b). The Importance of Fluid-Structure Interaction in Spinal Trauma Models. *J. Neurotrauma* 28, 113–125. doi:10.1089/neu.2010.1332.

Pickett, G. E., Campos-Benitez, M., Keller, J. L., and Duggal, N. (2006). Epidemiology of traumatic spinal cord injury in Canada. *Spine (Phila. Pa. 1976).* 31, 799–805. doi:10.1097/01.brs.0000207258.80129.03.

Pickett, W., Simpson, K., Walker, J., and Brison, R. J. (2003). Traumatic Spinal Cord Injury in Ontario, Canada. *J. Trauma Inj. Infect. Crit. Care* 55, 1070–1076. doi:10.1097/01.TA.0000034228.18541.D1.

Polak-Kraśna, K., Robak-Nawrocka, S., Szotek, S., Czyż, M., Gheek, D., and Pezowicz, C. (2019). The denticulate ligament – Tensile characterisation and finite element micro-scale model of the structure stabilising spinal cord. *J. Mech. Behav. Biomed. Mater.* 91, 10–17. doi:10.1016/j.jmbbm.2018.11.017.

Polak, K., Czyz, M., Royal, T., Hospital, O., and Foundati, N. H. S. (2016). Article : Experimental Investigations of Mechanical Characteristics of Denticulate Ligaments.

Polak, K., Czyz, M., Ścigała, K., Jarmundowicz, W., and Bedziński, R. (2014). Biomechanical

characteristics of the porcine denticulate ligament in different vertebral levels of the cervical spine-Preliminary results of an experimental study. *J. Mech. Behav. Biomed. Mater.* 34, 165–170. doi:10.1016/j.jmbbm.2014.02.010.

Post, A., Oeur, A., Hoshizaki, B., and Gilchrist, M. D. (2013). An examination of American football helmets using brain deformation metrics associated with concussion. *Mater. Des.* 45, 653–662. doi:10.1016/j.matdes.2012.09.017.

Puso, M. A., and Solberg, J. (2006). A stabilized nodally integrated tetrahedral. *Int. J. Numer. Methods Eng.* doi:10.1002/nme.1651.

Ramo, N. L., Shetye, S. S., Streijger, F., Lee, J. H. T., Troyer, K. L., Kwon, B. K., et al. (2018a). Comparison of in vivo and ex vivo viscoelastic behavior of the spinal cord. *Acta Biomater.* doi:10.1016/j.actbio.2017.12.024.

Ramo, N. L., Troyer, K. L., and Puttlitz, C. M. (2018b). Viscoelasticity of spinal cord and meningeal tissues. *Acta Biomater.*, 15–18. doi:10.1016/j.actbio.2018.05.045.

Rashid, B., Destrade, M., and Gilchrist, M. D. (2012). Determination of friction coefficient in unconfined compression of brain tissue. *J. Mech. Behav. Biomed. Mater.* 14, 163–171. doi:10.1016/j.jmbbm.2012.05.001.

Reina, M. A., De León Casasola, O., Villanueva, M. C., López, A., Machés, F., and De Andrés, J. A. (2004). Ultrastructural Findings in Human Spinal Pia Mater in Relation to Subarachnoid Anesthesia. *Anesth. Analg.* 98, 1479–1485. doi:10.1213/01.ANE.0000113240.09354.E9.

Reina, M. A., López, A., Dittmann, M., and De Andrés, J. A. (2015). "Ultrastructure of Spinal Dura Mater," in *Atlas of Functional Anatomy for Regional Anesthesia and Pain Medicine: Human Structure, Ultrastructure and 3D Reconstruction Images*, eds. M. A. Reina, J. A. De Andrés, A. Hadzic, A. Prats-Galino, X. Sala-Blanch, and A. A. J. van Zundert (Cham: Springer International Publishing), 411–434. doi:10.1007/978-3-319-09522-6_20.

Richardson, M. G., and Wissler, R. N. (1996). Density of lumbar cerebrospinal fluid in pregnant and nonpregnant humans. *Anesthesiology* 85, 326–30. doi:10.1097/00000542-199608000-00014.

Roache, P. J. (1997). Quantification of uncertainty in computational fluid dynamics. *Annu. Rev. Fluid Mech.* 29, 123–160. doi:10.1146/annurev.fluid.29.1.123.

Roache, P. J. (1998). Verification and Validation in Computational Science and Engineering. *Comput. Sci. Eng.*

Robin, S. (2001). Humos: Human Model for Safety–a joint effort towards the development of refined human like car occupant models. *Stapp Car Crash Conf.*, 1–9. Available at: http://www-nrd.nhtsa.dot.gov/pdf/nrd-01/esv/esv17/proceed/00129.pdf.

Rowson, S., and Duma, S. M. (2013). Brain injury prediction: Assessing the combined

probability of concussion using linear and rotational head acceleration. *Ann. Biomed. Eng.* 41, 873–882. doi:10.1007/s10439-012-0731-0.

Ruan, J., El-Jawahri, R., Chai, L., Barbat, S., and Prasad, P. (2003). Prediction and Analysis of Human Thoracic Impact Responses and Injuries in Cadaver Impacts Using a Full Human Body Finite Element Model. *SAE Tech. Pap.* 2003-Octob, 299–321. doi:10.4271/2003-22-0014.

Runza, M., Pietrabissa, R., Mantero, S., Albani, A., Quaglini, V., and Contro, R. (1999). Lumbar Dura Mater Biomechanics: Experimental Characterization and Scanning Electron Microscopy Observatios. *Anesth. Analg.* 88, 1317–1321. doi:10.1097/00000539-199906000-00022.

Russell, C. M., Choo, A. M., Tetzlaff, W., Chung, T.-E., and Oxland, T. R. (2012). Maximum Principal Strain Correlates with Spinal Cord Tissue Damage in Contusion and Dislocation Injuries in the Rat Cervical Spine. *J. Neurotrauma* 29, 1574–1585. doi:10.1089/neu.2011.2225.

Rycman, A., McLachlin, S., and Cronin, D. S. (2021). A Hyper-Viscoelastic Continuum-Level Finite Element Model of the Spinal Cord Assessed for Transverse Indentation and Impact Loading. *Front. Bioeng. Biotechnol.* 9. doi:10.3389/fbioe.2021.693120.

Rycman, A., McLachlin, S., and Cronin, D. S. (2022). Comparison of numerical methods for cerebrospinal fluid representation and fluid–structure interaction during transverse impact of a finite element spinal cord model. *Int. j. numer. method. biomed. eng.* doi:10.1002/cnm.3570.

Sadowsky, C., Volshteyn, O., Schultz, L., and McDonald, J. W. (2002). Spinal cord injury. *Disabil. Rehabil.* 24, 680–687. doi:10.1080/09638280110110640.

Salegio, E. A., Bresnahan, J. C., Sparrey, C. J., Camisa, W., Fischer, J., Leasure, J., et al. (2016). A Unilateral Cervical Spinal Cord Contusion Injury Model in Non-Human Primates (*Macaca mulatta*). *J. Neurotrauma* 33, 439–459. doi:10.1089/neu.2015.3956.

Schmitt, K.-U., Niederer, P. F., Cronin, D. S., Morrison III, B., Muser, M. H., and Walz, F. (2019). *Trauma Biomechanics*. doi:10.1007/978-3-030-11659-0.

Sekhon, L. H. S., and Fehlings, M. G. (2001). Epidemiology, Demographics, and Pathophysiology of Acute Spinal Cord Injury. *Spine (Phila. Pa. 1976).* 26, S2–S12. doi:10.1097/00007632-200112151-00002.

Shetye, S. S., Deault, M. M., and Puttlitz, C. M. (2014a). Biaxial response of ovine spinal cord dura mater. *J. Mech. Behav. Biomed. Mater.* 34, 146–153. doi:10.1016/j.jmbbm.2014.02.014.

Shetye, S. S., Troyer, K. L., Streijger, F., Lee, J. H. T., Kwon, B. K., Cripton, P. A., et al. (2014b). Nonlinear viscoelastic characterization of the porcine spinal cord. *Acta*

Biomater. 10, 792–797. doi:10.1016/j.actbio.2013.10.038.

Shi, B., Zheng, X., Min, S., Zhou, Z., Ding, Z., and Jin, A. (2014). The morphology and clinical significance of the dorsal meningovertebra ligaments in the cervical epidural space. *Spine J.* 14, 2733–2739. doi:10.1016/j.spinee.2014.04.014.

Shi, B., Zheng, X., Zhang, H., Sun, C., Cao, Y., Jin, A., et al. (2015). The Morphology and Clinical Significance of the Extraforaminal Ligaments at the Cervical Level. *Spine (Phila. Pa. 1976).* 40, E9–E17. doi:10.1097/BRS.0000000000000668.

Singh, D., Boakye-Yiadom, S., and Cronin, D. S. (2019). Comparison of porcine brain mechanical properties to potential tissue simulant materials in quasi-static and sinusoidal compression. *J. Biomech.* 92, 84–91. doi:10.1016/j.jbiomech.2019.05.033.

Singh, D., Cronin, D. S., and Haladuick, T. N. (2014). Head and brain response to blast using sagittal and transverse finite element models. *Int. j. numer. method. biomed. eng.* 30, 470–489. doi:10.1002/cnm.2612.

Sparrey, C. J., Choo, A. M., Liu, J., Tetzlaff, W., and Oxland, T. R. (2008). The distribution of tissue damage in the spinal cord is influenced by the contusion velocity. *Spine (Phila. Pa. 1976).* 33, 812–819. doi:10.1097/BRS.0b013e3181894fd3.

Sparrey, C. J., and Keaveny, T. M. (2009). The Effect of Flash Freezing on Variability in Spinal Cord Compression Behavior. *J. Biomech. Eng.* 131, 111010. doi:10.1115/1.4000079.

Sparrey, C. J., and Keaveny, T. M. (2011). Compression behavior of porcine spinal cord white matter. *J. Biomech.* 44, 1078–1082. doi:10.1016/j.jbiomech.2011.01.035.

Sparrey, C. J., Salegio, E. A., Camisa, W., Tam, H., Beattie, M. S., and Bresnahan, J. C. (2016). Mechanical Design and Analysis of a Unilateral Cervical Spinal Cord Contusion Injury Model in Non-Human Primates. *J. Neurotrauma* 33, 1136–1149. doi:10.1089/neu.2015.3974.

Standring, S., and Gray, H. (2009). *Gray's Anatomy: the anatomical basis of clinical practice.* 40th ed. Edinburgh: Churchill Livingstone.

Stoner, K. E., Abode-Iyamah, K. O., Fredericks, D. C., Viljoen, S., Howard, M. A., and Grosland, N. M. (2020). A comprehensive finite element model of surgical treatment for cervical myelopathy. *Clin. Biomech.* 74, 79–86. doi:10.1016/j.clinbiomech.2020.02.009.

Tabiei, A., and Chowdhury, M. R. (2004). Transient Response of a Projectile in Gun Launch Simulation Using Lagrangian and ALE Methods. *Aerosp. Eng.*, 25–44.

Takhounts, E. G., Eppinger, R. H., Campbell, J. Q., Tannous, R. E., Power, E. D., and Shook, L. S. (2003). On the Development of the SIMon Finite Element Head Model. *Stapp Car Crash J.* 47, 107–133. doi:2003-22-0007 [pii].

Takhounts, E. G., Ridella, S. A., Hasija, V., Tannous, R. E., Campbell, J. Q., Malone, D., et al. (2008). Investigation of Traumatic Brain Injuries Using the Next Generation of Simulated Injury Monitor (SIMon) Finite Element Head Model. *SAE Tech. Pap.* 2008-Novem. doi:10.4271/2008-22-0001.

Tan, P., Lee, B., and Tsangalis, C. (2009). FEA modelling prediction of the transmitted overpressure and particle acceleration within a frame subjected to shock tube blast loadings. in *18th World IMACS Congress and MODSIM 2009 - International Congress on Modelling and Simulation: Interfacing Modelling and Simulation with Mathematical and Computational Sciences, Proceedings*.

Tardieu, G. G., Fisahn, C., Loukas, M., Moisi, M., Chapman, J., Oskouian, R. J., et al. (2016). The Epidural Ligaments (of Hofmann): A Comprehensive Review of the Literature. *Cureus* 8. doi:10.7759/cureus.779.

Taylor, C., Bell, J. M., Breiding, M. J., and Xu, L. (2017). Traumatic Brain Injury-Related Emergency Department Visits, Hospitalizations, and Deaths-United States, 2007 and 2013 Surveillance Summaries Centers for Disease Control and Prevention MMWR Editorial and Production Sta. *Morb. Mortal. Wkly. Rep.* 66, 1–8. Available at: https://www.cdc.gov/mmwr/volumes/66/ss/pdfs/ss6609.pdf.

Telano, L. N., and Baker, S. (2022). *Physiology, Cerebral Spinal Fluid*. Available at: http://www.ncbi.nlm.nih.gov/pubmed/30085549.

Tencer, A. F., Allen, B. L., and Ferguson, R. L. (1985). A biomechanical study of thoracolumbar spine fractures with bone in the canal: Part III. Mechanical properties of the dura and its tethering ligaments. *Spine (Phila. Pa. 1976).* 10, 741–747. doi:10.1097/00007632-198510000-00009.

Thunnissen, J., Wismans, J., Ewing, C. L., and Thomas, D. J. (1995). Human Volunteer Head-Neck Response in Frontal Flexion: A New Analysis. in doi:10.4271/952721.

Tubbs, R. S., Salter, G., Grabb, P. A., and Oakes, W. J. (2001). The denticulate ligament: Anatomy and functional significance. *J. Neurosurg.* 94, 271–275. doi:10.3171/spi.2001.94.2.0271.

Tunturi, A. R. (1978). Elasticity of the spinal cord, pia, and denticulate ligament in the dog. *J. Neurosurg.* 48, 975–979. doi:10.3171/jns.1978.48.6.0975.

van Noort, R., Black, M. M., Martin, T. R. P., and Meanley, S. (1981). A study of the uniaxial mechanical properties of human dura mater preserved in glycerol. *Biomaterials* 2, 41–45. doi:10.1016/0142-9612(81)90086-7.

Verma, M. K., and Repa, B. S. (1983). Pedestrian impact simulation - A preliminary study. *SAE Tech. Pap.* doi:10.4271/831601.

Wadhwani, S., Loughenbury, P., and Soames, R. (2004). The Anterior Dural (Hofmann)

Ligaments. *Spine (Phila. Pa. 1976).* 29, 623–627. doi:10.1097/01.BRS.0000115129.59484.24.

Watson, C., Paxinos, G., and Kayalioglu, G. (2009). *The Spinal Cord.* Elsevier doi:10.1016/C2009-0-01677-8.

Wedekind, C., and Lippert-Grüner, M. (2005). Long-term outcome in severe traumatic brain injury is significantly influenced by brainstem in involvement. *Brain Inj.* 19, 681–684. doi:10.1080/02699050400025182.

Wilcox, R. K., Allen, D. J., Hall, R. M., Limb, D., Barton, D. C., and Dickson, R. A. (2004). A dynamic investigation of the burst fracture process using a combined experimental and finite element approach. *Eur. Spine J.* 13, 481–488. doi:10.1007/s00586-003-0625-9.

Wilcox, R. K., Boerger, T. O., Allen, D. J., Barton, D. C., Limb, D., Dickson, R. A., et al. (2003). A Dynamic Study of Thoracolumbar Burst Fractures. *J. Bone Joint Surg. Am.* 85-A, 2184–2189.

Wismans, J., Philippens, M., Van Oorschot, E., Kallieris, D., and Mattern, R. (1987). Comparison of human volunteer and cadaver head-neck response in frontal flexion. in *SAE Technical Papers* doi:10.4271/872194.

Wismans, J., and Spenny, C. H. (1983). Performance requirements for mechanical necks in lateral flexion. in *SAE Technical Papers* doi:10.4271/831613.

Wismans, J., Van Oorschot, H., and Woltring, H. J. (1986). Omni-directional human head-neck response. in *SAE Technical Papers* doi:10.4271/861893.

Xu, F., Seffen, K., and Lu, T. (2008). A Quasi-Linear Viscoelastic Model for Skin Tissue. *Proc. 3rd IASME / WSEAS Int. Conf. Contin. Mech.*, 14–21.

Xu, J., and Wang, J. (2014). Interaction Methods for the SPH Parts in LS-DYNA. *13th Int. LS-DYNA Users Conf.*, 1–12.

Yang, K. H. (2017). *Basic finite element method as applied to injury biomechanics.* doi:10.1016/c2015-0-06702-8.

Yang, K. H. (2018). Modeling Human Body for Injury Biomechanics Analysis. *Basic Finite Elem. Method as Appl. to Inj. Biomech.*, ccclxxxv–ccclxxxvii. doi:10.1016/B978-0-12-809831-8.02002-X.

Yang, K. H., Hu, J., White, N. A., King, A. I., Chou, C. C., and Prasad, P. (2006). Development of Numerical Models for Injury Biomechanics Research: A Review of 50 Years of Publications in the Stapp Car Crash Conference. *SAE Tech. Pap.* 2006-Novem. doi:10.4271/2006-22-0017.

Yardimci, M. A. (2000). Hydrodynamic Modeling of Cerebrospinal Fluid Motion Within the Spinal Cavity. *J. Biomech. Eng.* 123, 71. doi:10.1115/1.1336144.

Yoganandan, N., Kumaresan, S., Voo, L., and Pintar, F. A. (1996). Finite Element Applications in Human Cervical Spine Modeling.

Yreux, E. (2018). Fluid Flow Modeling with SPH in LS-DYNA. *15th Int. LS-DYNA Users Conf.*

Yucesoy, A., Pence, T. J., Alvarez, R. M., and Willis, A. M. (2018). Developing a Numerical Model for Human Brain under Blast Loading. *15 th Int. LS-DYNA ® Users Conf.*

Zhang, L., Yang, K. H., Dwarampudi, R., Omori, K., Li, T., Chang, K., et al. (2001). Recent Advances in Brain Injury Research: A New Human Head Model Development and Validation. *SAE Tech. Pap.* 45. doi:10.4271/2001-22-0017.

Zhang, L., Yang, K. H., and King, A. I. (2004). A Proposed Injury Threshold for Mild Traumatic Brain Injury. *J. Biomech. Eng.* 126, 226–236. doi:10.1115/1.1691446.

Zhao, W., Cai, Y., Li, Z., and Ji, S. (2017). Injury prediction and vulnerability assessment using strain and susceptibility measures of the deep white matter. *Biomech. Model. Mechanobiol.* 16, 1709–1727. doi:10.1007/s10237-017-0915-5.

Zhou, Z., Li, X., and Kleiven, S. (2020). Biomechanics of Periventricular Injury. *J. Neurotrauma* 37, 1074–1090. doi:10.1089/neu.2019.6634.